

A Search for Higgs Decay to Pseudoscalar Higgs-like Particles at  
CMS

Samuel Higginbotham

A Dissertation  
Presented to the Faculty  
of Princeton University  
in Candidacy for the Degree  
of Doctor of Philosophy

Recommended for Acceptance  
by the Department of  
Physics  
Advisor: Daniel Marlow

August, 2022

© Copyright 2022 by Samuel Higginbotham.

All rights reserved.

# Abstract

A search is conducted for exotic decays of the Standard Model Higgs Boson,  $H$ , decaying to a pair of pseudoscalars,  $a$ , which then decay to pairs of muons and tau leptons. Pseudoscalar masses between 20 and 60 GeV are investigated using the full Run II dataset, corresponding to a luminosity of  $137 \text{ fb}^{-1}$ . The existence of the pseudoscalar Higgs is primarily motivated by Two Higgs Doublet Models with the extension of a Singlet (2HDM+S). Upper limits on the branching fraction are set.

# Acknowledgements

thank

# Contents

<b>Abstract</b>	<b>iii</b>
<b>Acknowledgements</b>	<b>iv</b>
<b>Contents</b>	<b>v</b>
<b>List of Figures</b>	<b>viii</b>
<b>List of Tables</b>	<b>xv</b>
<b>1 Introduction</b>	<b>1</b>
1.1 The Standard Model and Beyond . . . . .	1
1.2 Gauge Principle, Yang Mills Theories, and the Weinberg-Salam Model . . . . .	2
1.3 The Higgs Mechanism . . . . .	4
1.4 Higgs Doublet Models . . . . .	5
1.5 Previous and present searches in 2HDM+S models . . . . .	6
<b>2 CERN, The LHC, and The CMS Detector</b>	<b>13</b>
2.1 CERN and the Large Hadron Collider . . . . .	13
2.2 The Compact Muon Solenoid detector . . . . .	14
2.3 Subdetector Systems . . . . .	15
2.3.1 Tracker . . . . .	15
2.3.2 Electronic Calorimeter . . . . .	19
2.3.3 Hadronic Calorimeter . . . . .	19
2.3.4 Muon Chambers . . . . .	19

2.4	Level 1 Trigger System and High Level Trigger . . . . .	20
2.5	Particle Flow Algorithms . . . . .	21
2.6	Computational Infrastructure . . . . .	22
<b>3</b>	<b>Luminosity</b>	<b>24</b>
<b>4</b>	<b>Lepton Identification and Data</b>	<b>27</b>
4.1	Lepton Identification . . . . .	27
4.1.1	Muon Identification Systems . . . . .	27
4.1.2	Electron Identification Systems . . . . .	27
4.1.3	Tau Identification Systems . . . . .	28
4.2	Data and Simulation Used for Analysis . . . . .	29
4.2.1	$2\mu 2\tau$ Signal Samples . . . . .	30
4.3	Corrections to Simulations . . . . .	30
4.3.1	Muon energy scale . . . . .	30
4.3.2	Electron energy scale . . . . .	31
4.3.3	$\tau$ energy scale . . . . .	31
4.3.4	$\tau_h$ ID efficiency . . . . .	32
4.3.5	$e \rightarrow \tau_h$ and $\mu \rightarrow \tau_h$ misidentification rate . . . . .	33
4.3.6	Pileup Re-weighting . . . . .	34
4.3.7	Electron and muon identification efficiency . . . . .	34
4.3.8	Generator event weights and luminosity . . . . .	34
4.3.9	Offline Muon Selection . . . . .	35
4.3.10	Visualizing the Corrections . . . . .	35
<b>5</b>	<b>Event Selection</b>	<b>37</b>
5.1	Framing an Analysis at CERN . . . . .	37
5.2	Defining Signal and Control Regions . . . . .	37
5.2.1	Optimizing Lepton Pair Selection . . . . .	38
<b>6</b>	<b>Background Estimation</b>	<b>43</b>
6.0.1	Brief Outline of the Fake Rate Method . . . . .	43

6.0.2	Measurement of the Fake Rate . . . . .	44
6.0.3	Application of the Fake Rate Method . . . . .	47
<b>7</b>	<b>Statistical Inference Modeling</b>	<b>49</b>
7.1	Statistical Inference at CERN . . . . .	49
7.2	Worked Example for Low Stat Analyses . . . . .	51
7.3	Fit model for pseudoscalar Higgs search . . . . .	52
<b>8</b>	<b>Conclusions</b>	<b>62</b>
<b>A</b>	<b>Data and Simulation Samples</b>	<b>69</b>
A.1	Data and Simluation Used for Analysis . . . . .	69
<b>B</b>	<b>Fake Rate Measurements</b>	<b>74</b>
<b>C</b>	<b>Systematic Uncertainties</b>	<b>80</b>
<b>D</b>	<b>Fit Models</b>	<b>91</b>
<b>References</b>		<b>106</b>

# List of Figures

1.1	Standard Model particles . . . . .	2
1.2	Type I 2HDM+S scenario branching fractions [4] . . . . .	7
1.3	Type II 2HDM+S scenario branching fractions [4] . . . . .	9
1.4	Type III 2HDM+S scenario branching fractions [4] . . . . .	10
1.5	Type IV 2HDM+S scenario branching fractions [4] . . . . .	11
1.6	Diagram of Higgs decay to pseudoscalar $a$ particles (Left) and branching ratios for pseudoscalar production in different $\tan\beta$ scenarios and different 2HDM+S Types (right) . . . . .	12
2.1	Overview of the Large Hadron Collider spanning Switzerland and France - Maximilien Brice, CERN . . . . .	14
2.2	The CMS detector full 3D image with all subsystems labeled . . . . .	15
2.3	(simulation) MIP particle traveling across a silicon strip sensor at $45^\circ$ over time from 0.0, 1.1, 1.5, 2, 3, 4, 5, 6, 7 nanoseconds. The induced surface current dissipates and would be collected by the channels of the silicon module [9]. . . . .	17
2.4	encapsulated token bit manager of a forward pixel module currently installed in CMS	18
2.5	The silicon tracker system, consisting of the inner pixel system (BPIX and FPIX), The Tracker End Caps (TEC), Tracker Inner Detector(TID), Tracker Inner Barrel (TIB), and the Tracker Outer Barrel (TOB) by position in $r$ , $z$ , and $\eta$ [8] . . . . .	18
2.6	Overview of the HCAL system from the $z-\eta$ plane showing the hadron barrel (HB), encap(HE), outer (HO), and the forward (HF) subsystems [8] . . . . .	20
2.7	Muon system involving multiple subdetector systems: tracker, solenoid, and the muon gas chambers around the iron yoke (grey) - Maximilien Brice, CERN . . . . .	21

2.8	Schematic overview of Tier0 computing, data can be available from different sections allowing for data quality monitoring and also storage to several databases [14] . . . . .	22
4.1	diagram depicting the possible decays of the tau lepton: 65% of the time hadronically and 18% to tau neutrino and electron with antielectron neutrino (17% for muon) . . . . .	32
4.2	Tau mass distributions considering the nominal $\tau_h$ energy scale in simulation (left), or the $\tau_h$ energy scale shifted by -6 (left) or +6% (right), in the $\mu\tau_h$ final state, for the 1 prong + pizero decay mode. . . . .	33
4.3	Systematic Shift in the Uncertainty Model for 2016 $\mu\mu\tau\tau$ for the muon energy scale shift down (left), nominal (mid), and up (right), no data is shown on this plot as it directly reflects the signal region without the extraction cuts . . . . .	35
5.1	Invariant mass of the four lepton system for 2018 data in all Channels . . . . .	41
5.2	Several data-MC control plots for full RunII data in all Channels . . . . .	42
6.1	Fake factors determined in the QCD multijet determination region with 0 jet in the $\tau_h$ final state in 2017. They are fitted with linear functions as a function of the $\tau_h p_T$ . The green and purple lines indicate the shape systematics obtained by uncorrelating the uncertainties in the two fit parameters returned by the fit. . . . .	46
6.2	Diagram depicting the measurement and application regions, this “ABCD” method is multiplied by each of the $\tau$ leptons in the final state . . . . .	48
6.3	Validation of the fake factor method, fake factors are applied to the same sign tight region . . . . .	48
7.1	Signal fit using a Voigtian function . . . . .	52
7.2	Signal fits using a voiigtian function for a-mass at 40GeV . . . . .	53
7.3	Spline functions for 2016 mmmt a 3rd order polynomial is used for for Alpha, Sigma, and Normalization, a 1st order polynomial is used for the Mean . . . . .	54
7.4	Spline functions for 2016 mmet a 3rd order polynomial is used for for Alpha, Sigma, and Normalization, a 1st order polynomial is used for the Mean . . . . .	55
7.5	Spline functions for 2016 mmmt a 3rd order polynomial is used for for Alpha, Sigma, and Normalization, a 1st order polynomial is used for the Mean . . . . .	56

7.6	Spline functions for 2016 mmem a 3rd order polynomial is used for for Alpha, Sigma, and Normalization, a 1st order polynomial is used for the Mean . . . . .	57
7.7	Irreducible background fit using Bernstein polynomials . . . . .	58
7.8	Reducible background fit using Bernstein polynomials . . . . .	59
7.9	Expected systematic impacts for the fit model $\mu\mu\mu\tau$ . . . . .	61
8.1	Asymptotic CL Limits on the branching fraction times ratio of the SM cross sections	63
8.2	Asymptotic CL Limits on the branching fraction times ratio of the SM cross sections for 2017 . . . . .	64
8.3	Asymptotic CL Limits on the branching fraction times ratio of the SM cross sections for 2018 . . . . .	65
8.4	Asymptotic CL Limits on the branching fraction times ratio of the SM cross sections for the full Run II dataset $137\text{fb}^{-1}$ . . . . .	66
8.5	2HDM model specific scenarios upper 95% CL limits on the branch fraction of Higgs to a a times the ratio of the SM cross sections for the full Run II dataset $137\text{fb}^{-1}$ .	67
B.1	Fake factors determined in the W+jets determination region with 0 jet in the $e\tau_h$ final state in 2016 (left), 2017 (center), and 2018 (right). They are fitted with linear functions as a function of the $\tau_h p_T$ . The green and purple lines indicate the shape systematics obtained by uncorrelating the uncertainties in the two fit parameters returned by the fit. . . . .	74
B.2	Fake factors determined in the W+jets determination region with one jet in the $e\tau_h$ final state in 2016 (left), 2017 (center), and 2018 (right). They are fitted with linear functions as a function of the $\tau_h p_T$ . The green and purple lines indicate the shape systematics obtained by uncorrelating the uncertainties in the two fit parameters returned by the fit. . . . .	75
B.3	Fake factors determined in the W+jets determination region with at least two jets in the $e\tau_h$ final state in 2016 (left), 2017 (center), and 2018 (right). They are fitted with linear functions as a function of the $\tau_h p_T$ . The green and purple lines indicate the shape systematics obtained by uncorrelating the uncertainties in the two fit parameters returned by the fit. . . . .	75

B.4	Fake factors determined in the W+jets determination region with 0 jet in the $\tau_h$ final state in 2016 (left), 2017 (center), and 2018 (right). They are fitted with linear functions as a function of the $\tau_h p_T$ . The green and purple lines indicate the shape systematics obtained by uncorrelating the uncertainties in the two fit parameters returned by the fit. . . . .	75
B.5	Fake factors determined in the W+jets determination region with one jet in the $\tau_h$ final state in 2016 (left), 2017 (center), and 2018 (right). They are fitted with linear functions as a function of the $\tau_h p_T$ . The green and purple lines indicate the shape systematics obtained by uncorrelating the uncertainties in the two fit parameters returned by the fit. . . . .	76
B.6	Fake factors determined in the W+jets determination region with at least two jets in the $\tau_h$ final state in 2016 (left), 2017 (center), and 2018 (right). They are fitted with linear functions as a function of the $\tau_h p_T$ . The green and purple lines indicate the shape systematics obtained by uncorrelating the uncertainties in the two fit parameters returned by the fit. . . . .	76
B.7	Fake factors determined in the QCD multijet determination region with 0 jet in the $e\tau_h$ final state in 2016 (left), 2017 (center), and 2018 (right). They are fitted with linear functions as a function of the $\tau_h p_T$ . The green and purple lines indicate the shape systematics obtained by uncorrelating the uncertainties in the two fit parameters returned by the fit. . . . .	76
B.8	Fake factors determined in the QCD multijet determination region with one jet in the $e\tau_h$ final state in 2016 (left), 2017 (center), and 2018 (right). They are fitted with linear functions as a function of the $\tau_h p_T$ . The green and purple lines indicate the shape systematics obtained by uncorrelating the uncertainties in the two fit parameters returned by the fit. . . . .	77
B.9	Fake factors determined in the QCD multijet determination region with at least two jets in the $e\tau_h$ final state in 2016 (left), 2017 (center), and 2018 (right). They are fitted with linear functions as a function of the $\tau_h p_T$ . The green and purple lines indicate the shape systematics obtained by uncorrelating the uncertainties in the two fit parameters returned by the fit. . . . .	77

B.10	Fake factors determined in the QCD multijet determination region with one jet in the $\tau_h$ final state in 2016 (left), 2017 (center), and 2018 (right). They are fitted with linear functions as a function of the $\tau_h p_T$ . The green and purple lines indicate the shape systematics obtained by uncorrelating the uncertainties in the two fit parameters returned by the fit. . . . .	77
B.11	Fake factors determined in the QCD multijet determination region with at least two jets in the $\tau_h$ final state in 2016 (left), 2017 (center), and 2018 (right). They are fitted with linear functions as a function of the $\tau_h p_T$ . The green and purple lines indicate the shape systematics obtained by uncorrelating the uncertainties in the two fit parameters returned by the fit. . . . .	78
B.12	Fake factors determined in the $t\bar{t}$ determination region in data in the $e\tau_h$ final state in 2016 (left), 2017 (center), and 2018 (right). They are fitted with linear functions as a function of the $\tau_h p_T$ . The green and purple lines indicate the shape systematics obtained by uncorrelating the uncertainties in the two fit parameters returned by the fit. . . . .	78
B.13	Fake factors determined in the $t\bar{t}$ simulation in the $e\tau_h$ final state in 2016 (left), 2017 (center), and 2018 (right). They are fitted with linear functions as a function of the $\tau_h p_T$ . The green and purple lines indicate the shape systematics obtained by uncorrelating the uncertainties in the two fit parameters returned by the fit. . . . .	78
B.14	Fake factors determined in the $t\bar{t}$ determination region in data in the $\tau_h$ final state in 2016 (left), 2017 (center), and 2018 (right). They are fitted with linear functions as a function of the $\tau_h p_T$ . The green and purple lines indicate the shape systematics obtained by uncorrelating the uncertainties in the two fit parameters returned by the fit. . . . .	79
B.15	Fake factors determined in the $t\bar{t}$ simulation in the $\tau_h$ final state in 2016 (left), 2017 (center), and 2018 (right). They are fitted with linear functions as a function of the $\tau_h p_T$ . The green and purple lines indicate the shape systematics obtained by uncorrelating the uncertainties in the two fit parameters returned by the fit. . . . .	79
C.1	Expected systematic impacts for the fit model $\mu\mu\mu\tau$ . . . . .	80

C.2	Expected systematic impacts for the fit model $\mu\mu e\tau$	81
C.3	Expected systematic impacts for the fit model for 2016 $\mu\mu\tau\tau$	82
C.4	Expected systematic impacts for the fit model for 2016 $\mu\mu ee$	83
C.5	Expected systematic impacts for the fit model $\mu\mu e\tau$	84
C.6	Expected systematic impacts for the fit model for 2017 $\mu\mu\tau\tau$	85
C.7	Expected systematic impacts for the fit model for 2017 $\mu\mu ee$	86
C.8	Expected systematic impacts for the fit model $\mu\mu\mu\tau$	87
C.9	Expected systematic impacts for the fit model $\mu\mu e\tau$	88
C.10	Expected systematic impacts for the fit model for 2018 $\mu\mu\tau\tau$	89
C.11	Expected systematic impacts for the fit model for 2018 $\mu\mu ee$	90
D.1	2017 Signal fit using a Voigtian function	92
D.2	Spline functions for 2017 mmmt a 3rd order polynomial is used for for Alpha, Sigma, and Normalization, a 1st order polynomial is used for the Mean	93
D.3	Spline functions for 2017 mmet a 3rd order polynomial is used for for Alpha, Sigma, and Normalization, a 1st order polynomial is used for the Mean	94
D.4	Spline functions for 2017 mmtt a 3rd order polynomial is used for for Alpha, Sigma, and Normalization, a 1st order polynomial is used for the Mean	95
D.5	Spline functions for 2017 mmem a 3rd order polynomial is used for for Alpha, Sigma, and Normalization, a 1st order polynomial is used for the Mean	96
D.6	2017 irreducible background fit using Bernstein polynomials	97
D.7	2017 reducible background fit using Bernstein polynomials	98
D.8	2018 Signal fit using a Voigtian function	99
D.9	Spline functions for 2018 mmmt a 3rd order polynomial is used for for Alpha, Sigma, and Normalization, a 1st order polynomial is used for the Mean	100
D.10	Spline functions for 2018 mmet a 3rd order polynomial is used for for Alpha, Sigma, and Normalization, a 1st order polynomial is used for the Mean	101
D.11	Spline functions for 2018 mmtt a 3rd order polynomial is used for for Alpha, Sigma, and Normalization, a 1st order polynomial is used for the Mean	102

D.12 Spline functions for 2018 mmem a 3rd order polynomial is used for for Alpha, Sigma, and Normalization, a 1st order polynomial is used for the Mean . . . . .	103
D.13 2018 irreducible background fit using Bernstein polynomials . . . . .	104
D.14 2018 reducible background fit using Bernstein polynomials . . . . .	105

# List of Tables

4.1	Possible hadronic tau decays, $h$ doesn't indicate a Higgs particle but a hadronic prong [19]	28
4.2	Measured energy scale correction for genuine across all years.	31
4.3	Measured energy scale correction for genuine across all years.	31
4.4	Measured $\tau_h$ energy scale correction for genuine $\tau_h$ 's across all years.	32
4.5	Scale factors to correct for Offline muon selection being less than the online trigger threshold.	35
5.1	Lepton Pair Matching Efficiency	38
5.2	Event selection requirements for the four decay channels. These demarcate cuts that are applied to the $p_T$ , $\eta$ , and isolation of the particle in addition to the trigger requirements.	39
7.1		60
8.1	Expected event yields of signal and background categories across all years pertaining to $137 \text{ fb}^{-1}$ .	62
A.1	List of data sets included in the analysis for the 2016 data taking period.	69
A.2	List of data sets included in the analysis for the 2017 data taking period.	70
A.3	List of data sets included in the analysis for the 2018 data taking period.	70
A.4	List of data sets included in the analysis for the 2016 data taking period.	71
A.5	List of data sets included in the analysis for the 2017 data taking period.	72
A.6	List of data sets included in the analysis for the 2018 data taking period.	73

# Chapter 1

## Introduction

### 1.1 The Standard Model and Beyond

Comprising 18 particles and numerous interactions between their fields the Standard Model provides a description of the fundamental interactions of nature. The Standard Model (SM) which is consistent with all empirical evidence is the leading theory of the universe.

Rather than providing a detailed description of the SM, the purpose of this introduction is to frame the analysis from a theoretical perspective. A table listing the particles appears below in figure 1.1.

Particles are represented by fields and interact within the theory. To frame the Standard Model the typical approach is to look at the Dirac Lagrangian and then establish  $U(1)$  interactions that have a conserved quantity (charge).

Noether originally proved that local transformation symmetries imply conserved currents which has extensive implications for particle physics and theories that predict quantum numbers and conserved quantities [1].

After analyzing the  $U(1)$  group, one typically extends the theory to include more fields and structures through higher dimensional groups. For a concise description, the gauge principle will be examined for  $U(1)$  and then expanding to  $SU(2)$ , before taking the product of these groups to form the Weinberg-Salam Model.

## Standard Model of Elementary Particles

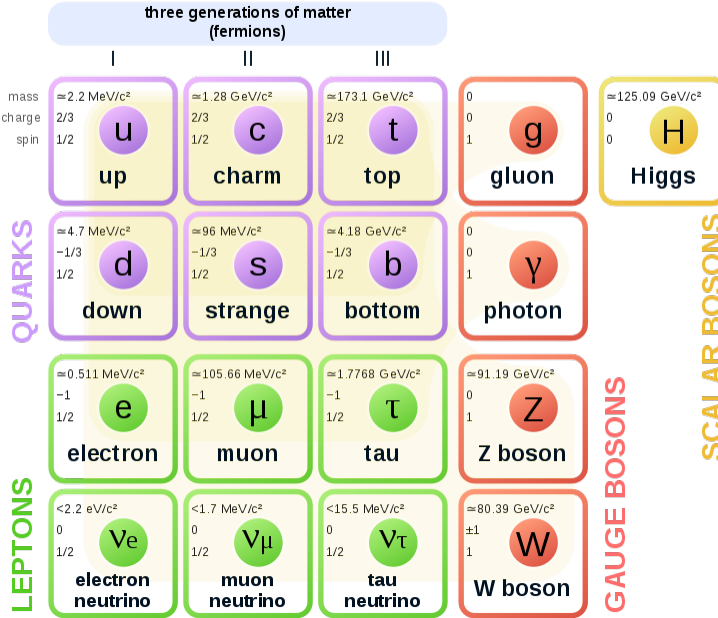


Figure 1.1: Standard Model particles

## 1.2 Gauge Principle, Yang Mills Theories, and the Weinberg-Salam Model

The gauge principle sets the stage for interactions between particle-fields in a theory. Much like in differential geometry and general relativity, there is a cost to interacting or changing through the action of a transformation. Consider the covariant derivative on a vector field  $V(x)$ .

$$\mathcal{D}_\mu V(x) \equiv \lim_{\Delta x \rightarrow 0} \frac{V_{||}(x + \Delta x) - V(x)}{\Delta x^\mu} \quad (1.1)$$

How the field changes under the transformation will determine the nature of the field. The connection terms that link the field follow from the transformation. A unitary operator can capture the parallel component in the covariant derivative. This operator carries the field and the *local* transformation law depending on the symmetries and complexity of the math structure that the unitary operator carries.

$$V_{||}(x + \Delta x) = U(x + \Delta x)V(x + \Delta x) \quad (1.2)$$

After expanding the unitary operator one can find the terms and phases that are carried under this transformation. For the  $U(1)$  group these actions give the electromagnetic field tensor and charge

conservation.

One defines the transformation and field then works out the form of the covariant derivative and examines how the gauge field transforms [2]. To put it generally

$$\Psi' = U(\vec{x})\Psi \text{ particle under local transformation} \quad (1.3)$$

$$\mathcal{D}^\mu = \partial^\mu + igB^\mu \text{ covariant derivative} \quad (1.4)$$

$$B'^\mu = UB^\mu U^{-1} + \frac{i}{g}(\partial^\mu U)U^{-1} \text{ gauge field transform.} \quad (1.5)$$

For  $U(1)$  with a unitary transformation of the form  $U(x) = \exp \frac{ig}{2}Y \cdot \beta(x)$

$$\Psi'(x) = (1 + \frac{ig}{2}Y \cdot \beta(x))\Psi \text{ particle field with local transformation} \quad (1.6)$$

$$\mathcal{D}_\mu = \partial_\mu + ieA_\mu \text{ covariant derivative} \quad (1.7)$$

$$A^\mu \rightarrow A^\mu + \frac{1}{g}(\partial^\mu \beta) \text{ gauge field transform.} \quad (1.8)$$

Notably, the commutator between the covariant derivatives yields the practical field that it carries. For the  $U(1)$  case, it is the electromagnetic field tensor.

$$[\mathcal{D}^\mu, \mathcal{D}^\nu] \Psi = ieF^{\mu\nu}\Psi \quad (1.9)$$

These relations are important when higher dimensional groups and more complex particle fields are considered. Yang-Mills theories take these components and analyzes them under groups like  $SU(2)$  or other special unitary groups. When one considers a local  $SU(2)$  transformation, the terms that show up are more rich than  $U(1)$ .

For  $SU(2)$  with a unitary transformation of the form  $U(x) = \exp \frac{ig}{2}\boldsymbol{\tau} \cdot \alpha(x)$

$$\Psi'(x) = (1 + \frac{ig}{2}\boldsymbol{\tau} \cdot \boldsymbol{\alpha})\Psi \text{ particle field with local transformation} \quad (1.10)$$

$$\mathcal{D}_\mu = \partial_\mu - \frac{i}{2}g\boldsymbol{\tau} \cdot \mathbf{W}_\mu(x) \text{ covariant derivative} \quad (1.11)$$

$$\boldsymbol{\tau} \cdot \mathbf{W}_\mu \rightarrow \boldsymbol{\tau} \cdot \mathbf{W}_\mu + \frac{1}{g}\boldsymbol{\tau} \cdot (\partial_\mu \boldsymbol{\alpha}) - \boldsymbol{\tau} \cdot (\boldsymbol{\alpha} \times \mathbf{W}_\mu) \text{ gauge field transform.} \quad (1.12)$$

Now if we consider  $SU(2) \times U(1)$  and build states out of that with a coupling of only one component in the  $SU(2)$  interaction then add a scalar field, the structure is there for the Weinberg-Salam Model.

### 1.3 The Higgs Mechanism

As mentioned in the previous section, taking the  $SU(2) \times U(1)$  groups with an additional scalar field and defining their local transformations indicates the interactions within the electroweak Weinberg-Salam model. The fields transform the same way as before; however, Higgs and others thought of adding a scalar field to the theory. In order to see the interactions with the scalar field we need to see how it transforms. The scalar field interacts with the other fields under the  $SU(2)$  and the  $U(1)$  transformations.

$$\begin{pmatrix} \phi^+ \\ \phi^0 \end{pmatrix} = \frac{1}{\sqrt{2}} \begin{pmatrix} \phi_3 + i\phi_4 \\ \phi_3 - i\phi_4 \end{pmatrix} \quad (1.13)$$

This scalar field transforms in the following way under  $U(1)$  and  $SU(2)$  transformations

$$\begin{pmatrix} \phi^+ \\ \phi^0 \end{pmatrix} \rightarrow \begin{pmatrix} e^{ig\frac{\beta}{2}} & 0 \\ 0 & e^{ig\frac{\beta}{2}} \end{pmatrix} \begin{pmatrix} \phi^+ \\ \phi^0 \end{pmatrix} \quad (1.14)$$

$$\begin{pmatrix} \phi^+ \\ \phi^0 \end{pmatrix} \rightarrow e^{\frac{ig}{2}\tau \cdot \alpha} \begin{pmatrix} \phi^+ \\ \phi^0 \end{pmatrix} \quad (1.15)$$

$$\mathcal{D}_\mu \phi = \partial_\mu \phi - \frac{i}{2} g \tau \cdot \mathbf{W}_\mu \phi - \frac{i}{2} g' \beta_\mu \phi, \quad (1.16)$$

yielding the Higgs field Lagrangian component

$$\mathcal{L} = (\mathcal{D}^\mu \phi)^\dagger (\mathcal{D}_\mu \phi) + \frac{m_h^2}{2} \phi^\dagger \phi - \frac{\lambda}{4} (\phi^\dagger \phi)^2. \quad (1.17)$$

The Higgs potential contains the typical “Mexican hat” shape and the kinetic term holds interesting interactions and implications for the gauge bosons in the theory. All together the Weinberg-Salam model with the Higgs field is [3]

$$\mathcal{L} = \bar{L} i \gamma^\mu \mathcal{D}_\mu L + \bar{R} i \gamma^\mu \mathcal{D}_\mu R + (\mathcal{D}^\mu \phi)^\dagger (\mathcal{D}_\mu \phi) \quad (1.18)$$

$$\begin{aligned} &+ \frac{m_h^2}{2} \phi^\dagger \phi - \frac{\lambda}{4} (\phi^\dagger \phi)^2 - G_e (\bar{L} \phi R + \bar{R} \phi^\dagger L) \\ &- \frac{1}{4} G_{\mu\nu}^{(W)} \cdot G^{(W)\mu\nu} - \frac{1}{4} F_{\mu\nu}^{(B)} F^{(B)\mu\nu}. \end{aligned} \quad (1.19)$$

The Weinberg-Salam Model has major implications: the terms  $L$  and  $R$  along with their hermitian conjugates form an interaction with the Higgs field giving electrons mass. This equation along with the shape of the Higgs potential imply spontaneous symmetry breaking and interactions that produce massive vector gauge bosons and massless photons.

## 1.4 Higgs Doublet Models

The Standard Model can naturally be extended by giving more complexity to the fields. Suppose that there were multiple scalar fields instead of just the single Higgs field  $\phi$ , then one can consider adding another component, thus making it a doublet. Adding the doublet, and working out the relations for the field, the most general two-Higgs doublet model (2HDM) Higgs potential is found in equation 1.20 [4].

$$\begin{aligned} V = & m_1^2 |H_1|^2 + m_2^2 |H_2|^2 + \frac{\lambda_1}{2} |H_1|^2 + \frac{\lambda_2}{2} |H_2|^2 \\ & + \lambda_3 |H_1|^2 |H_2|^2 + \lambda_4 |H_1^\dagger H_2|^2 \\ & + \frac{\lambda_5}{2} \left( (H_1 H_2)^2 + c.c. \right) + m_{12}^2 (H_1 H_2 + c.c.) \\ & + \left( \lambda_6 |H_1|^2 (H_1 H_2) + c.c. \right) \\ & + \left( \lambda_7 |H_2|^2 (H_1 H_2) + c.c. \right) \end{aligned} \quad (1.20)$$

Expanding around the minimum of the potential yields two doublets with vacuum expectation values  $v_1$  and  $v_2$ , which are usually mixed under a rotation parameter  $\tan \beta = v_1/v_2$ . After one carries out the interactions with the SM gauge bosons, which consume the complex field components and a neutral pseudoscalar combination of scalar Higgs field components, the surviving three real degrees of freedom yield one neutral pseudoscalar mass eigenstate along with two neutral scalar mass eigenstates.  $A$  will denote the pseudoscalar,  $h$  for the lighter neutral SM like Higgs, and  $H^0$  for the remaining scalar. As with the notation for fields that interact with the potential, the rotation matrix that mixes these scalars into the components that interact under the potential is parametrized by the continuous parameter  $\alpha$ .

$$\begin{pmatrix} h \\ H^0 \end{pmatrix} = \begin{pmatrix} -\sin \alpha & \cos \alpha \\ \cos \alpha & \sin \alpha \end{pmatrix} \begin{pmatrix} H_{1,R}^0 \\ H_{2,R}^0 \end{pmatrix} \quad (1.21)$$

In the literature this parameter is important because  $\tan \beta$  and  $\alpha$  set the possible couplings to SM particles. Next, if a complex scalar singlet is added, couplings to SM fermions and bosons are supported [5].

$$S = \frac{1}{\sqrt{2}} (S_R + iS_I) \quad (1.22)$$

The scalar singlet doesn't have Yukawa couplings, but rather couples to  $H_{1,2}$ . Through its mixing with  $H_{1,2}$  the singlet can couple to SM fermions.

A possible coupling that preserves the SM Higgs by keeping  $\theta_a$  small could be defined as

$$a \equiv \cos \theta_a S_i + \sin \theta_a A, \quad \theta_a \ll 1 \quad (1.23)$$

This allows for decays like  $h \rightarrow aa \rightarrow X\bar{X}YY\bar{Y}$ , where  $X$  and  $Y$  are SM fermions or bosons. Looking into the phase space where the mixing is light then frames the Higgs pseudoscalar analysis in a region with little SM resonance—making it also a general search for any beyond SM (BSM) phenomena. There are terms in the effective Lagrangian that support the  $h \rightarrow aa$  decays:

$$\begin{aligned} \mathcal{L} &\subset g_{hAA} hAA + \lambda_S |S^2|^2 \\ &\subset g_{hAA} \sin^2 \theta_a haa + 4\lambda_S v_s \sin \zeta_1 \cos^2 \theta_a haa \end{aligned} \quad (1.24)$$

here  $\zeta$  is just the angle that mixes the singlet with the SM Higgs (needed because of the added state). These interactions give rise to different scenarios that favor certain SM fermions and bosons. According the literature, four distinct scenarios are typically entertained. The scenarios, supported by the effective Lagrangian 1.24, yield branching fractions as a function of  $a$ -mass and  $\tan \beta$ . These are enumerated below:

- Type I: Fermions couple only to the  $H_2$  field and are independent of  $\tan \beta$ , pseudoscalar coupling are proportional to the SM Higgs (final state of the fermions) represented in figure 1.2.
- Type II: Down-type fermions are particularly favored supporting more NMSSM models, and is dependent on  $\tan \beta$  represented in figure 1.3.
- Type III: Branching ratios are directly dependent on  $\tan \beta$  and are emphasized when more than one lepton is considered.  $\tau^+ \tau^-$  can dominate in this scenario represented in figure 1.4.
- Type IV: Dependent on  $\tan \beta$ , for  $\tan \beta < 1$  branching ratios for  $b\bar{b}$ ,  $c\bar{c}$ , and  $\tau^+ \tau^-$  are similar (supports  $2b2\tau$ ) represented in figure 1.5.

## 1.5 Previous and present searches in 2HDM+S models

As shown in the previous section, the Higgs couples to all SM particles and also to new particles provided that the new particles have mass. BSM theories contain ample room for the Higgs to

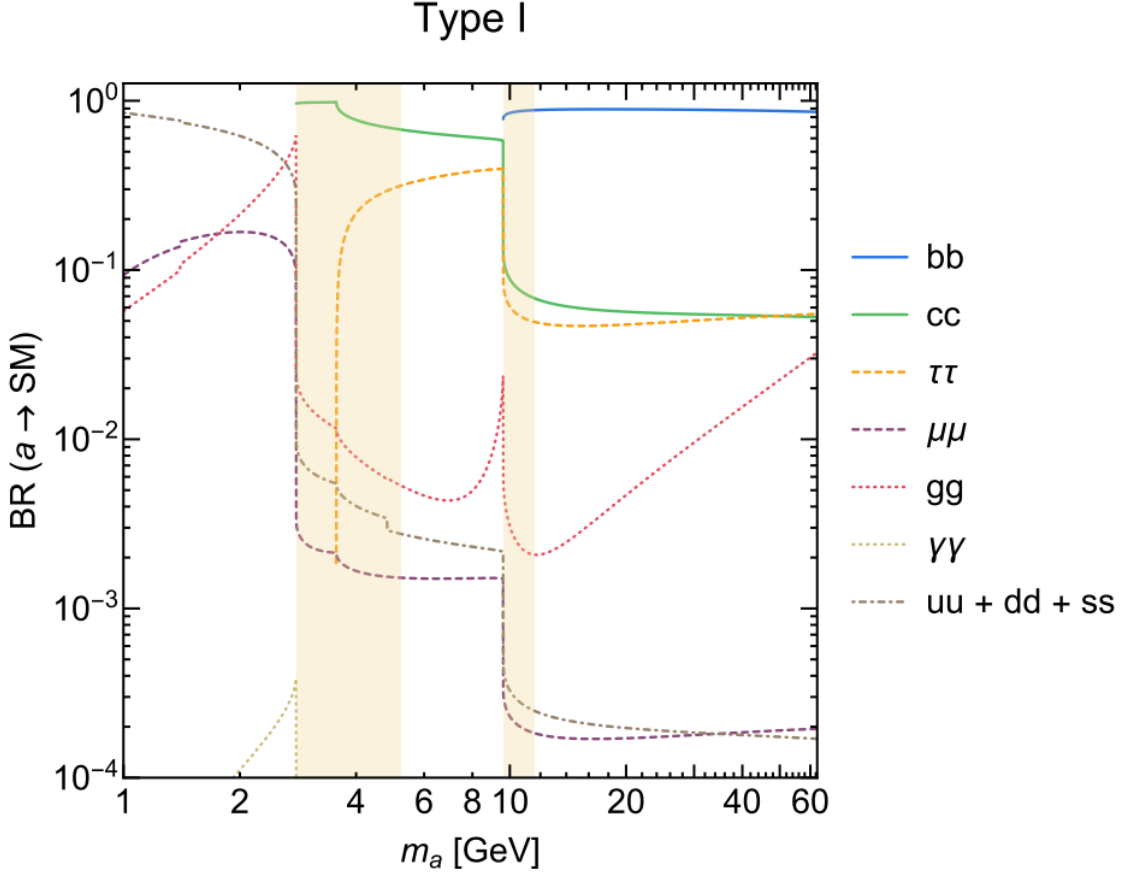


Figure 1.2: Type I 2HDM+S scenario branching fractions [4]

couple to particles beyond the SM, making the Higgs an excellent window to investigate any physics beyond the SM. Notably, the two Higgs doublet model (2HDM) with its extension of a scalar singlet is considered (2HDM+S). These types of BSM theories can solve the  $\mu$  coupling problem in Super Symmetry (SUSY), while maintaining general support of SUSY (Holomorphy), Axion-like Models (Peccei-Quinn), electroweak baryogenesis and several Grand Unified Theories (GUTs) [4].

A representative diagram showing the physics process and the branching ratio as a function of  $\tan\beta$  is shown in figure 1.6. This pseudoscalar Higgs search for “resolved”  $a$  particles in the range of 20 to 60 GeV is a good search for new physics. In 2016 this general search was carried out with  $35.9 \text{ fb}^{-1}$  of data and new competitive limits were set in reference [6].

Given the potential for improvement in the limits for different 2HDM+S types, extending this search using the full RunII dataset is motivated.

The branching ratios change based on the function of  $\tan\beta$  depending on the type of model under investigation. In particular, we look at types 1-4. Type III is expected to be most sensitive

as it maintains a larger branching ratio compared to other decay modes over the range of the pseudoscalar masses when focusing on the final state of two muons and two tau leptons.

In addition to the search for this model, any deviation from the SM prediction in the effective mass range would also be found.

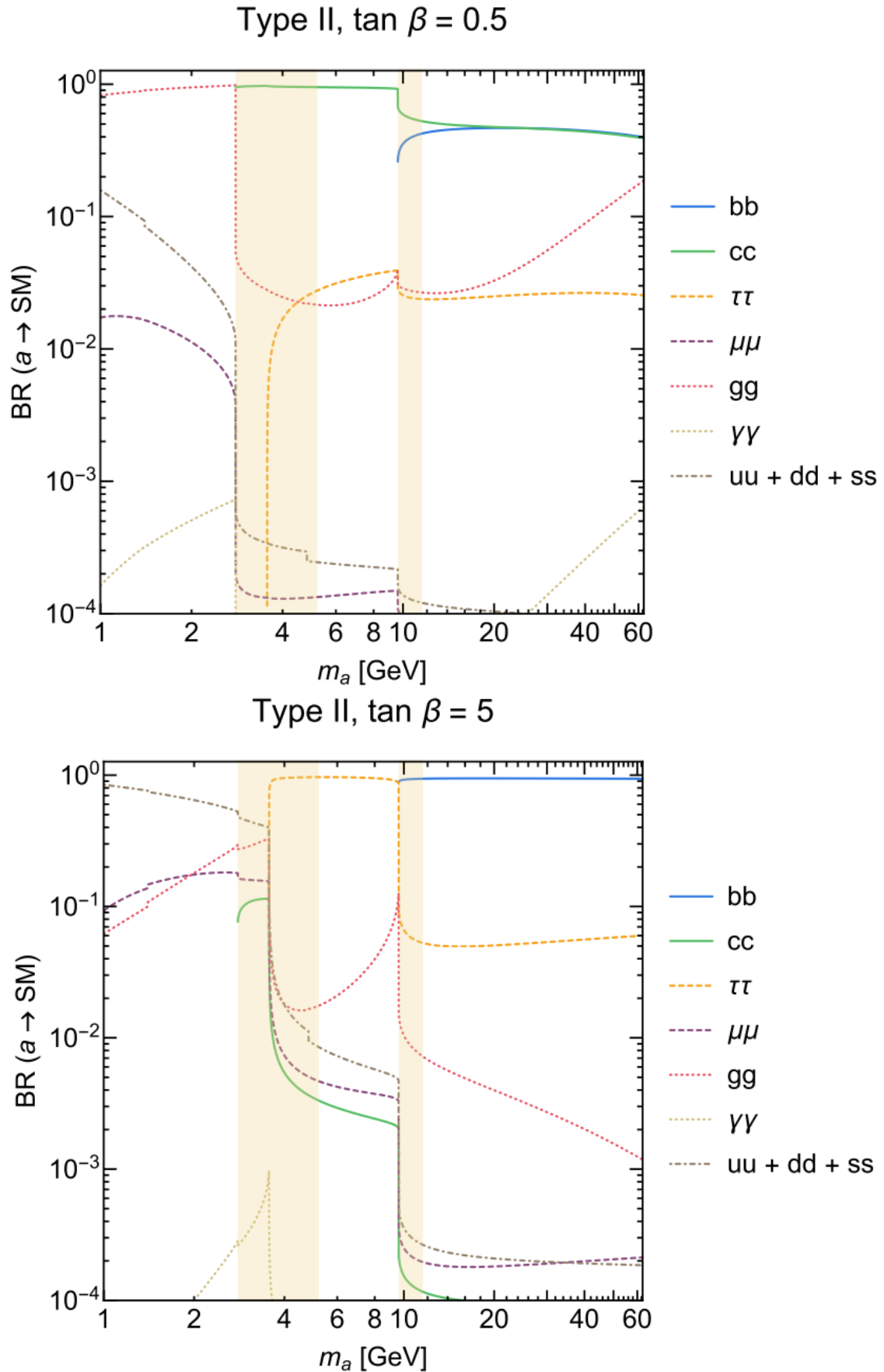


Figure 1.3: Type II 2HDM+S scenario branching fractions [4]

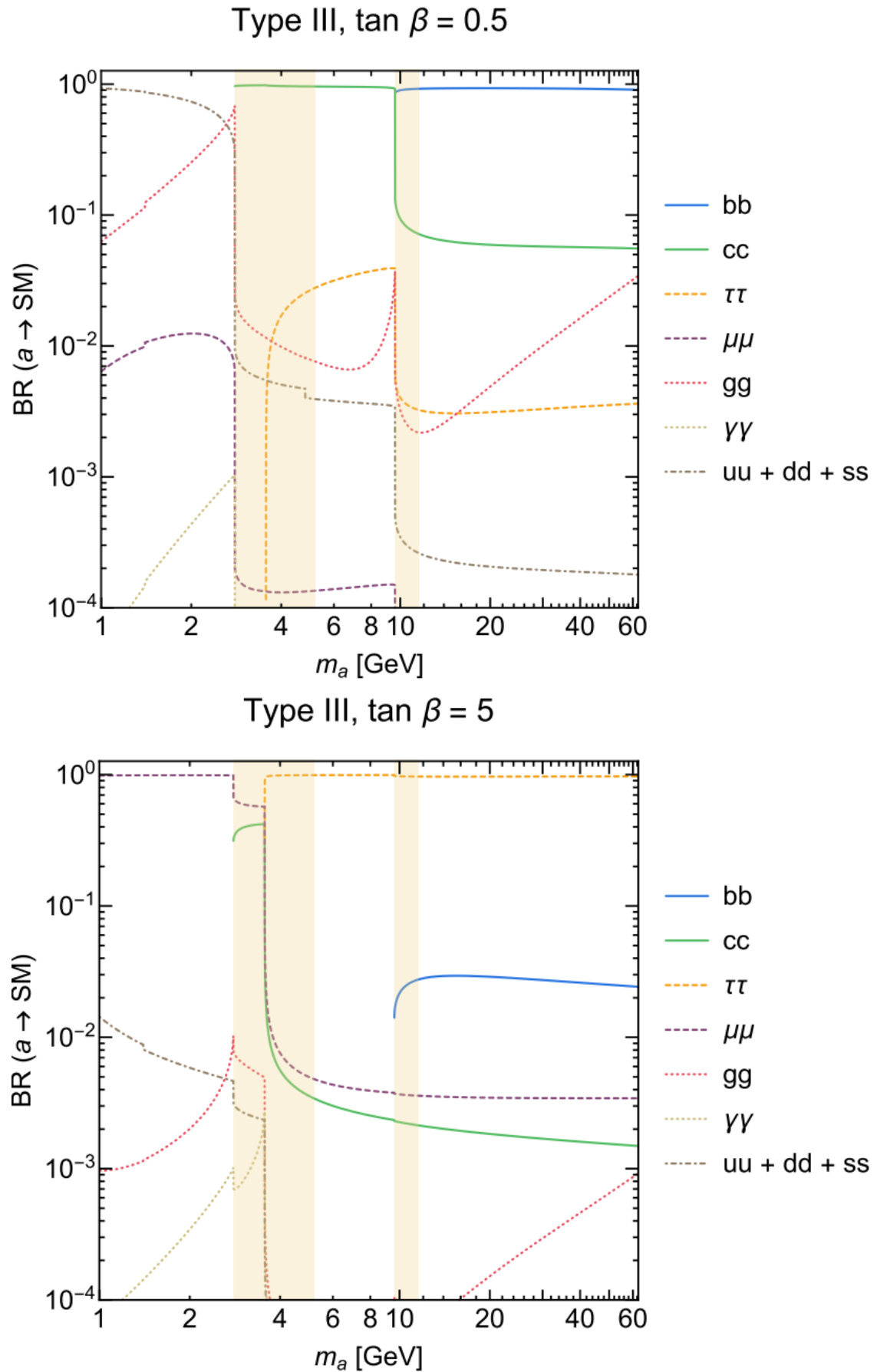


Figure 1.4: Type III 2HDM+S scenario branching fractions [4]

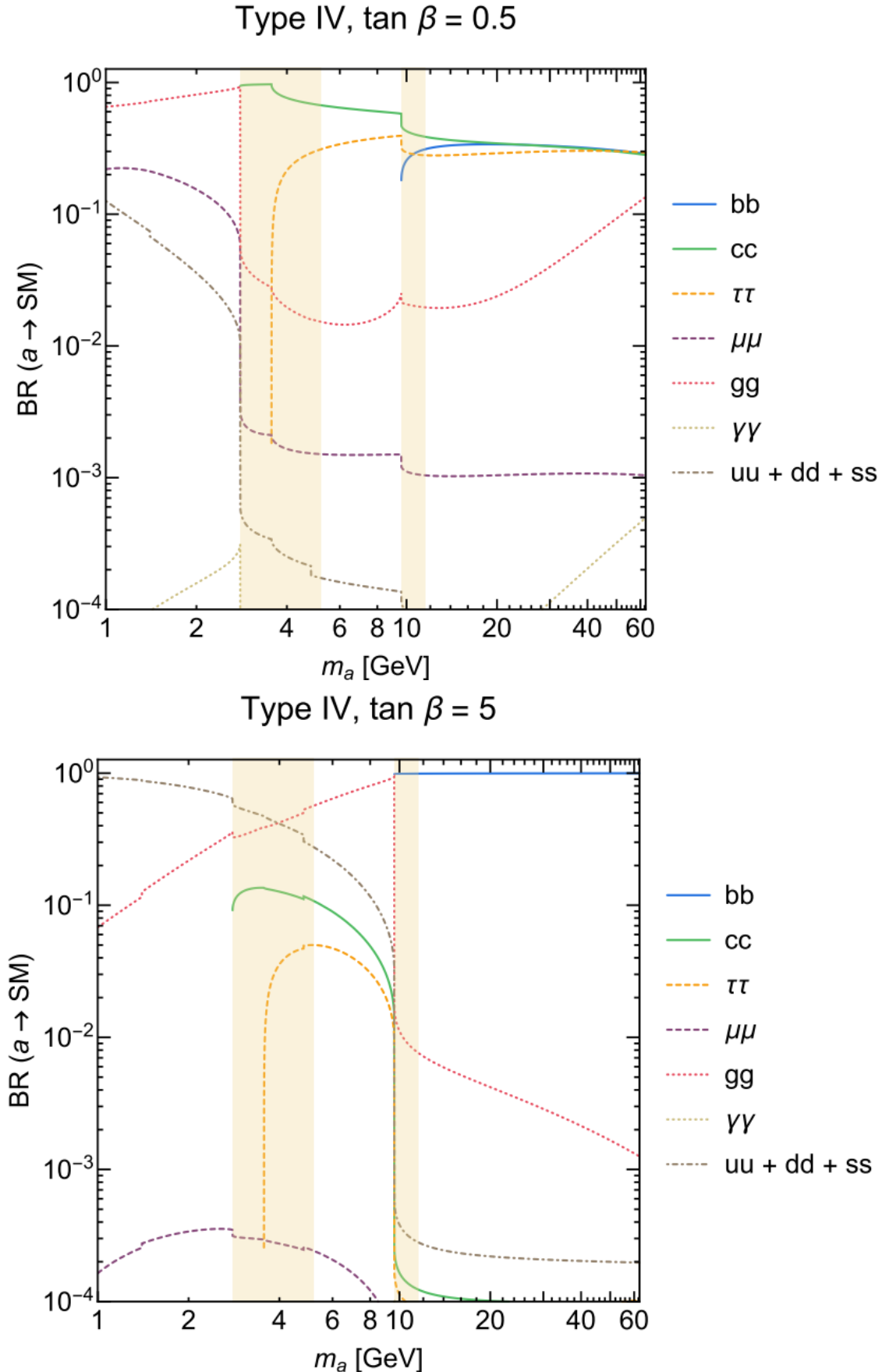


Figure 1.5: Type IV 2HDM+S scenario branching fractions [4]

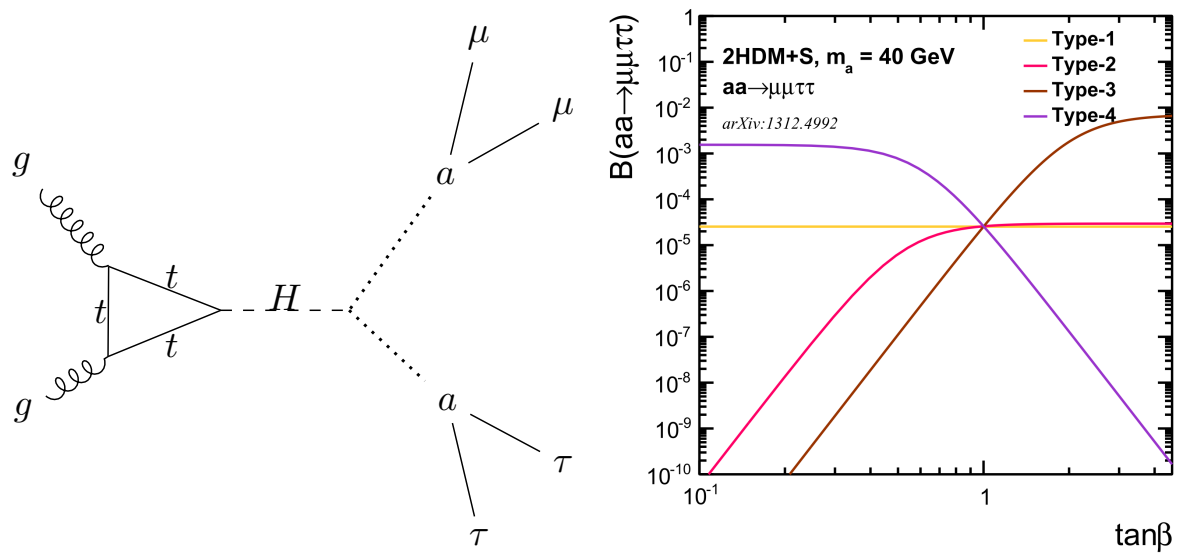


Figure 1.6: Diagram of Higgs decay to pseudoscalar  $a$  particles (Left) and branching ratios for pseudoscalar production in different  $\tan\beta$  scenarios and different 2HDM+S Types (right)

## Chapter 2

# CERN, The LHC, and The CMS Detector

### 2.1 CERN and the Large Hadron Collider

The *organisation européenne pour la recherche nucléaire* or CERN conducts the world's frontier particle physics experiments. It's a coalition of scientists representing numerous countries around the world who work together for a greater understanding of the universe. CERN hosts the Large Hadron Collider, currently the largest particle collider in the world. It is 27 km in circumference and holds eight experimental caverns 150 meters underneath the earth. Accelerator physicists and engineers strive to provide high energy collisions along these eight sites. Monumental effort is made to guide the beam, utilizing more than 1500 superconducting magnets to steer, press, and shape the accelerating protons. Crossing points facilitated by crab cavities force these particles to cross, collide, and interact at the caverns where the experiments take data. Multiple campaigns for particle physics are done such as low intensity fills, lead-lead collisions, and proton collision. The Compact Muon Solenoid (CMS) is the general purpose proton-proton detector located at P5 in Cessy, France that took the data that will be analyzed in this dissertation [7].

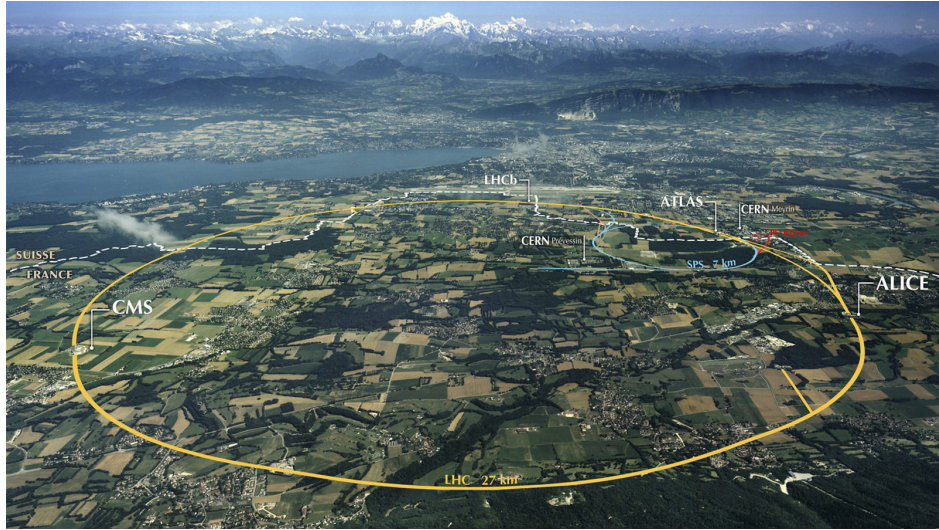


Figure 2.1: Overview of the Large Hadron Collider spanning Switzerland and France - Maximilien Brice, CERN

## 2.2 The Compact Muon Solenoid detector

At around 14,000 tonnes, the CMS detector may not seem like it would be compact; however, it is quite dense. As shown in the diagram, the detector contains many sub-detector systems and also features the most powerful solenoid magnet ever made for its size. At 6 meters inner diameter, and a combined weight of the solenoid and the steel return yolk of 12,500 tonnes, the solenoid is the central feature of the Compact Muon Solenoid (CMS) 2.2. Within the solenoid volume, there is the silicon pixel and strip tracker, a lead tungstate crystal electromagnetic calorimeter (ECAL), and a brass plus scintillator hadron calorimeter (HCAL). Each tracker and calorimeter is composed of a barrel and two endcap sections. Forward calorimeters extend the pseudorapidity— $\eta$ —coverage provided by the barrel and endcap detectors. Muons are detected in gas-ionization chambers embedded in the steel flux-return yoke outside the solenoid.

The coordinate system that is adopted is cylindrical in nature starting at the interaction or nominal collision point. The  $y$ -axis points vertically outward toward the sky, the  $x$ -axis tangent to the Earth, and the  $z$ -axis along the direction of the beam pipe. The azimuthal angle  $\phi$  and the radial coordinate  $r$  in the  $x$  and  $y$  plane, and the polar angle  $\theta$  measured from the  $z$  axis comprise the angular coordinate interpretation. Often pseudorapidity is used to describe angular distance

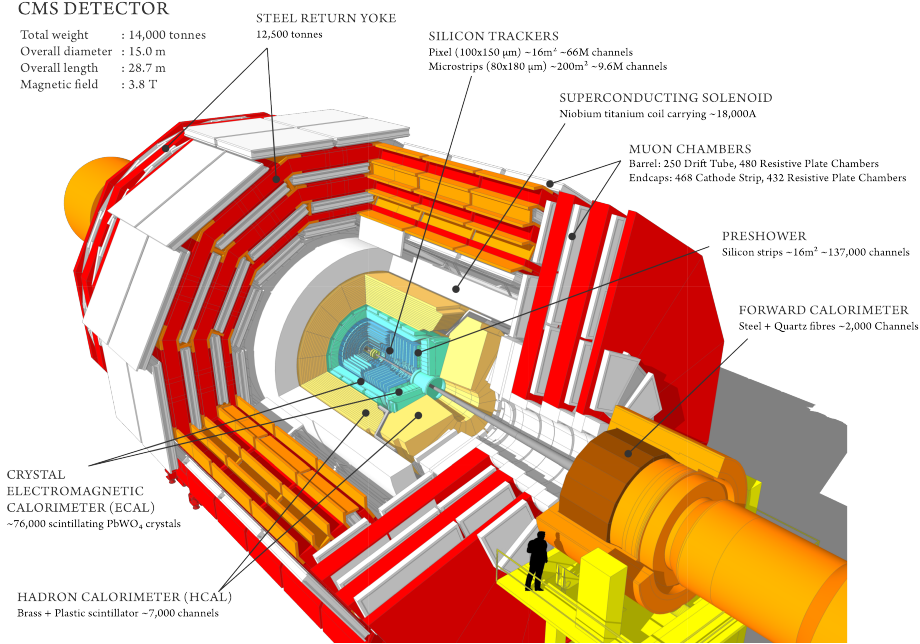


Figure 2.2: The CMS detector full 3D image with all subsystems labeled

from the beam pipe—useful in detector segmentation in forward and barrel regions:

$$\eta = -\ln \tan(\theta/2) \quad (2.1)$$

A more detailed description of the CMS detector can be found in Reference [8].

## 2.3 Subdetector Systems

Several subdetector systems play an important role in the identification of muons and tau leptons that are used in the analysis. Some impressive infrastructure that supports physics at CMS and physicists worldwide will also be described. While all subdetector systems are important to event reconstruction in CMS, there are several detectors that contribute to the particles that are identified in the pseudoscalar search. These are the tracker system, electromagnetic calorimeter, the hadronic calorimeter, and muon system.

### 2.3.1 Tracker

Working around silicon for almost 10 years, I have a slight bias in presenting this sub-detector system and I plan to share more details in this section than others.

The tracker comprises several groups of silicon detectors.

Going outward from the beam pipe and central interaction points, there is the pixel detector system and then the silicon tracker system. For better coverage, both are divided into barrel and endcap components.

A silicon detector is a detector that can identify charge by disturbing the electron lattice that exists on the silicon itself. Typically, multiple band gaps are created through the process of lithography which adds artificial impurities of p-type (holes) or n-type (electrons). This process is known as “doping”. When a minimum ionizing particle (MIP) disturbs the latent charge—set by the bias voltage on the sensor—there is a current generated in the n and p type components (Shockley Equation):

$$\mathcal{J}_{n,p} = \frac{q_0 D_{n,p} d_{n,p}}{L_{n,p}} \left( e^{\frac{q_0 V}{k_B T}} - 1 \right) \quad (2.2)$$

For reference,  $L_{n,p}$  is the diffusion length,  $D_{n,p}$  the diffusion coefficients,  $d_{n,p}$  the charge/hole density,  $V$  the bias voltage,  $q_0$  the standard charge unit,  $k_B$  the Boltzmann constant, and  $T$  the temperature. This sets in motion the current which will be collected later by each of the channels. A graphical display of surface current dissipation using TCAD (technology computer aided design) as a function of time can be displayed in figure 2.3. A wealth of silicon information can be found in reference [9].

## Pixel Detector

Sitting closest to the beam pipe is the pixel detector system. It contains the Barrel Pixels (BPIX) and the Forward Pixel System (FPIX). Similar 2x8 silicon detector modules make up both the BPIX and FPIX systems.

In 2016, the phase 1 Forward Pixel System (FPIX) was constructed and tested. At Purdue University, an Aerotech robotic gantry control system was used to join a hybrid flex circuit to a bump-bonded silicon pixel module. After wirebonding, the gantry system encapsulated the wirebonds for protection from corrosion and magnetic field resonance. Purdue was one of the manufacturing sites alongside University Nebraska-Lincoln.

Using LabVIEW, we developed a state machine to assemble and encapsulate these pixel modules. Pattern recognition and a linear algebra suite were developed to perform precise operations at a 50 micron resolution. An example of a post encapsulated token bit manager - which resides on top of

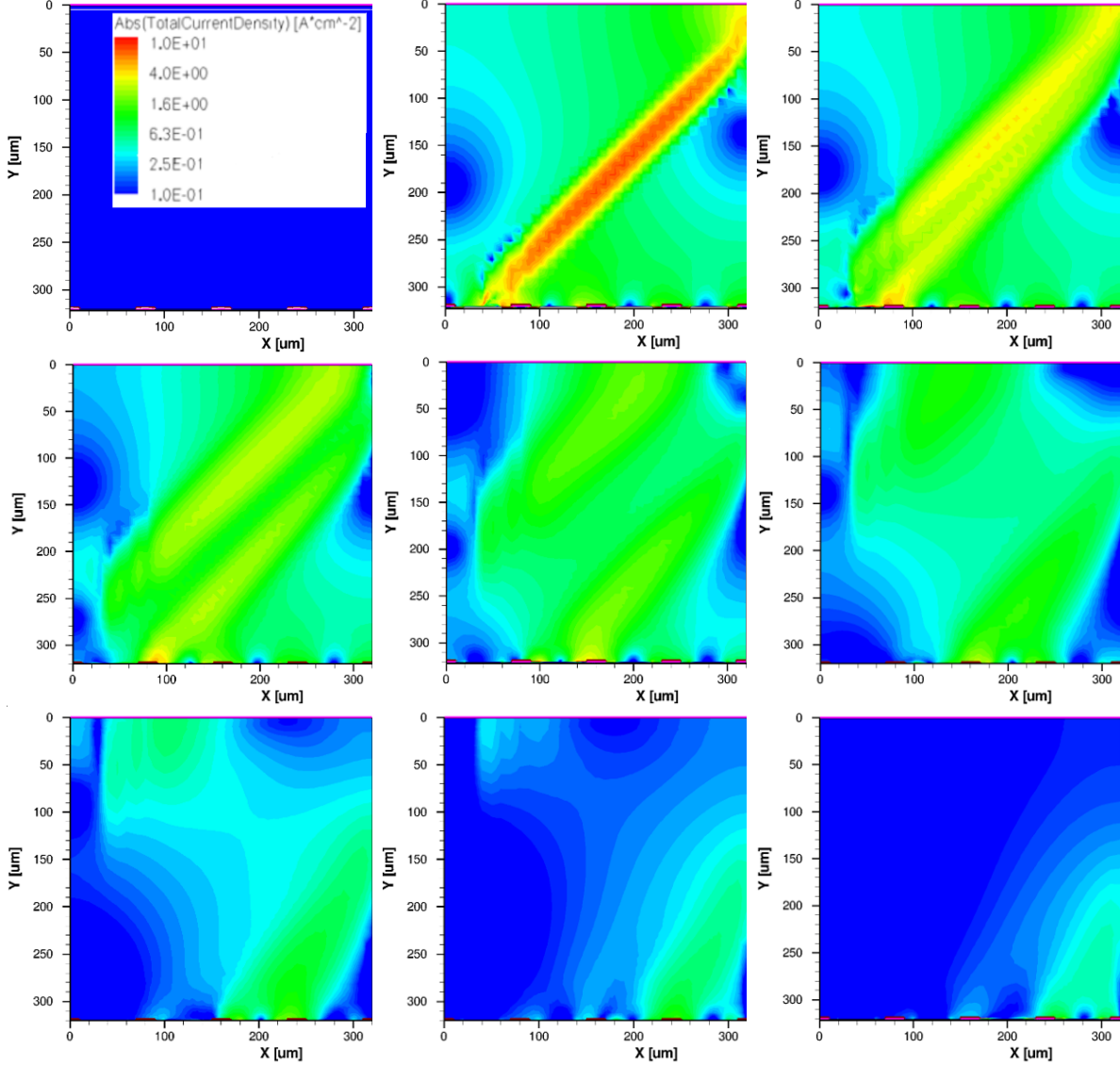


Figure 2.3: (simulation) MIP particle traveling across a silicon strip sensor at  $45^\circ$  over time from 0.0, 1.1, 1.5, 2, 3, 4, 5, 6, 7 nanoseconds. The induced surface current dissipates and would be collected by the channels of the silicon module [9].

the high density interconnect of a completely assembly module - is shown in figure 2.4.

In 2017, this system was installed in CMS, increasing the number of disks to three and the number of barrel layers to four. Due to the experimental design of CMS, the inner sub-detector systems may be taken out of the inner body—the solenoid—and serviced. These forward disks are especially important for reconstruction of events with boosted charged particles. They are located in high regions of  $\eta$  and are overlapped for improved hermeticity.

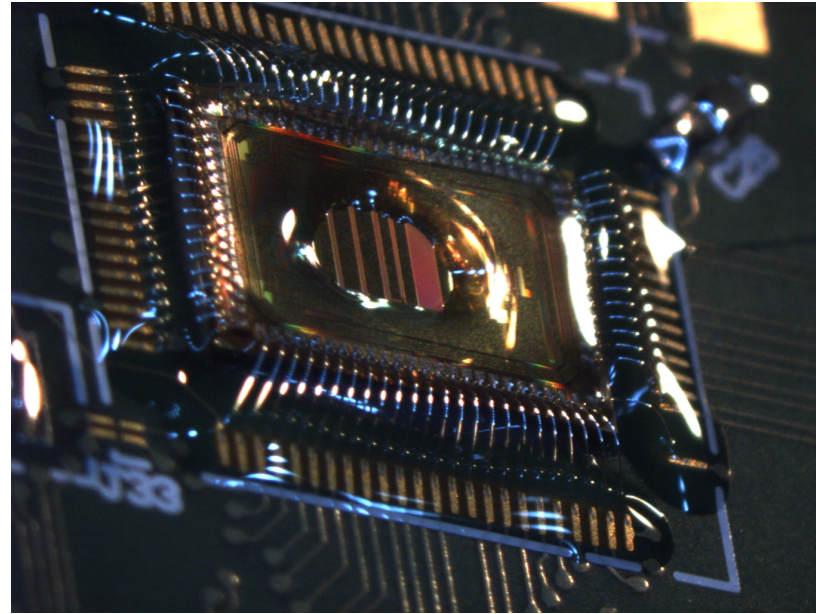


Figure 2.4: encapsulated token bit manager of a forward pixel module currently installed in CMS

### Silicon Tracker

The silicon tracker comprises larger silicon modules by area than the pixel system and is located further from the beam pipe. A representative layout of the silicon tracker and the pixel system can be found in figure 2.3.1 [8].

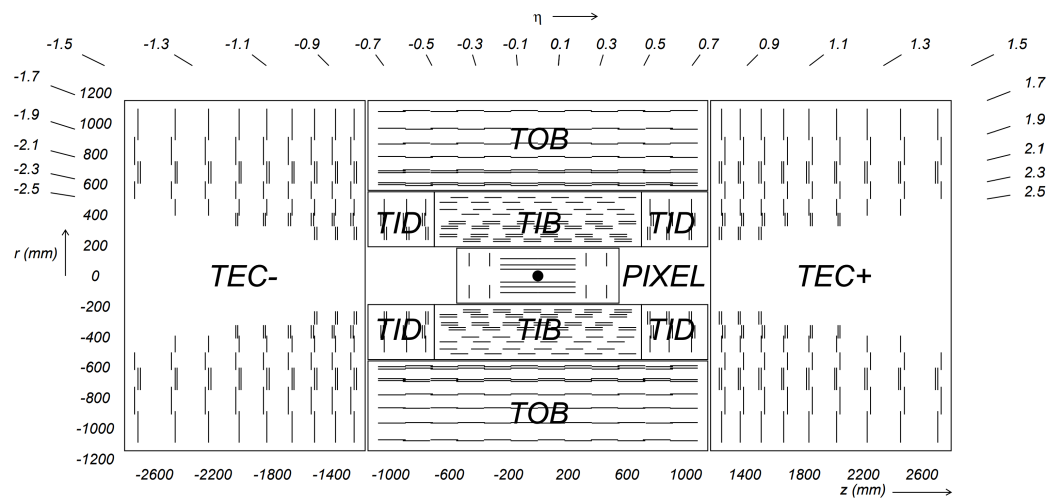


Figure 2.5: The silicon tracker system, consisting of the inner pixel system (BPIX and FPIX), The Tracker End Caps (TEC), Tracker Inner Detector(TID), Tracker Inner Barrel (TIB), and the Tracker Outer Barrel (TOB) by position in  $r$ ,  $z$  , and  $\eta$  [8]

### 2.3.2 Electronic Calorimeter

The principal components of the ECAL are the 76200 lead tungstate ( $\text{PbWO}_4$ ) crystals, which scintillate and absorb energy from incoming particles. These detector components are also separated in barrel and endcap regions. Photomultipliers are attached to the crystal to detect the light signal. The relative energy resolution is

$$\left(\frac{\sigma}{E}\right)^2 = \left(\frac{2.8\%}{\sqrt{E}}\right)^2 + \left(\frac{0.12}{E}\right)^2 + (0.3\%)^2$$

The 2.8% reflects the stochastic term, 0.12 the Noise term and 0.3% the constant term in the fit during calibration with a 440 nm blue laser over 11.5 days [8, 9].

### 2.3.3 Hadronic Calorimeter

The Hadronic Calorimeter is the primary sub-detector to identify “jets”, which are collections of hadronic processes. These jets have subcomponents of densely clustered energy.

Plates are used to induce particle showers, which can be identified through scintillation. Similar to the ECAL, these signals are read out through photodiodes as well.

There are barrel (HB) and endcap (HE) inside the solenoid. The Hadronic Outer (H0) and super forward detector (HF) sit outside the solenoid. An overview of the HCAL system is shown in figure 2.6 [8, 9].

### 2.3.4 Muon Chambers

The chambers comprises drift tubes which cover a pseudorapidity region ( $|\eta| < 1.2$ ) split into 4 stations in the flux return plates.

In the higher  $|\eta|$  regions, cathode strip chambers (CSCs) are used and preferred for their fast response time, fine segmentation, and radiation resistance [10]. For a visual representation of a cross section of the muon system please refer to figure 2.7.

Notably, the track of the muon is bent inside the solenoid by the Lorentz force, and then reverses after it exits.

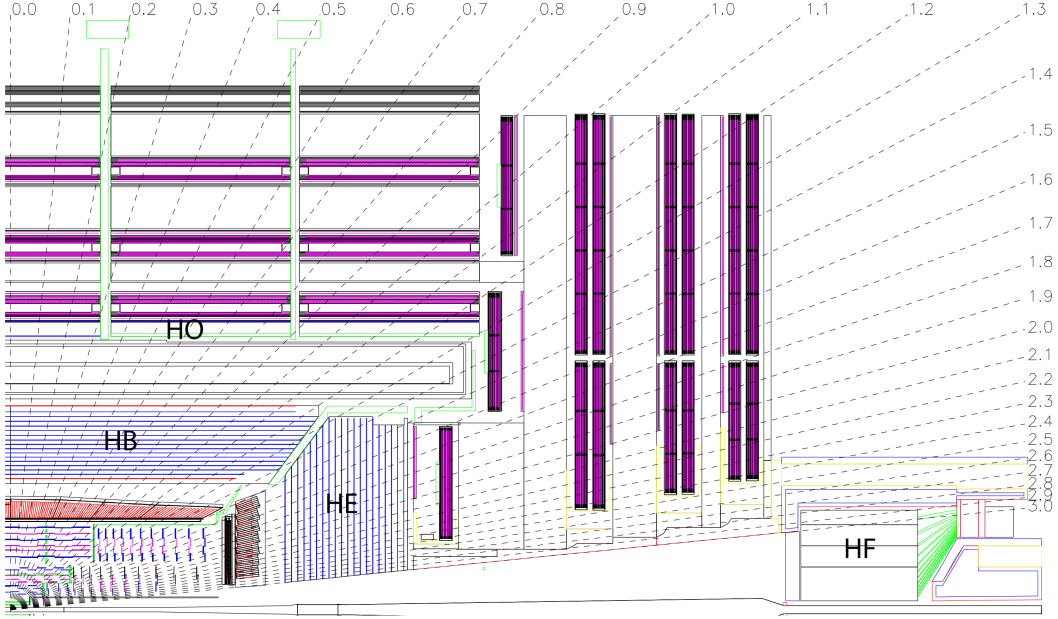


Figure 2.6: Overview of the HCAL system from the  $z-\eta$  plane showing the hadron barrel (HB), encap(HE), outer (HO), and the forward (HF) subsystems [8]

## 2.4 Level 1 Trigger System and High Level Trigger

Particle collisions happen at a rate of 40 MHz with 22 minimum bias events expected to occur on average, making full readout impossible to store because of the high bandwidth [7, 11]. The Level 1 Trigger System and High Level Trigger work to reduce these rates by recording events that physicists agree are worth saving.

The Level-1 trigger system can process data close to the beam collision rate. It is the first online event selection that uses many subsystems in tandem to decide whether or not to save the event. Algorithms are in place that take input from the calorimeters, the muon systems, and other detectors in the form of “trigger primitives” and use pattern recognition along with fast summing techniques to trigger on the event. Many of these algorithms are run on Field Programmable Gate Arrays (FPGAs). These decisions are concatenated at the CMS Global Trigger (GT) which signals at the front end electronics, 144 beam crossing after the interaction. The Level-1 system also outputs physics objects from the algorithms so preliminary leptons, jets, missing transverse energy among other objects can be used in algorithms operating at the High Level Trigger [11].

The HLT maximum input rate is 100KHz and the output is in the order of kHz. It is constrained by the processing power available, the data recording and transfer rate of Tier 0, and the prompt

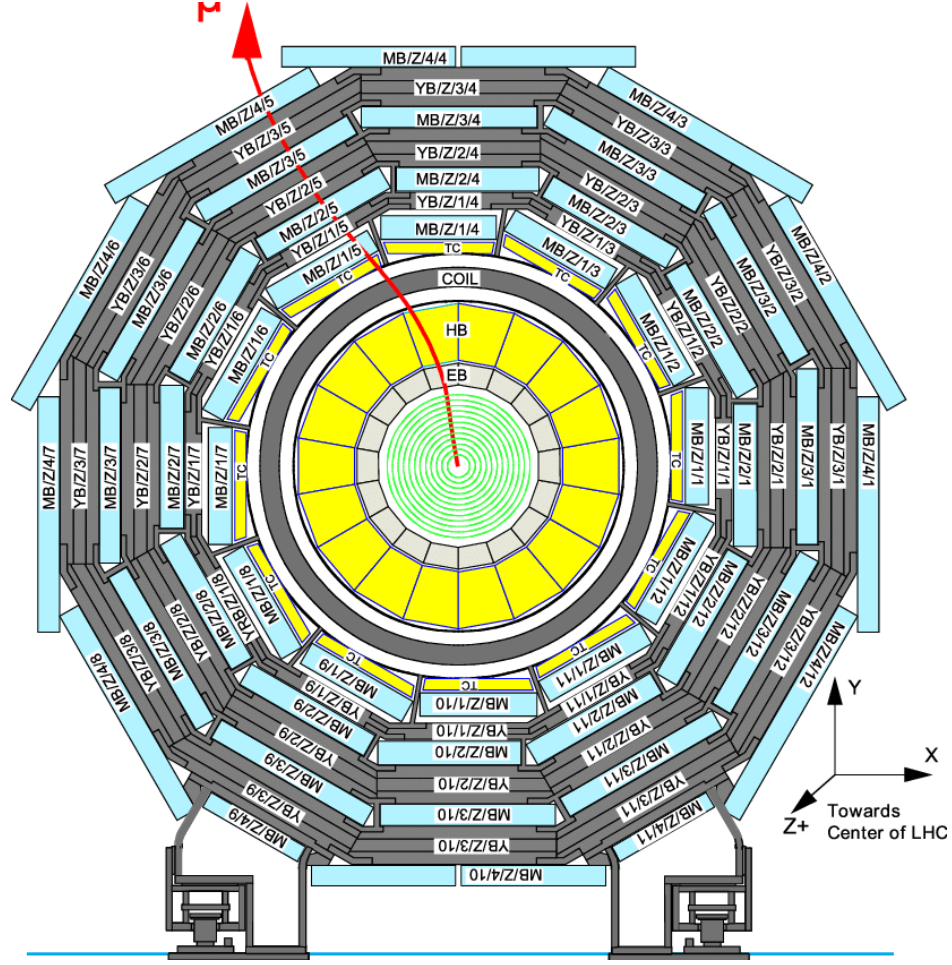


Figure 2.7: Muon system involving multiple subdetector systems: tracker, solenoid, and the muon gas chambers around the iron yoke (grey) - Maximilien Brice, CERN

reconstruction algorithms. Late in Run II “Scouting” and “Parking” data were used to help increase bandwidth. “Scouting” reduces the event size by saving only objects reconstructed at HLT and “Parking” avoids prompt reconstruction by saving lower level information [12].

## 2.5 Particle Flow Algorithms

The event data model requires association of higher level physics objects—like leptons—with energy deposits and tracks in the detector.

The particle flow algorithm at CMS has the goal of associating these primary detector signatures with these particles so that direct comparison to Monte Carlo simulation can be done.

The list includes, but is not limited to jets, missing transverse energy, taus, charged-leptons,

photon isolation, and bottom quark jet identification.

To outline the algorithm: Charged particle tracks reconstructed in the tracker, energy clusters from the ECAL, HCAL, and preshower detector (ES), and forward calorimeter (HF) are topologically linked into blocks. The linking is done through many associations of energy deposits and tracks in  $\phi, \eta$  space. These blocks are then interpreted as particles and central energies are calibrated depending on their composition. This information and an exhaustive explanation can be found in reference [13].

## 2.6 Computational Infrastructure

Over 200 peta-bytes of information have been gathered in Run II. The way data is gathered, computed, and stored should all be highlighted.

At CMS above ground there are 32,000 24-core processors at Tier 0 (T0). This is where higher level reconstruction of physics objects is done. A schematic overview of the infrastructure can be found in figure 2.8 [14].

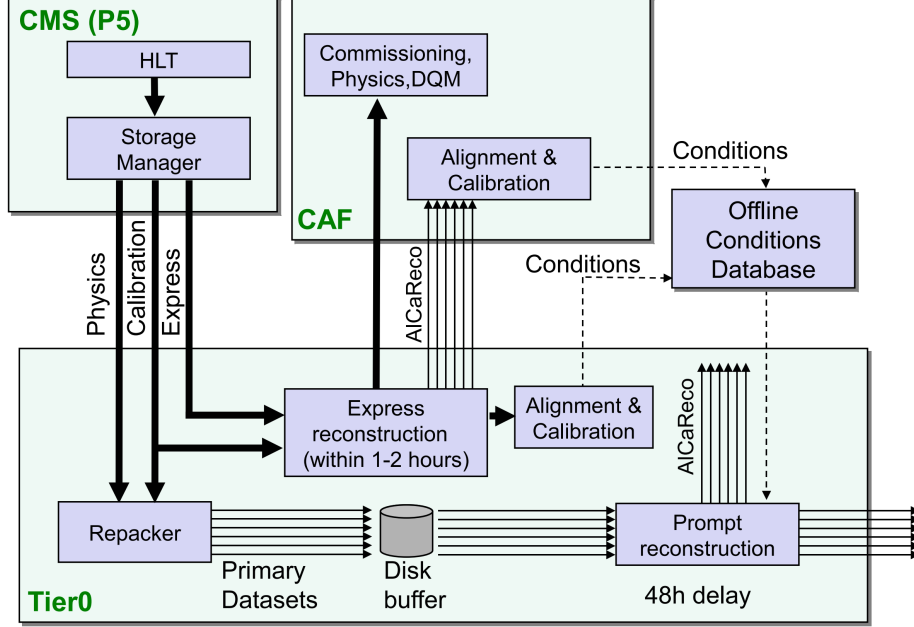


Figure 2.8: Schematic overview of Tier0 computing, data can be available from different sections allowing for data quality monitoring and also storage to several databases [14]

The data can then be stored at many different sites. The sites are demarcated based on

importance and functionality. There is one Tier-0, seven Tier-1, about one-hundred fifty Tier-2, and numerous Tier-3 centers. The sum of these tiers is the “grid” or the Worldwide LHC Computing Grid (WLCG), which in total combines 900 000 cpus from over 170 sites in 42 countries. **XrootD** and tools like **Rucio** are used for a global file lookup service that allows physicists from around the world to access and use centrally supported data. An abundance of information that is constantly changing can be found <https://home.cern/science/computing/grid>.

# Chapter 3

## Luminosity

Luminosity sets the scale for the number of events recorded at the LHC. It is how bright the beam is and correspondingly, dictates how many interactions can be expected over a data taking period. Therefore, it is important for all physics analyses to use the correct luminosity, and its measured error, to obtain an accurate result. The number of expected events for any given process is the luminosity  $\mathcal{L}$  times the cross section  $\sigma$ .

$$N_{\text{event}} = \mathcal{L}\sigma_{\text{event}} \quad (3.1)$$

$$\mathcal{L} = \frac{N_b^2 n_b f_{\text{LHC}} \gamma_r}{4\pi \epsilon_n \beta^*} \left( 1 / \sqrt{1 + (\frac{\theta_c \sigma_z}{2\sigma^*})^2} \right) \quad (3.2)$$

$N_b$  is the number of particles in the bunch crossing,  $n_b$  the number of bunches,  $f_{\text{LHC}}$  the revolution frequency of the LHC,  $\gamma_r$  the relativistic factor,  $\epsilon_n$  the normalized beam emittance,  $\beta^*$  the beta function at the collision point (related to the crossing angle),  $\theta_c$  is the full crossing angle,  $\sigma_z$  the RMS bunch length and  $\sigma^*$  the transverse RMS beam size at the interaction point.

Several subsystems are used to measure luminosity at CMS. Particularly the Pixel Luminosity Telescope, Hadronic Calorimeter (HF) with summed transverse energy(ET) and occupancy (OC), BCM1F, and Tracker based or Pixel based luminosity to name several. In this section, the tracker based luminosity will be the focus. The pixel system is integral in the reconstruction of events for physics analysis and in measuring the luminosity.

There was validation of the new pixel detector in early 2017, from the BPIX and FPIX upgrades mentioned in section 2.3.1. The Lumi-POG (Luminosity physics object group) commisioned luminosity measurement using the clusters from the new pixel detector in an automated workflow. We

measure the luminosity by counting pixel clusters in a low channel occupancy setting and scaling it by a visual cross section determined in a separate analysis. Using the relation in equation 3.3 the instantaneous luminosity can be obtained once the number of clusters and the visible cross section  $\sigma_{\text{cluster}}$  are measured.

$$\langle N_{\text{cluster}} \rangle \equiv \frac{\sigma_{\text{cluster}}}{f_{\text{LHC}}} \mathcal{L}_{\text{SBIL}} \quad (3.3)$$

Where  $f_{\text{LHC}}$  is the revolution frequency of the LHC, and  $\mathcal{L}_{\text{SBIL}}$  is the instantaneous luminosity of a single bunch crossing—the aggregate collection of protons that are in the beam typically 3564 total bunches during standard pp-collisions.  $\sigma_{\text{cluster}}$ , is the cross section that is measured in a separate analysis involving Van-de-Meer scans (beam dynamic scans), more details can be found here [15].

For the pixel luminosity, a two component correction is applied on the fly to correct for self-radiative effects on the pixel modules under particle fluence and for inefficiency. One detail that is important in estimating the luminosity from the pixel detector is ensuring that the data that is taken and analyzed has consistent performance. Several times in a year, the Lumi-POG and Beam Radiation Instrumentation Luminosity (BRIL) groups analyze the performance of each sub-detector used to measure luminosity and certify the data once the analysis is complete. In 2017 and 2018 data taking campaigns, the luminosity from the pixel detector is vetted by looking at relative module performance over the runs of data taking for the year. If the modules don't have consistent performance they are removed from the final result.

Even though up to half of the modules are vetoed after this procedure, there are plenty of statistics (lots of pixel clusters per event) to keep the statistical uncertainties low. This module veto decision was made by taking the total clusters in each module and scaling them so that the overall total clusters are 1. Then on a per module basis, the performance relative to the total clusters are compared. This helps the analyzer look at consistent performance and manage a list of passing modules to be used in a final luminosity measurement using the pixel detector.

For Run III data taking (Summer 2022 to Fall 2025), integration of the cluster counting procedure was made into the High Level Trigger at CMS. A data compression of  $10^3$  was made by taking the raw level data from the silicon pixels and storing them in a simple data container, saving a peta-byte of data. Online luminosity using these data containers and methods are being investigated as more CMS-physicists are interested in using the central tracking system for luminosity

measurements.

# Chapter 4

## Lepton Identification and Data

### 4.1 Lepton Identification

The following three sections briefly describe how certain subsystems of the CMS detector work together to identify muons, electrons, and tau leptons.

#### 4.1.1 Muon Identification Systems

In order to identify good muons, several subdetector work together to reconstruct muons. Looking at muons that come from the interaction vertex—prompt muons—the tracker plays an important role in identifying charged particle tracks.

As CMS implies in its name, muons are certainly a focal point in particle detection.

The tracker system works in tandem with the gas chambers to reconstruct muons, and the solenoid measures charge particle's momentum allowing for an accurate mass resolution.

During reconstruction, tracker or global muons are identified and are ultimately divided into four sub types depending on the  $\chi^2$  of the track and momentum of the candidate muon [16, 17]

#### 4.1.2 Electron Identification Systems

The main sub detector system that is involved with electron identification is the ECAL. To identify electrons a cluster of energy in the ECAL is associated with a track that is constructed in the silicon detector system.

The tracks are identified in the typical fashion by using the Kalman Filter tracking technique

to pick good quality tracks, then the tracks are refitted using a Gaussian Sum Filter (GSF). This track would then be associated with the ECAL super cluster (SC) by requiring matching in  $\eta$ ,  $\phi$  space

$$|\Delta\eta| = |\eta_{\text{SC}} - \eta_{\text{in}}^{\text{extrap}}| < 0.02 \quad (4.1)$$

$$|\Delta\phi| = |\phi_{\text{SC}} - \phi_{\text{in}}^{\text{extrap}}| < 0.15 \quad (4.2)$$

This association amounts to an overall efficiency of about 93% [18].

#### 4.1.3 Tau Identification Systems

Tau leptons are one of the most diverse particles in the Standard Model, decaying in many different ways. It is the heaviest lepton, so heavy that even tau decays to intermediate mesons are possible. The  $\rho$ ,  $a$ , and  $\pi$  mesons are several possible mesons that the tau can decay to. Therefore, when it comes to tau identification many subsystems are needed to properly identify them in addition to higher level algorithms. The focus of this section is on the hardware components that are needed to identify tau leptons. Tau leptons decay both hadronically and leptonically as shown in the table below 4.1.

Table 4.1: Possible hadronic tau decays,  $h$  doesn't indicate a Higgs particle but a hadronic prong [19]

Decay Modes	Resonance	$\mathcal{B}(\%)$
Leptonic Decay		35.2
$\tau^- \rightarrow e^- \bar{\nu}_e \nu_\tau$		17.8
$\tau^- \rightarrow \mu^- \bar{\nu}_\mu \nu_\tau$		17.4
Hadronic Decay		64.8
$\tau^- \rightarrow h^- \nu_\tau$		11.5
$\tau^- \rightarrow h^- \pi^0 \nu_\tau$	$\rho(770)$	25.9
$\tau^- \rightarrow h^- \pi^0 \pi^0 \nu_\tau$	$a_1(1260)$	9.5
$\tau^- \rightarrow h^- h^+ h^- \nu_\tau$	$a_1(1260)$	9.8
$\tau^- \rightarrow h^- h^+ h^- \pi^0 \nu_\tau$		4.8
Other		3.3

The Hadron Plus Strips (HPS) combines the use of the tracker system and the electromagnetic calorimeter (ECAL) for hadronic tau identification [20].

## 4.2 Data and Simulation Used for Analysis

Data gathered at CMS is organized primarily on the trigger implemented to identify events. For this analysis, requiring muons is paramount and the search should be inclusive. Therefore datasets published by CMS that are considered are single muon, double muon, and electron plus photon datasets depending on the year. These datasets contain the triggers that are the most important for event selection. Single muon triggers that contain isolated muons at 24 and 27 GeV thresholds are implemented, along with double muon triggers with good reconstructed muons that have 17 GeV threshold. More information on triggers and selection will be given in the event selection section.

The simulation used to compare to data typically use MadGraph5@NLO along with a PYTHIA 8 hadronizer. These CMS-centrally generated samples are then digitized to the same format as real data events collected and processed at CMS high level trigger. These raw data formats are then reconstructed to physics objects - like tracks and higher level objects like muons and  $\tau$  leptons. A direct comparison between data and simulation can then be made after calibrating simulation in control regions.

Data taken from CMS during the entire Run II period was examined. This corresponds to 137  $\text{fb}^{-1}$  of integrated luminosity. The list for data and simulation Monte Carlo(MC) is exhaustive and listed in the appendix A.

For the MC production of the signal samples, to reflect the 2HDM modeling, events were generated at tree level for a pseudoscalar Higgs like boson between the masses of 15 and 60 in intervals of 5 GeV with gluon fusion production. These masses are sufficient for the parametric modeling described in the fit to obtain a more precise peak resolution. The signal samples were privately produced for 2017 and 2018, because CMS MC generator contacts weren't sufficient in providing the samples in an acceptable manner. Samples existed from the 2016 analysis. MadGraph5@NLO v2.6.5 was used to generate these events with a PYTHIA 8 hadronizer. Privately produced samples were used for 2017 and 2018. However, the scripts and conditions used are located here: <https://github.com/samhiggle/iDM-analysis-AODproducer/tree/haa>. The NMSSMHE $t$  model was used to simulate the events. Parameters and information can be seen in the package: <https://cms-project-generators.web.cern.ch/cms-project-generators/>.

### 4.2.1 $2\mu 2\tau$ Signal Samples

For the Monte Carlo production of the signal samples, to reflect the 2HDM modeling, events were generated at tree level for a pseudoscalar Higgs like boson between the masses of 15 and 60 in intervals of 5 GeV with gluon fusion production. These masses are sufficient for the parametric modeling described in the fit to obtain a more precise peak resolution. MadGraph5@NLO v2.6.5 was used to generate these events with a PYTHIA 8 hadronizer. Privately produced samples were used for 2017 and 2018. However, the scripts and conditions used are located here: <https://github.com/samhiggi/eIDM-analysis-AODproducer/tree/haa>. The NMSSMHEt model was used to simulate the events. Parameters and information can be seen in the package: <https://cms-project-generators.web.cern.ch/cms-project-generators/>.

## 4.3 Corrections to Simulations

For accurate results that reflect true experimental data, many corrections to MC samples are made. In general, in compliance with CMS’s Physics Object Groups (POGs), standard techniques are applied to ensure proper simulation. Of critical importance is the corrections to energy scales for the leptons in the analysis. These corrections will affect the nominal energy recorded for the event as well as the rates in which objects are identified. In order to protect against bias and to investigate systematic errors, corrections that could effect the results are considered in the overall error in the statistical inference model.

### 4.3.1 Muon energy scale

Corrections to the muon’s energy scale are computed for the muons that pass selection for the analysis. Medium muon ID with track based isolation that pass the isolated single muon triggers at 24 GeV and 27GeV are then rescaled for pileup, efficiency, di-lepton  $P_T$  and EWK re-weighting of based on accurate gauge boson measurements. After selection, the scale factors for energy corrections are measured and parametrized in  $\phi$  and  $\eta$  in multiplicative and additive corrections

$$\rho^{\text{cor}} = \kappa(\eta, \phi)\rho + Q\lambda(\eta, \phi) \quad (4.3)$$

In practice these are just scale factors applied to the energy scale in certain eta phi regions.

Table 4.2: Measured energy scale correction for genuine across all years.

Correction (%)	
$\eta$ region	scale factor
0 – 1.2	0.4
1.2 – 2.1	0.9
> 2.1	2.7

### 4.3.2 Electron energy scale

Genuine electron energy scale and resolution requires corrections to be applied to MC in order to match data [21]. These corrections are provided directly by the E/Gamma POG, and applied to genuine electrons coming from tau lepton decays for the channels  $\mu\mu e\mu$  and  $\mu\mu e\tau$ .

The energy shift is split depending on the  $\eta$  of the electron shown in table 4.3.

Table 4.3: Measured energy scale correction for genuine across all years.

Correction (%)	
$\eta$ region	scale factor
0 – 1.2	1.0
1.2 – 2.1	1.0
> 2.1	2.0

### 4.3.3 $\tau$ energy scale

There is a central energy shift based on the type of tau decay. Due to the electroweak interactions  $\tau$  leptons decay hadronically and leptonically. Figure 4.1 shows the typical tau decay leptonically or hadronically.

When the tau decays hadronically, many different intermediate mesons are produced and each type of decay has different kinds of signatures particularly when they hadronize and deposit the energy within the hadronic calorimeter of CMS. The Tau-POG has measured the central value

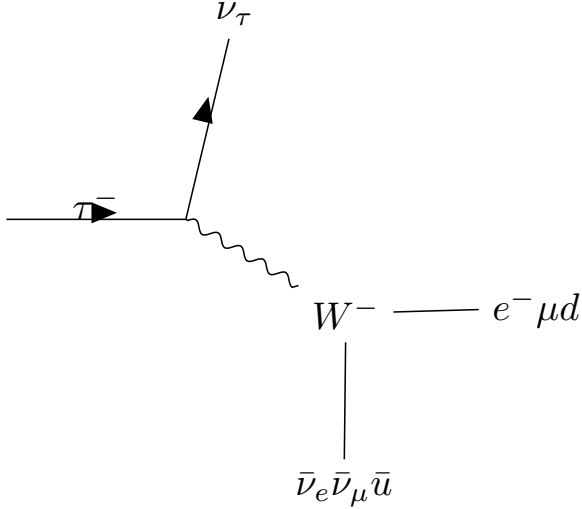


Figure 4.1: diagram depicting the possible decays of the tau lepton: 65% of the time hadronically and 18% to tau neutrino and electron with antielectron neutrino (17% for muon)

systematic deviation as a form of scalar factor that should be applied for an accurate result of measuring the tau's energy. This is split by the prongs (charged hadrons) and  $\pi^0$ 's.

Table 4.4: Measured  $\tau_h$  energy scale correction for genuine  $\tau_h$ 's across all years.

Decay mode	Correction (%)		
	2016	2017	2018
$h^\pm$	-0.6	0.7	-1.3
$h^\pm \pi^0$	-0.5	-0.2	-0.5
$h^\pm h^\pm h^\pm$	0.0	0.1	-1.2

The deviation in the model is measured by between the difference in data and MC for different values of hadronic tau energy. The uncertainty is measured for each decay mode considered in the analysis. Figures 4.2 shows the differences in data and MC for the 1 prong +  $\pi_0$  decay mode as a function of tau energy, all other tau decay modes are also measured.

#### 4.3.4 $\tau_h$ ID efficiency

Genuine  $\tau_h$  identification efficiency can be different in Data and MC [22]. To correct for this difference, measurements are made in an inclusive  $\mu\tau$  channel, using genuine Drell-Yan to  $\tau_h$  as a signal and using the invariant mass of the  $\tau_h$  as an observable. Naturally, this region has far more statistics than the control and signal regions in the pseudoscalar analysis. To measure the

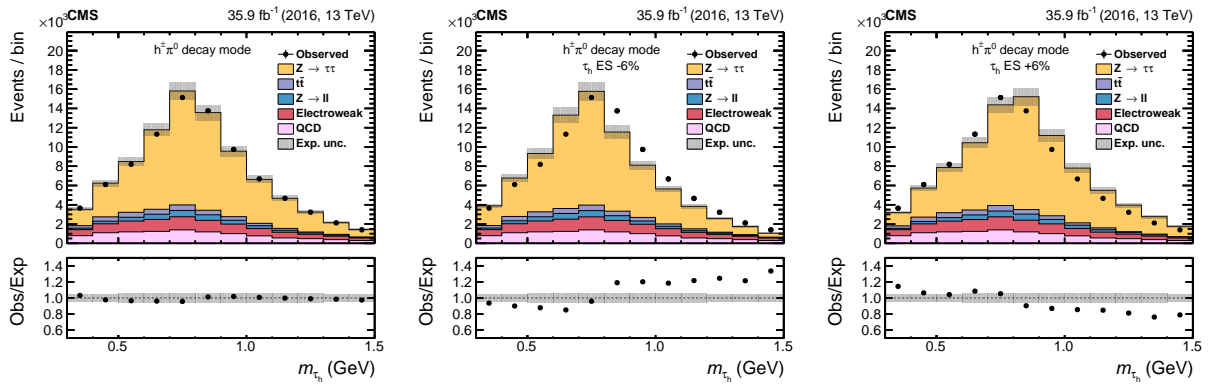


Figure 4.2: Tau mass distributions considering the nominal  $\tau_h$  energy scale in simulation (left), or the  $\tau_h$  energy scale shifted by -6% (left) or +6% (right), in the  $\mu\tau_h$  final state, for the 1 prong + pizero decay mode.

identification efficiency precisely, it is done in the inclusive regions with an emphasis of simulation containing real taus. This measurement is done by the Tau POG, and the scale factors are provided to CMS.

For the  $\mu\mu e\tau_h$  and  $\mu\mu\mu\tau_h$  channels, scale factors are binned in 3 different  $p_T$  bins: 30–35, 35–40, and 40+ GeV. In the  $\tau_h\tau_h$  final state, the efficiencies are also binned by decay mode.

These efficiencies, while used in the primary event and the parameter of interest in the fit, they are not considered in the systematic model as they are expected to have very little impact on fit and limits based on the 2016 result.

#### 4.3.5 $e \rightarrow \tau_h$ and $\mu \rightarrow \tau_h$ misidentification rate

The efficiencies associated with  $\tau$  identification through the Deep Neural Net approach is considered. The efficiency of the discriminators against electrons or muons misidentified as  $\tau_h$  candidates can be miss-modeled in simulation. These data/MC scale factors are binned by barrel/endcap region of the measured  $\eta_{\tau_h}$ , and by  $\tau_h$  decay mode. They depend on the anti-electron or anti-muon discriminator used. Scale factors are measured to correct this and are applied to  $e \rightarrow \tau_h$  or  $\mu \rightarrow \tau_h$  in MC. Full information on misidentification measurements and application in analyses can be found in reference [22].

The misidentification scale factors are derived by pass and fail regions. The regions are set up by selecting events where a reconstructed  $\tau_h$  passes the DNN working point and also fails the

DNN discriminant against muons. QCD multijet is estimated from same sign lepton region within data - similar to the fake rate calculation like in chapter 6. W+Jets normalization is carefully selection from a region with high transverse mass. The visible mass distributions of the events in these regions are fit and the overall signal yield remains constant in the pass and fail regions. The normalization of  $Z \rightarrow ee$  background is allowed to vary in this muon faking tau measurement. The expected impact on the systematic model from these anti-lepton discriminators are expected to be very small so they are not included in the uncertainty model.

#### 4.3.6 Pileup Re-weighting

MC events are re-weighted using a minimum bias cross section equal to the luminosity for the corresponding year. This pileup re-weighting is to rescale the events for effective number of primary interactions during collisions. During Run II, pileup or the number of primary vertices in a crossing or underlying event could reach close to 100 and in Run III this will exceed 200.

#### 4.3.7 Electron and muon identification efficiency

Scale factors derived within the HTT group are applied for muons [23], and the EGamma POG scale factors are applied for electrons [24]. The scale factors for muons with  $5 < p_T < 9$  GeV and  $9 < p_T < 10$  GeV, are computed privately as there are no official numbers, and were approved by the MuonPOG in the 2016 analysis.

#### 4.3.8 Generator event weights and luminosity

Generator weights are applied on an event-by-event basis. Samples produced with the aMCatNLO generator contain both positive and negative event weights. The presence of negative event weights reduces the effective statistics of the samples. The event weights for simulation are scaled to the expected yields for each sample. The number of generated events in each sample is used, however in the aMCatNLO sample this sum of generated events is weighted by the generator weights, effectively making the aMCatNLO samples smaller when weighting for luminosity and cross section. Additionally, K-factors are considered for W+Jets and Drell-Yan samples in order to correct between purely generated events and reconstructed event yeilds for Drell-Yan a factor of

1.1637 is used and for W+Jets a factor of 1.221 is used. These are applied to each exclusive and inclusive samples during the combination of inclusive and exclusive sample processing.

#### 4.3.9 Offline Muon Selection

Due to the selection of muons at 5 GeV, which is below the trigger threshold, scale factors were measured in the barrel and endcap using the tag and probe technique in the 2016 analysis. These factors are considered, in addition to the Muon POG's recommendation, to support correct simulation of data.

Table 4.5: Scale factors to correct for Offline muon selection being less than the online trigger threshold.

	Barrel	Endcap
Muons with $5 < pT < 9$ GeV	0.956	0.930
Muons with $9 < pT < 10$ GeV	0.916	0.897

#### 4.3.10 Visualizing the Corrections

The energy scales for the various leptons used in the analysis are not only changed in the nominal case, but their uncertainty is measured and then propagated to the fit model via changes in the normalization for the distribution. To visualize this and provide a cross check distributions for the  $\tau$ ,  $\mu$ , and  $e$  energy scales are cross checked in the parameter of interest (the mass of the di-muon system from the leading  $p_T$  pseudoscalar  $a$  particle). These systematics for  $\mu\mu\tau\tau$  channel are visualized here in figure 4.3.

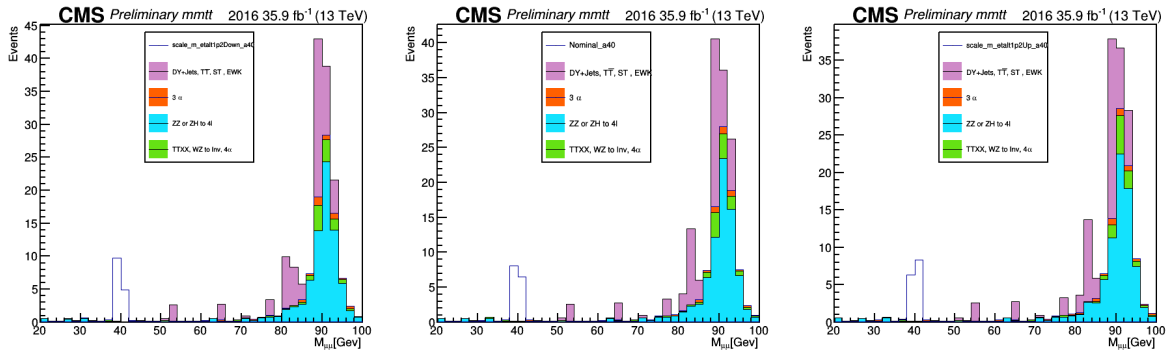


Figure 4.3: Systematic Shift in the Uncertainty Model for 2016  $\mu\mu\tau\tau$  for the muon energy scale shift down (left), nominal (mid), and up (right), no data is shown on this plot as it directly reflects the signal region without the extraction cuts

In the end, the uncertainty considered in the fit model would then be the percent yield up and down as a log-normal that affects the normalization of the template. Because the model is so statistically limited the log-normal is sufficient in capturing the changes in the distributions over the fit range.

# Chapter 5

## Event Selection

### 5.1 Framing an Analysis at CERN

In order to make a definitive statement and concrete hypothesis test, two perspectives are taken. There is the null hypothesis, ergo the hypothesis of the accepted standard within High Energy Physics—the Standard Model—which will comprise all possible events that are categorized as *background*.

Then the alternative hypothesis is taken to be the model that encompasses the Standard Model and adds additional physics that will contain events from the theory under consideration in the analysis *signal*. For this analysis, it's events pertaining to the pseudoscalar Higgs-like particle “a”, with two muons and two tau leptons in the final state.

### 5.2 Defining Signal and Control Regions

The next thing to consider is what data should be used to test that hypothesis. Working with CMS, central Standard Model simulation samples are provided. Then to make the analysis competitive, regions of the full data and simulation are cut away in order to increase the number of signal events relative to background events. This process is known as “making cuts”. In order to not bias the result, typically regions are setup to investigate the agreement of simulation with data (the control region) and to conduct the statistical hypothesis test (signal region). When the data and MC simulation agreement are reasonable in the control region then the statistical test can be made in

the signal region.

### 5.2.1 Optimizing Lepton Pair Selection

In order to maximize the signal event yield - as it is expected that the analysis is statistically limited - a simple selection algorithm was used to identify good lepton pairs that come from the pseudo scalar  $a$ . Standard working point cuts are made, in addition to delta R cleaning, two prompt-like muons with opposite charge and leading scalar summed  $P_t$  are chosen to form the first decay products of the  $a$  and two opposite charged leading scalar summed  $P_t \tau$  leptons are chosen for the second  $a$ . This approach increased the signal acceptance compared to choosing mass window cuts to form the  $a$  pairs. The following table reflects the pair matching efficiency study done with the preliminary dataset from 2016 NanoAODv6:

Table 5.1: Lepton Pair Matching Efficiency

$a$ - Mass	15	20	25	30	35	40	45	50	55	60
Efficiency	0.87	0.82	0.79	0.79	0.79	0.80	0.80	0.83	0.85	0.87

All selections follow the Physics Object Group (POG) recommendations for object selection. Since the search in 2016, a new identifier for  $\tau$  leptons was considered using a Deep Neural Network (DNN) [25]. To identify the dimuon pair which come from one pseudoscalar  $a$ , several cuts were applied across all channels:

- each  $\mu_{pt} > 5.0$  GeV,
- charge dimuon  $< 0$
- all  $\mu_{iso} <= 0.2$
- medium ID of the  $\mu$ , require global and track requirements (good  $\mu$ )
- number of b-quark tag jets  $< 1$
- signal extraction cuts (not shown in data MC control plots)
  - invariant mass of the 4 lepton system (AMass) $< 120GeV$
  - $M_{\mu\mu} > M_{\tau\tau}$

The trigger requirements are inclusive, selecting events that pass single muon and double muon triggers. Events that are triggered by the single muon triggers criteria contain muons that are isolated with either 22, 24, and 27 GeV muons. Double muon triggers have a 17 GeV threshold for the leading muon and 8 GeV for the subleading muon. Triple muon triggers are used for the channels that have three muons in the final state and have a descending threshold of 12, 10, and 5 GeV. These triggers and other minimal selection requirements are listed in table 5.2.

Table 5.2: Event selection requirements for the four decay channels. These demarcate cuts that are applied to the  $p_T$ ,  $\eta$ , and isolation of the particle in addition to the trigger requirements.

Channel	Trigger requirement	Minimal lepton selection		
		$p_T$ (GeV)	$\eta$	Isolation
$\mu\mu\tau_h\tau_h$	$\mu[22] \mu[24] \mu[27]$ or $\mu\mu[17, 8]$	all $p_T^\mu > 5$ $p_T^{\tau_h} > 18.5$	$ \eta^{\tau_h}  < 2.3$	Med. DNN $\tau_h$
$\mu\mu\mu\tau_h$	$\mu[22] \mu[24] \mu[27]$ or $\mu\mu[17, 8]$ or $\mu\mu\mu[12, 10, 5]$	all $p_T^\mu > 5$ $p_T^{\tau_h} > 18.5$	$ \eta^\mu  < 2.3$	$I^\mu < 0.2$
$\mu\mu e\tau_h$	$\mu[22] \mu[24] \mu[27]$ or $\mu\mu[17, 8]$	all $p_T^\mu > 5$ $p_T^e > 7$ $p_T^{\tau_h} > 18.5$	$ \eta^e  < 2.5$	$I^e < 0.15$
$\mu\mu e\mu$	$\mu[22] \mu[24] \mu[27]$ or $\mu\mu[17, 8]$ or $\mu\mu\mu[12, 10, 5]$	all $p_T^\mu > 5$ $p_T^e > 7$ $p_T^\mu > 5$	$ \eta^e  < 2.4$	Med. DNN $\tau_h$

As mentioned in the instrumentation and detector section, the muon identification system uses the tracker to identify charged tracks and the muon chambers identify the particles later in their trajectory after they exit the solenoid. Typically “good” muons are those that are both associated with a track and their subsequent identification in the drift tubes or the CSC chambers. The average muon lifetime is 2.2  $\mu$ s so they travel quite far from the interaction point the sub detectors. The physics object group’s recommendations are followed, which select muons with  $p_T > 15$  GeV and  $|\eta| < 2.4$  in addition to selecting only “good” muons.

Electrons originating from the tau decay are reconstructed in by track association in tandem with energy deposition in the Electronic Calorimeter (ECAL). To clarify selection in the calorimeter systems, events are vetoed for candidate electrons that also show a substantial energy deposition in the HCAL. The hits and track quality from two separate algorithms, along with the geometrical and energy matching from the ECAL are used in a Multivariate Analysis (MVA) technique like Boosted Decision Trees (BDTs) to select good electrons for analysis [18].

Of critical importance in event selection is identification of unique particles, particularly differentiating between lepton candidates that come from the interaction vertex (prompt) and those that appear from decays down the line (nonprompt). Relative isolation is typically defined in order to

ensure there is no overlap between candidate leptons. More details on this variable and it's usage in the Particle Flow algorithm can be found here [26].

$$I^\ell \equiv \frac{\sum_{\text{charged}} p_T + \max(0, \sum_{\text{neutral}} p_T - \frac{1}{2} \sum_{\text{charged}}, \text{PU } p_T)}{p_T^\ell}. \quad (5.1)$$

$\sum_{\text{charged}} p_T$  is the scalar sum of the transverse momenta of the charged particles originating from the primary vertex and contained in a cone of size  $\Delta R = \sqrt{(\Delta\eta)^2 + (\Delta\phi)^2} = 0.4$  (0.3) centered on the muon (electron) direction. The sum  $\sum_{\text{neutral}} p_T$  is a similar quantity for neutral particles.

To identify  $\tau_h$  candidates, the hadron-plus-strips (HPS) algorithm is used to identify the major modes of the hadronic tau decay [20]. Typically events with hadronic prong are considered in combination with a number of neutral pions and missing transverse energy from the neutrinos. Pions almost always decay to photons, so an algorithm is considered that joins the identification of charged hadrons and neutral pions. The HPS algorithm combines inner track information, hits in the HCAL, and pion association in the ECAL by deposits in a  $\eta, \phi$  strip region to identify hadronic tau leptons. The  $\tau_h$  is matched to  $h^\pm, h^\pm\pi^0, h^\pm h^\mp h^\pm$ , or  $h^\pm h^\mp h^\pm\pi^0$  depending on the overall charge vs neutral constituents [27]. In addition to HPS algorithms, a Deep Neural Network (DNN) was constructed to further aid in identification by discriminate between genuine tau leptons and those that originate from quark or gluon jets, electrons, or muons. In the DNN, the tau four-momentum and charge, the number of charged and neutral particles used to reconstruct the tau candidate, the isolation variables, the compatibility of the leading tau track with coming from the primary vertex, the properties of a secondary vertex in case of a multiprong tau decay, observables related to the  $\eta$  and  $\phi$  distributions of energy reconstructed in the ECAL strips, observables related to the compatibility of the tau candidate with being an electron, and the estimated pileup density in the event are all used. In total, 47 high-level input variables are incorporated [28]. In practice, the DNN has discriminators for muons, electrons, and jets that fake genuine taus and have efficiencies that go from 40% to 90% in a 10% granularity of the discriminating variable. The medium working point is used for each of these discriminators.

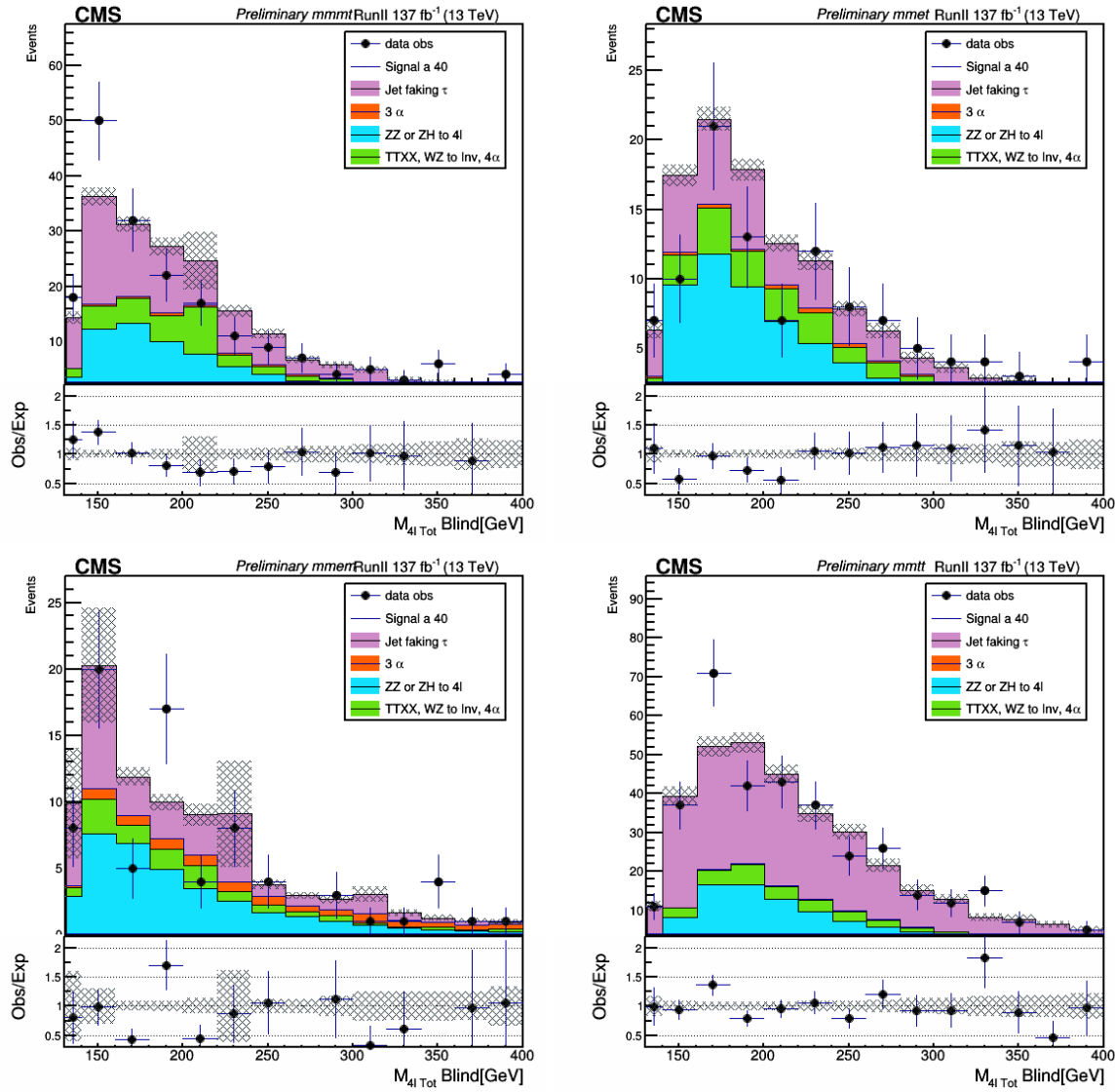


Figure 5.1: Invariant mass of the four lepton system for 2018 data in all Channels

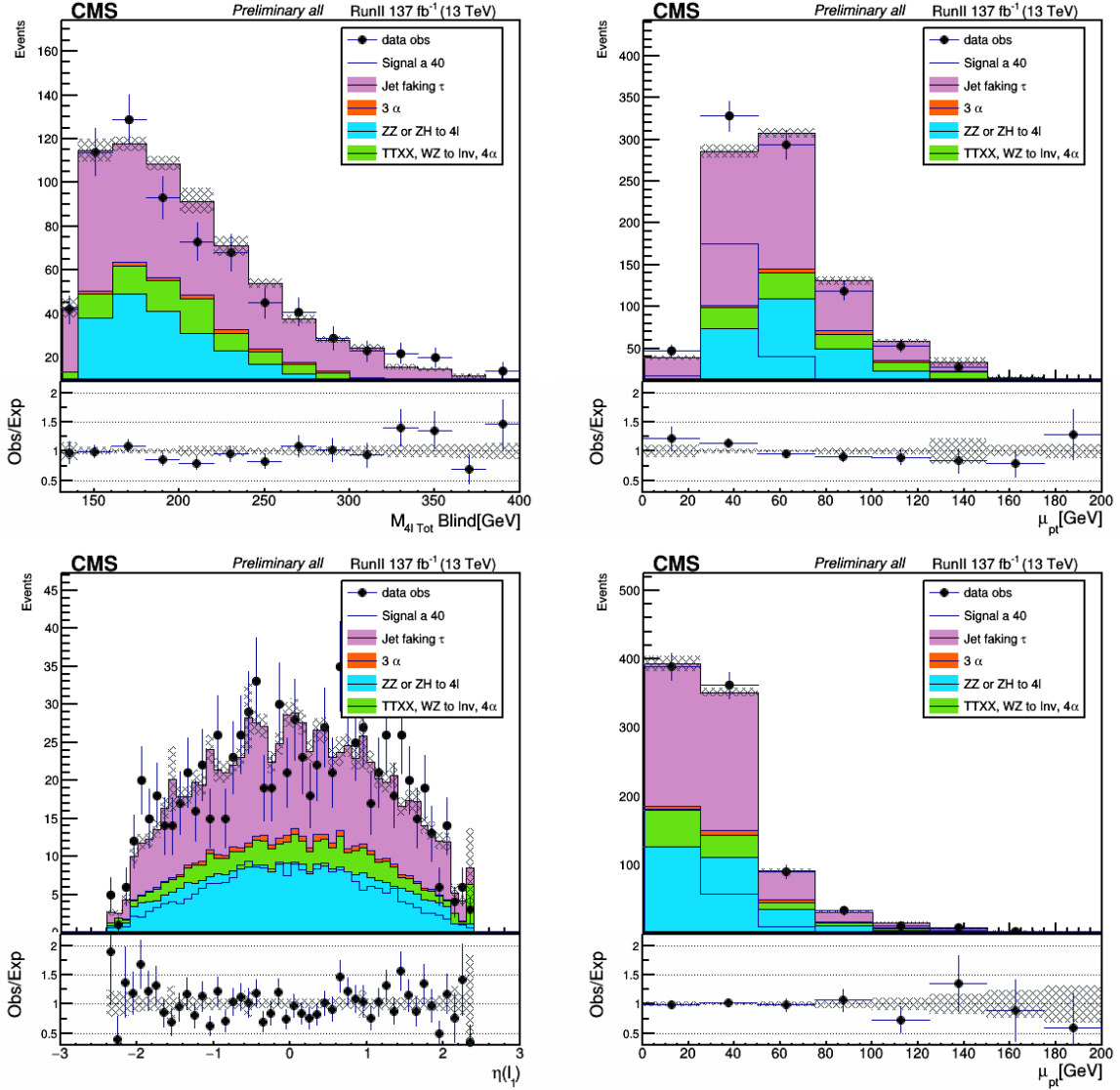


Figure 5.2: Several data-MC control plots for full RunII data in all Channels

# Chapter 6

## Background Estimation

In addition to the Monte Carlo simulation, a data driven method is used to estimate a significant portion of background that simulation alone is not sufficient to measure. Tau leptons decay hadronically about 65% of the time forming intermediate mesons. The clusters of hadrons that these decays produce are very similar to Quantum Chromodynamic (QCD) processes. These QCD events effectively fake the hadronic  $\tau$  signature for the  $a$  decay.

In order to conduct the data driven method, a proportionality is made to extract the jet faking tau background. Generally, this proportion is constructed using an orthogonal region to the statistical hypothesis test (the test is conducted in the signal region). For example this could be sign inversion on the lepton pair used in the final state. In this orthogonal region and in the signal region, tight and loose identification criteria is made to extrapolate the scale factor. One of the critical assumptions for this method to hold is that the shape of the distribution doesn't change much by the tight to loose regions. Therefore using the orthogonal regions—tight and loose—along with the loose signal region one can extrapolate the number of events in the tight signal region. Due to the four regions, the method is also referred to as the “ABCD” method.

### 6.0.1 Brief Outline of the Fake Rate Method

The general outline to measure the fake rate is as follows. The fake rate function in the same sign (SS) region is *known*. Events passing loose identification in the opposite sign (OS) region is *known*. Events passing in the signal region is *unknown*. Assuming the shapes are similar and that the loose and tight identification is not dependent on the sign of the leptons. Then one can make

the equivalence statement:

$$\frac{\text{Events}_{\text{SS Tight}}}{\text{Events}_{\text{SS Loose}}} \equiv \frac{\text{Events}_{\text{OS Tight}}}{\text{Events}_{\text{OS Loose}}} \quad (6.1)$$

To make the expression more precise, the fake rate function is typically parametrized in lepton candidate transverse momentum. Also, prompt MC is subtracted from data, which is motivated by estimating the true jet faking taus background (non-prompt taus). If MC is matched to prompt then it is unlikely a jet faking tau, so they are removed.

$$f_r(pt) = \frac{\text{Data Events S.S. Tight} - \text{Prompt MC Background}}{\text{Data Events S.S. Loose} - \text{Prompt MC Background}} \quad (6.2)$$

After the measurement is made for each leg, then apply the fake rate as an event weight to the Opposite Sign loose region one leg at a time to extrapolate to the signal region. So isolating the events in the signal region and flipping the relation in equation 6.1, one obtains the result for each lepton candidate in the final state:

$$\text{Events}_{\text{OS Tight}} = f_r(pt) \cdot \text{Events}_{\text{OS Loose}} \quad (6.3)$$

### 6.0.2 Measurement of the Fake Rate

To measure the fake rate multiple categories are considered. As outlined in the standard model Higgs decays to tau leptons analysis and its supporting document on fake rate measurements, several regions are used to determine the fake rate [23]. The separate “enriched” background regions are considered

- QCD multijet (large majority of jet $\rightarrow \tau_h$  fake events in the  $\tau_h \tau_h$  final state)
- W+jets (mostly in the e $\tau_h$  and  $\mu\tau_h$  final states)
- tt events with fully-hadronic or semi-leptonic decays
- diboson events with fully-hadronic or semi-leptonic decays.

These are then measured as a function of  $p_T$  of the object and split into subcategories depending on the decay mode.

In the QCD multijet region, there is no way to estimate it with pure MC simulation. Therefore, in order to estimate the QCD contribution all MC simulation events are subtracted before the

measurements. Then the remaining fake rate measurement in the determination region is assumed to be from QCD.

In the W+Jets region, similarly all MC is subtracted except for the W+Jets simulation. Note that QCD contamination is minimal because of the dominance of the W boson resonance.

In the  $t\bar{t}$  region it is the same as the W+Jets regions, except the subtraction is  $t\bar{t}$ ; however, there is also an isolation region that is used because the fake rate for this process is expected to be very small and actually calculable using MC, so in addition to the genuine  $t\bar{t}$  events, the fraction of jets faking hadronic taus are also included in the subtraction.

To parameterize the fake rates as a smooth function in  $p_T$ , a line is fitted to each distribution. In addition to measuring the rate for each “enriched” background region, they are further split by final state or lepton candidate composition.

W+jets with no jets and one jet, QCD multi-jet with no jets, one jet, and more jets, and  $t\bar{t}$  make up the total number of background categories that are measured. Only plots pertaining to the  $\mu\mu\tau$  and  $\mu\mu\mu\tau$  channels are created.

At high hadronic tau  $p_T$  (greater than 100 GeV), negative fake rates are possible because of low statistics and the linear fit model extrapolation, so if the candidate tau has a  $p_T$  of greater than 100 GeV then the rate at 100 GeV is applied.

Fake factor measurements for the  $\mu\mu\mu\tau$  channel in the QCD 0jet region for 2017 is included in figure 6.1.

The rest of the regions are included in the Appendix B.

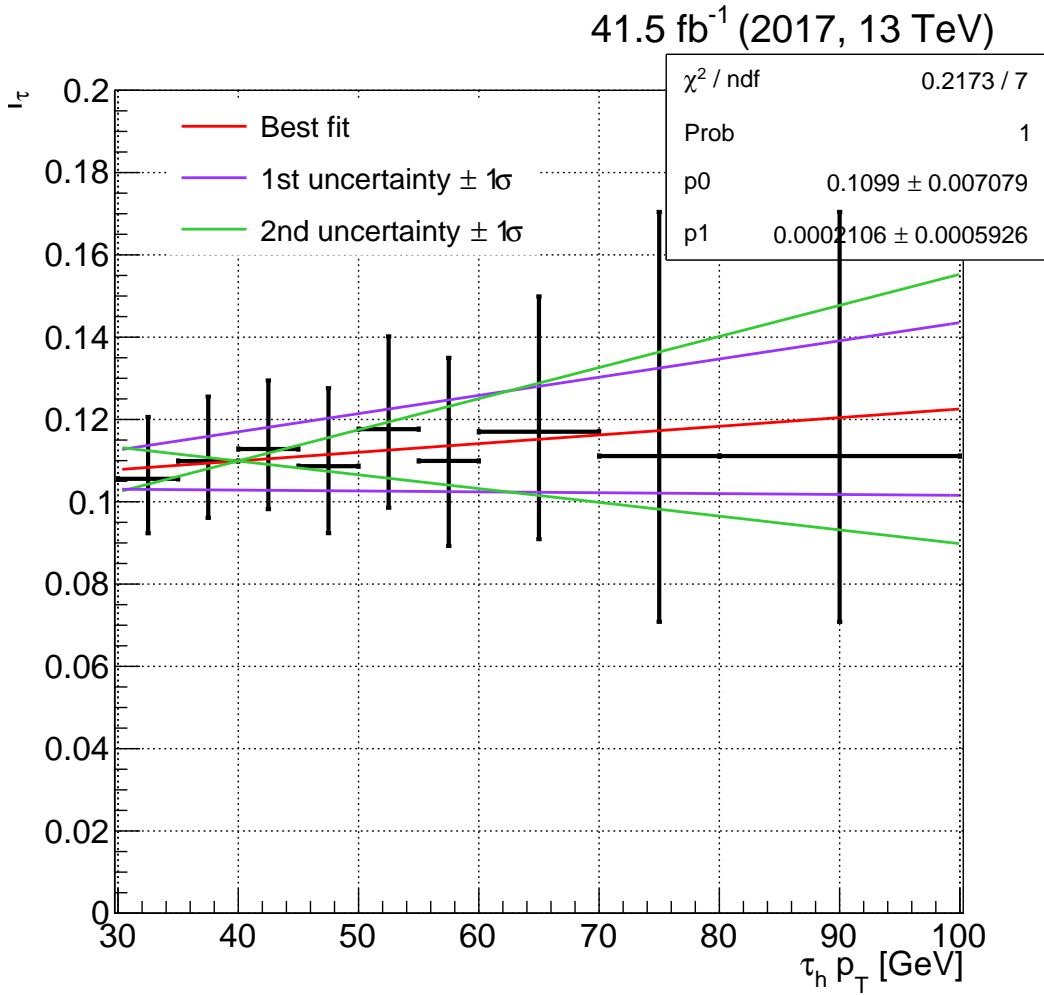


Figure 6.1: Fake factors determined in the QCD multijet determination region with 0 jet in the  $\tau_h$  final state in 2017. They are fitted with linear functions as a function of the  $\tau_h$   $p_T$ . The green and purple lines indicate the shape systematics obtained by uncorrelating the uncertainties in the two fit parameters returned by the fit.

### 6.0.3 Application of the Fake Rate Method

After the jet faking tau rate is measured, it is then applied to events that are identified as loose. Since the final state involves two tau leptons, this procedure is applied to each tau lepton in the final state thus requiring application of the fake rate to four different possibilities. Each lepton “leg” may be identify as loose or equivalently, failing the tight identification. The fake rate is then applied depending on the identification for each leg and in the case the event fails both legs then a minus sign is included to avoid the case of double counting.

- The final weight is then applied depending on the pass and fail criteria of each lepton candidate
- If event fails identification for leg 1:

$$f_1(pt) = \frac{f_{r_1}(pt)}{1 - f_{r_1}(pt)} \quad (6.4)$$

- If event fails identification for leg 2:

$$f_2(pt) = \frac{f_{r_2}(pt)}{1 - f_{r_2}(pt)} \quad (6.5)$$

- If event fails identification for both:

$$f_{12}(pt) = -\frac{f_{r_1}(pt)}{1 - f_{r_1}(pt)} \cdot \frac{f_{r_2}(pt)}{1 - f_{r_2}(pt)} \quad (6.6)$$

To illustrate the different regions please consider the diagram outlining the different regions in the “ABCD” method 6.2.

This fake factor methodology has been used by other analyses such as the standard model Higgs measurement with an associated Z boson [29].

For a closure test, the same criteria are applied to the selection of the tight same sign region. The vast majority of the background should be jets faking taus in that case. Indeed it is shown in figure 6.3.

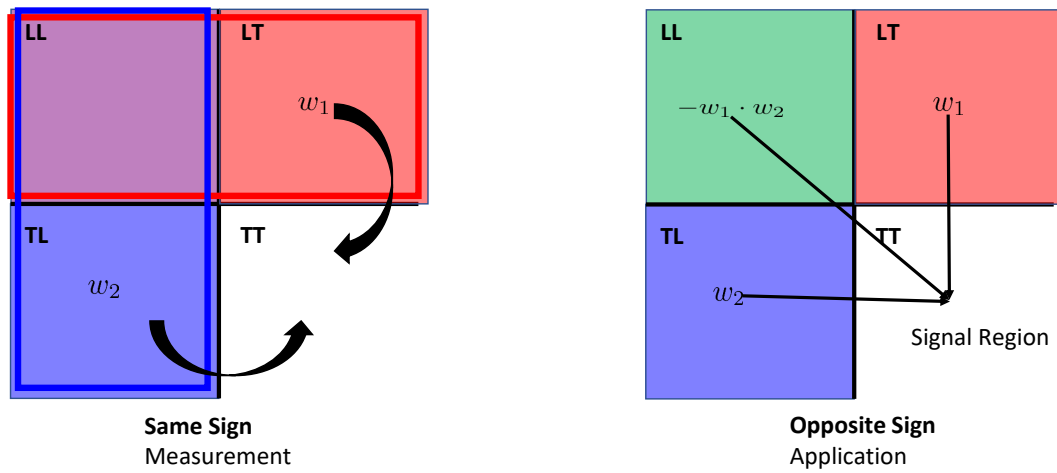


Figure 6.2: Diagram depicting the measurement and application regions, this “ABCD” method is multiplied by each of the  $\tau$  leptons in the final state

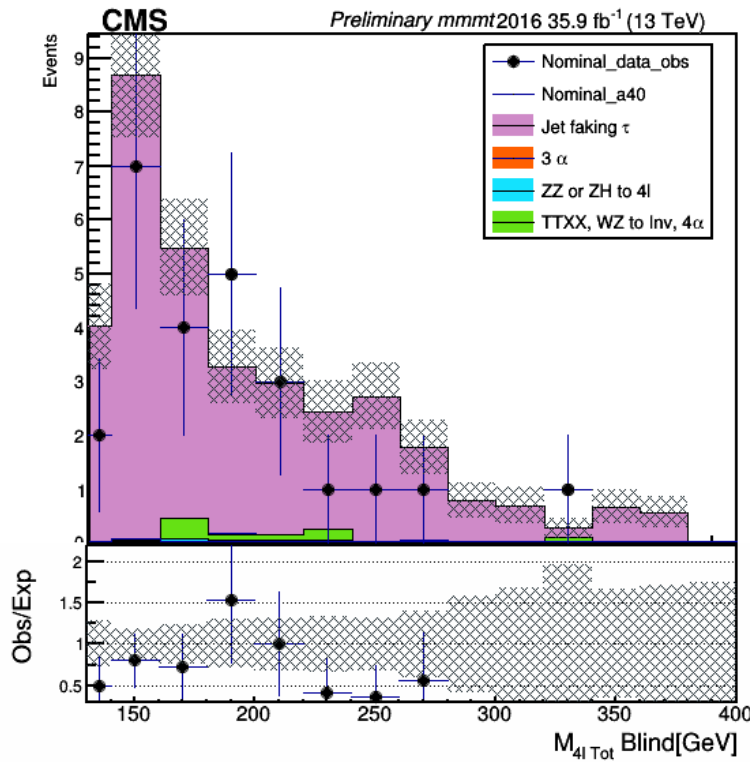


Figure 6.3: Validation of the fake factor method, fake factors are applied to the same sign tight region

# Chapter 7

## Statistical Inference Modeling

### 7.1 Statistical Inference at CERN

In order to conduct a hypothesis test, a test statistic is needed. This is constructed through the *profile likelihood ratio* and then a confidence level is set using the test statistic [30]. So construction of a likelihood is required, the test statistic from the likelihood, and a way to calculate a confidence level to complete the hypothesis test. To construct the likelihood, the typical approach is to assume a Poisson distribution for the events in the  $i^{th}$  bin and then “smear” it by multiplying it with a Gaussian that is also dependent on the events. The events are split, into signal and background. Because an alternative hypothesis is explored and a-priori the amount of signal events isn’t known, it is floated by a coefficient denoted as  $\mu$  - the signal strength. For an upper limit this value is changed until the cumulative distribution function of the likelihood reaches the desired confidence or  $p$ -value.

$$\mathcal{L}(\text{data}|\mu, \theta) = \text{Poisson}(\text{data}, \mu \cdot s(\theta) + b(\theta)) \cdot p(\tilde{\theta}|\theta) \quad (7.1)$$

For binned  $n_i$  events in bin label  $i$ :

$$\text{Poisson}(\text{data}, \mu \cdot s(\theta) + b(\theta)) = \prod_i \frac{(\mu s_i + b_i)^{n_i}}{n_i!} e^{-\mu s_i - b_i} \quad (7.2)$$

In the case of the pseudoscalar analysis discussed in this paper a slightly different likelihood is considered. A shape-based approach is considered, which instead of a product of many simple Poisson probability density functions, probability distribution functions are used over the entirety

of the fit variable (or parameter of interest POI). Multiple PDFs can be combined in this scenario, but the important difference is the absence of any binning. Therefore a good fit is required to have a good description of the events.

Unbinned or Parametric likelihood functions over  $k$  events,  $S$  and  $B$  the total event rate,  $f_s(x_i)$  and  $f_b(x_i)$  the *pdfs*

$$\text{Poisson}(\text{data}, \mu \cdot s(\theta) + b(\theta)) = k^{-1} \prod_i (\mu S f_s(x_i) + B f_b(x_i)) e^{-\mu S - B} \quad (7.3)$$

Specifically for the pseudoscalar analysis, a product of Bernstein polynomials for  $f_b(x_i)$  and Voigtian functions for  $f_s(x_i)$  are used. The Bernstein captures the slow changing background that is basically constant in a 2GeV mass window and the Voigtian captures the sharp peaking dimuon mass signal. Details in the analysis will be saved for after the overview of the statistical inference model.

To outline the typical approach in the profile likelihood method, the follow steps are done in an effort to set the limit

1. To form the test statistic, the *profile likelihood ratio* is used

$$\tilde{q}_\mu = -2 \ln \frac{\mathcal{L}(\text{data}|\mu, \hat{\theta}_\mu)}{\mathcal{L}_{\max}(\text{data}|\hat{\mu}, \hat{\theta})} \quad 0 \leq \hat{\mu} \leq \mu \quad (7.4)$$

Where  $\hat{\mu}$  and  $\hat{\theta}$  are the maximum likelihood estimators.

2. Find the *observed* value of the test statistic  $\tilde{q}_\mu^{\text{obs}}$  for given signal strength  $\mu$ .
3. Find values of the nuisance parameters that best describe the experimentally observed data by maximizing the likelihood.
4. Generate toy MC pseudo data to construct probability density functions for signal and background  $f(\tilde{q}_\mu|\mu, \hat{\theta}_\mu)$  and  $f(\tilde{q}_\mu|0, \hat{\theta}_\mu)$  for background only hypothesis. These pdfs are the pdfs of the test statistic under the assumption of a signal strength.
5. Generate toy MC pseudo data to construct probability density functions for signal and background  $f(\tilde{q}_\mu|\mu, \hat{\theta}_\mu)$  and  $f(\tilde{q}_\mu|0, \hat{\theta}_\mu)$  for background only hypothesis.
6. Define *p*-values to be associated with the actual observation for both  $s + b$  and  $b$  only hypotheses

$$p_\mu = P(\tilde{q}_\mu \geq \tilde{q}_\mu^{\text{obs}} | s + b) = \int_{\tilde{q}_\mu^{\text{obs}}}^{\infty} f(\tilde{q}_\mu|\mu, \hat{\theta}_\mu^{\text{obs}}) d\tilde{q}_\mu \quad (7.5)$$

$$1 - p_b = P(\tilde{q}_\mu \geq \tilde{q}_b^{obs} | b) = \int_{\tilde{q}_b^{obs}}^{\infty} f(\tilde{q}_\mu | \mu, \hat{\theta}_b^{obs}) d\tilde{q}_\mu \quad (7.6)$$

Then take the ratio to form the confidence levels

$$CL_s(\mu) = \frac{p_\mu}{1 - p_b} \quad (7.7)$$

7. Let  $\alpha$  be the measure of confidence, then for  $CL_s \leq \alpha$  then the signal hypothesis is rejected in favor of the background only hypothesis
8. Further to quote the 95% confidence level on  $\mu$ , we need to adjust the signal strength ( $\mu$ ) , until  $CL_s = 0.05$

## 7.2 Worked Example for Low Stat Analyses

Order of magnitude estimates for low stat analyses like the Higgs decay to pseudoscalars can be obtained by considering a very simple statistical inference model.

Suppose there are  $N$  events

$$N = B \cdot \sigma \cdot A \cdot \mathcal{L} \quad (7.8)$$

where  $B$  is the branching fraction for the physics process,  $A$  is the signal acceptance,  $\sigma$  is the cross section, and  $\mathcal{L}$  is the luminosity.

In general 7.8 works; however, a likelihood model is needed to fully get the estimate of the number of events expected.

As outlined in binned-likelihood models in CMS [30], suppose that the number of expected events follows a Poisson distribution. Then in that case if the background model would predict 0 average events, then the upper 95% bound in that case is 3.7 events.

Inverting the relation

$$B = \frac{N}{\sigma \cdot A \cdot \mathcal{L}} \quad (7.9)$$

Selecting the signal acceptance from the pseudoscalar analysis (2016  $\mu\mu\mu\tau$ )

$$A = \frac{\text{events pass all cuts}}{\text{starting events}} = \frac{1293}{250000} \approx 0.005 \quad (7.10)$$

and taking the cross section of the gluon gluon fusion for the parent particle in the decay chain  $\sigma = 48\text{pb}$  along with the luminosity for 2016  $\mathcal{L} = 35,900\text{pb}^{-1}$

Then the upper 95% limit on the branching fraction is

$$B = \frac{N}{\sigma \cdot A \cdot \mathcal{L}} = 0.00043 = 4.3 \times 10^{-4} \quad (7.11)$$

### 7.3 Fit model for pseudoscalar Higgs search

After the signal extraction cuts are applied, an unbinned parametric likelihood fit was done with various shapes depending on the background and signal categorization. There is one signal distribution depending on the hypothesized  $a$  mass, and two background distributions that are considered in the final fit. The two contributing background distributions originate from “Irreducible” events coming from two Z bosons (ZZ) and from “Reducible” events coming from jets faking tau leptons (FF).

For the signal, a Voigtian function is used to fit the pseudoscalar  $a$  mass spectrum in a small window - 2GeV - of the hypothesized  $a$  mass for the sample as in figure 7.2. The Voigtian shape was chosen to reflect the narrow simulated peak that is statistically smeared by experimental measurement. The Voigtian shape has one extra degree of freedom compared to the Gaussian. This parameter controls the Lorentzian factor in the Voigtian. For the signal MC the distributions tend to increase in standard deviation as the mass approaches 60 GeV. To compare the signal MC distributions, they are all plotted in figure 7.1.

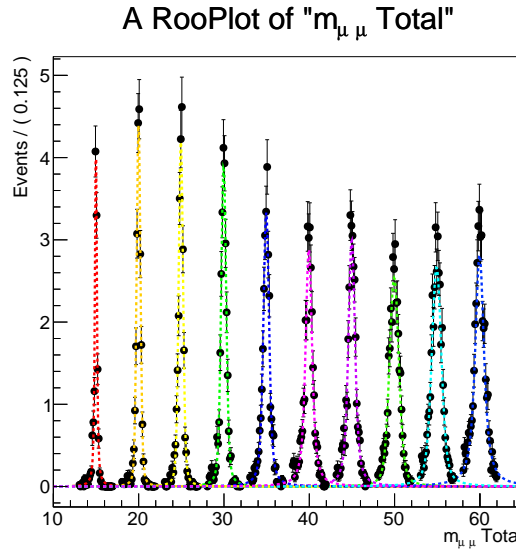


Figure 7.1: Signal fit using a Voigtian function

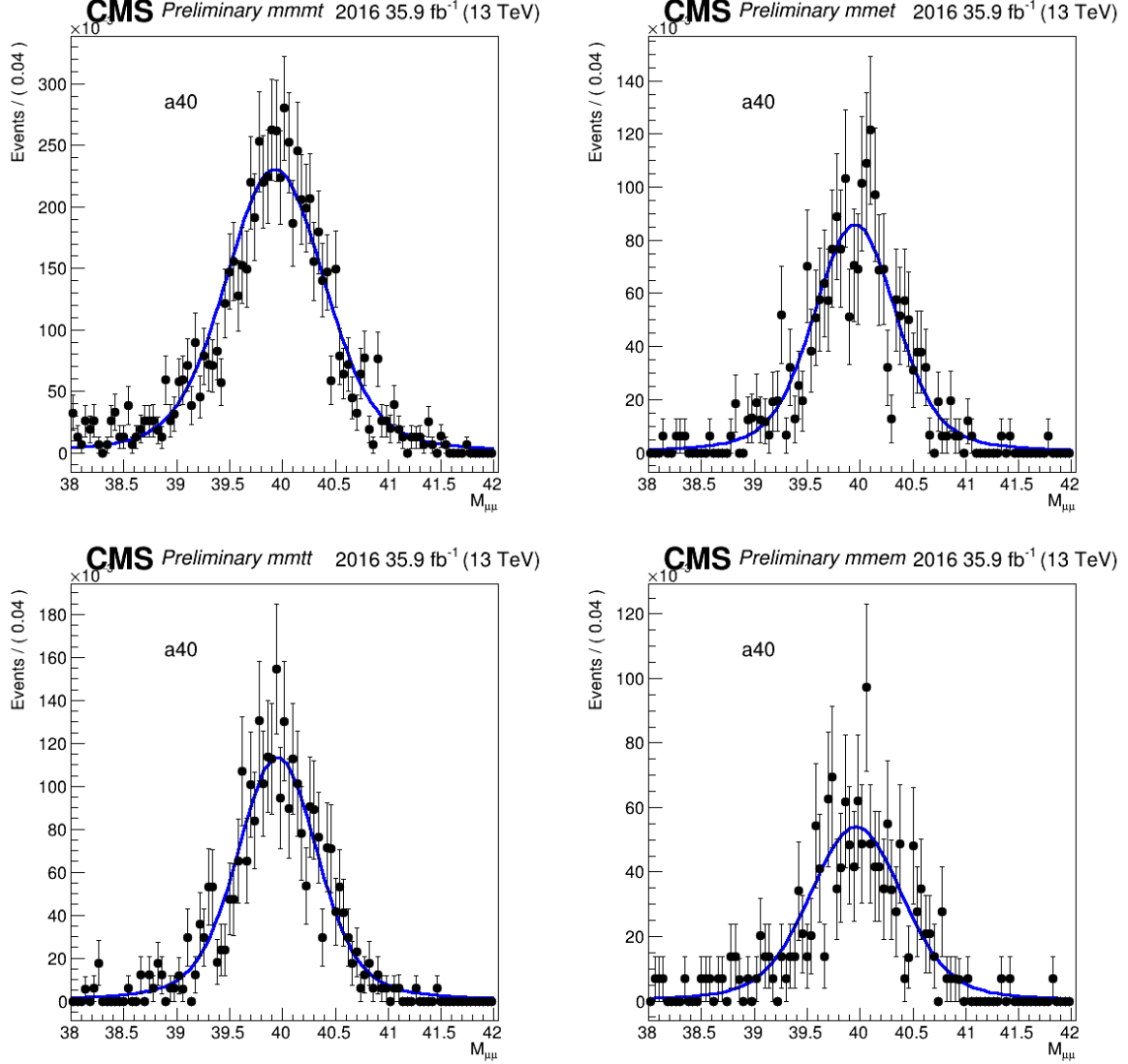


Figure 7.2: Signal fits using a voiigtian function for a-mass at 40GeV

Shapes from the signal samples in intervals of 5 GeV across the whole fit range 20-60 GeV are interpolated using spline functions. Thus precise limits can be obtained at the 1 GeV granularity. Predicated upon the fit model, using the spline in a refit would produce results that are close to the original fit to signal ensuring that in the statistical inference model that the signal is well modeled for all mass points. A spline function is necessary for each degree of freedom in the model. An example of such functions are shown in figure 7.3. The bands that envelope the spline indicate the spread and the accepted error on the spline in the statistical inference model, more details are discussed in the systematics section.

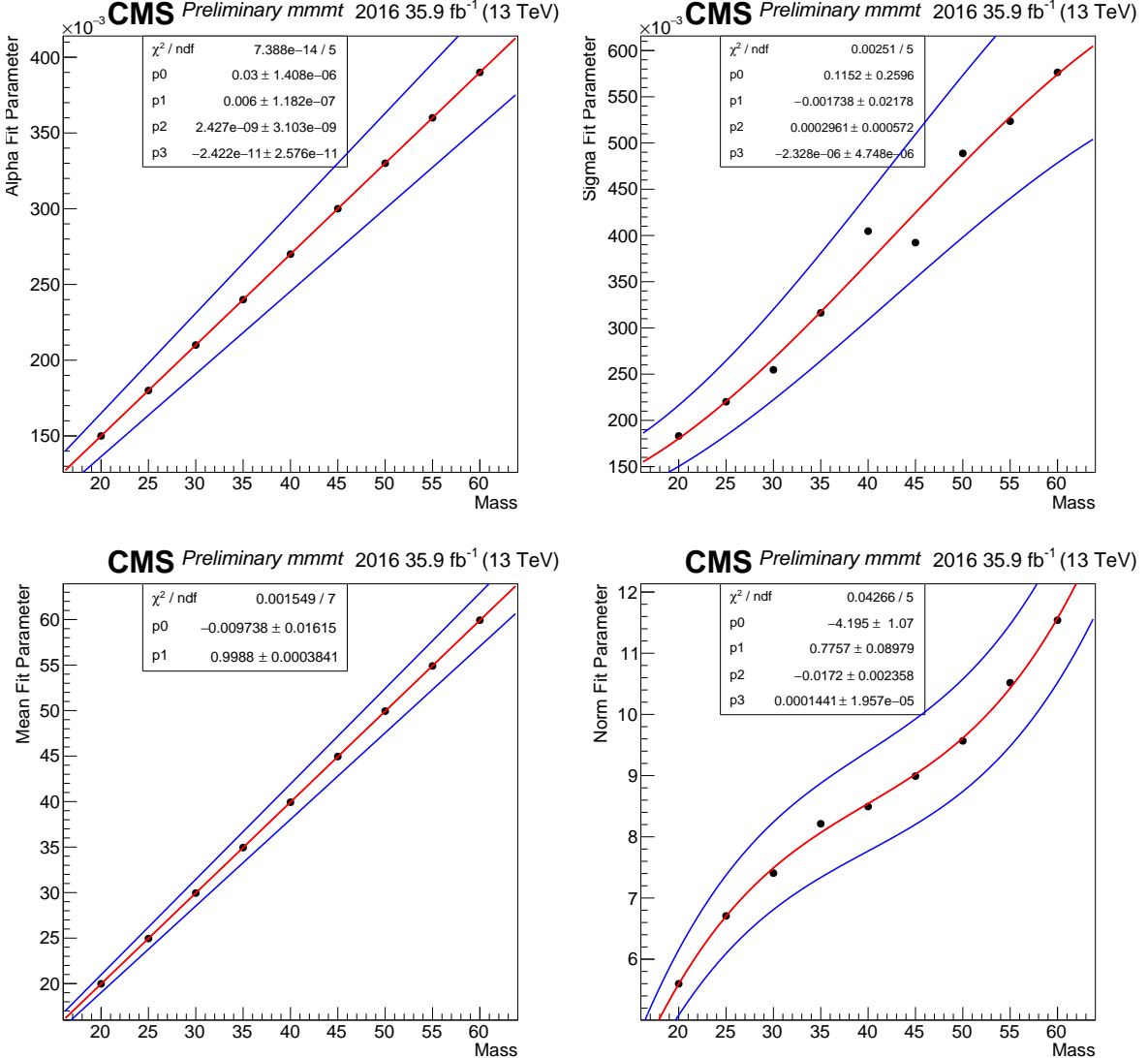


Figure 7.3: Spline functions for 2016 mmmmt a 3rd order polynomial is used for for Alpha, Sigma, and Normalization, a 1st order polynomial is used for the Mean

For the irreducible background coming from  $ZZ \rightarrow 4l$ , a Bernstein polynomial is used to fit the shape over the entire  $a$  mass range in figure 7.7. Depending on the final state and shape, the degree of the polynmoial is chosen by best fit. A Fischer F-test was conducted and there doesn't seem to be enough statistics in the bins to provide an accurate difference in the log-likelihood in order to recommend a particularly higher order polynomial over other orders. Thus for  $\mu\mu\tau\tau$  and  $\mu\mu\epsilon\tau$ , a a 1st order polynomial is used is used. For the channels that do have more events like  $\mu\mu\mu\tau$  and  $\mu\mu\epsilon\mu$  - albeit even for a lower number of integrated events - a parabolic order is used. The true values of the error estimation on the parameters are taken from the fit itself and can be

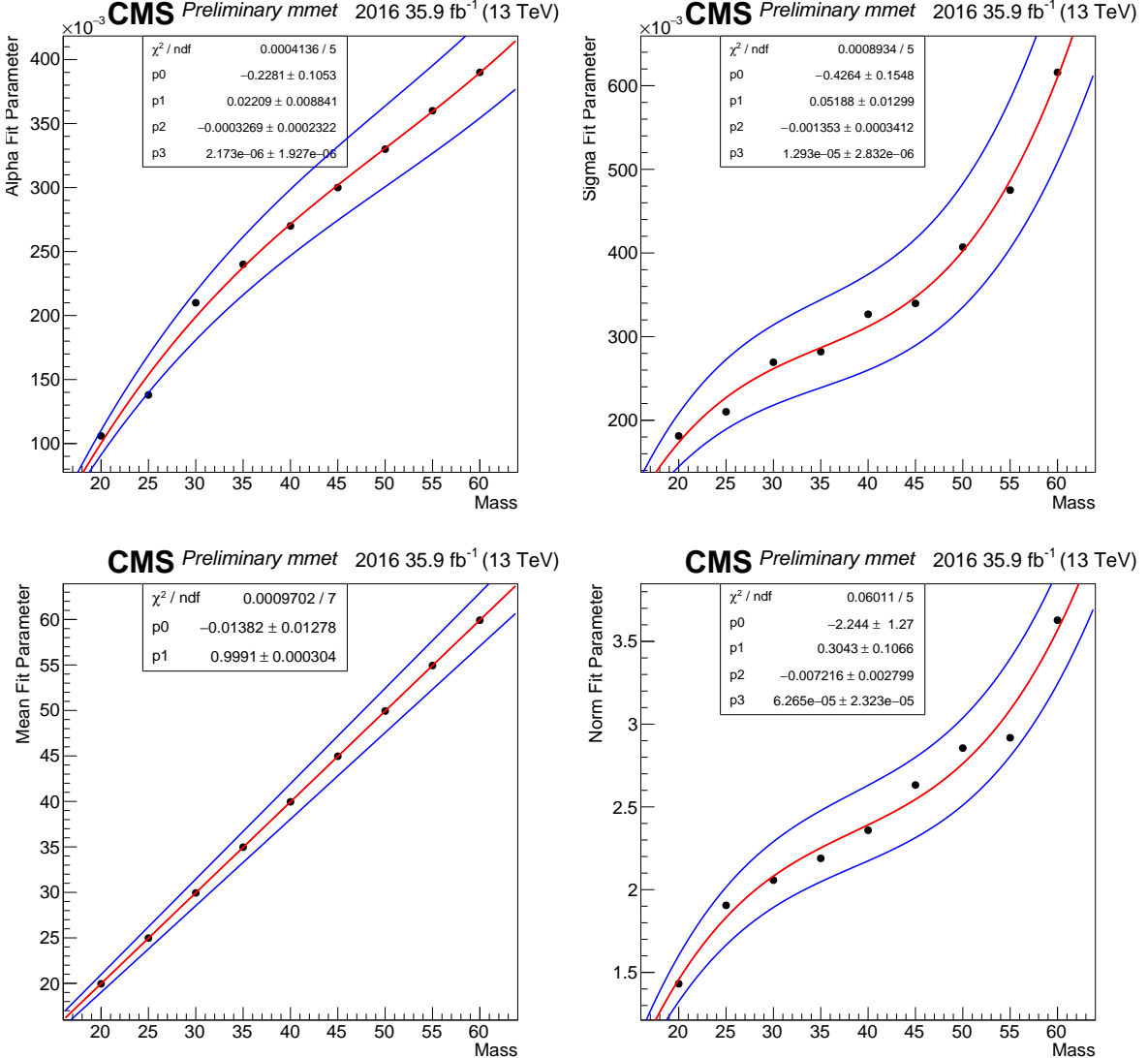


Figure 7.4: Spline functions for 2016 mmet a 3rd order polynomial is used for for Alpha, Sigma, and Normalization, a 1st order polynomial is used for the Mean

seen in the plots like figure 7.7. The error on these shape parameters are shown in the impacts which demonstrate how the fit parameters effect the overall statistical inference model C.1.

For the jet faking tau background, a Bernstein polynomial is also used to fit the shape over the entire  $a$  mass range in figure 7.8. Similar to the ZZ or irreducible background, the jet faking tau background polynomial degree is chosen by best fit.

The rest of the channels and years are shown in the appendix D.

Before a presentation of the expected limits on the branching fractions is given, a view of the uncertainty model is discussed here. In order to measure the systematic effects on the final

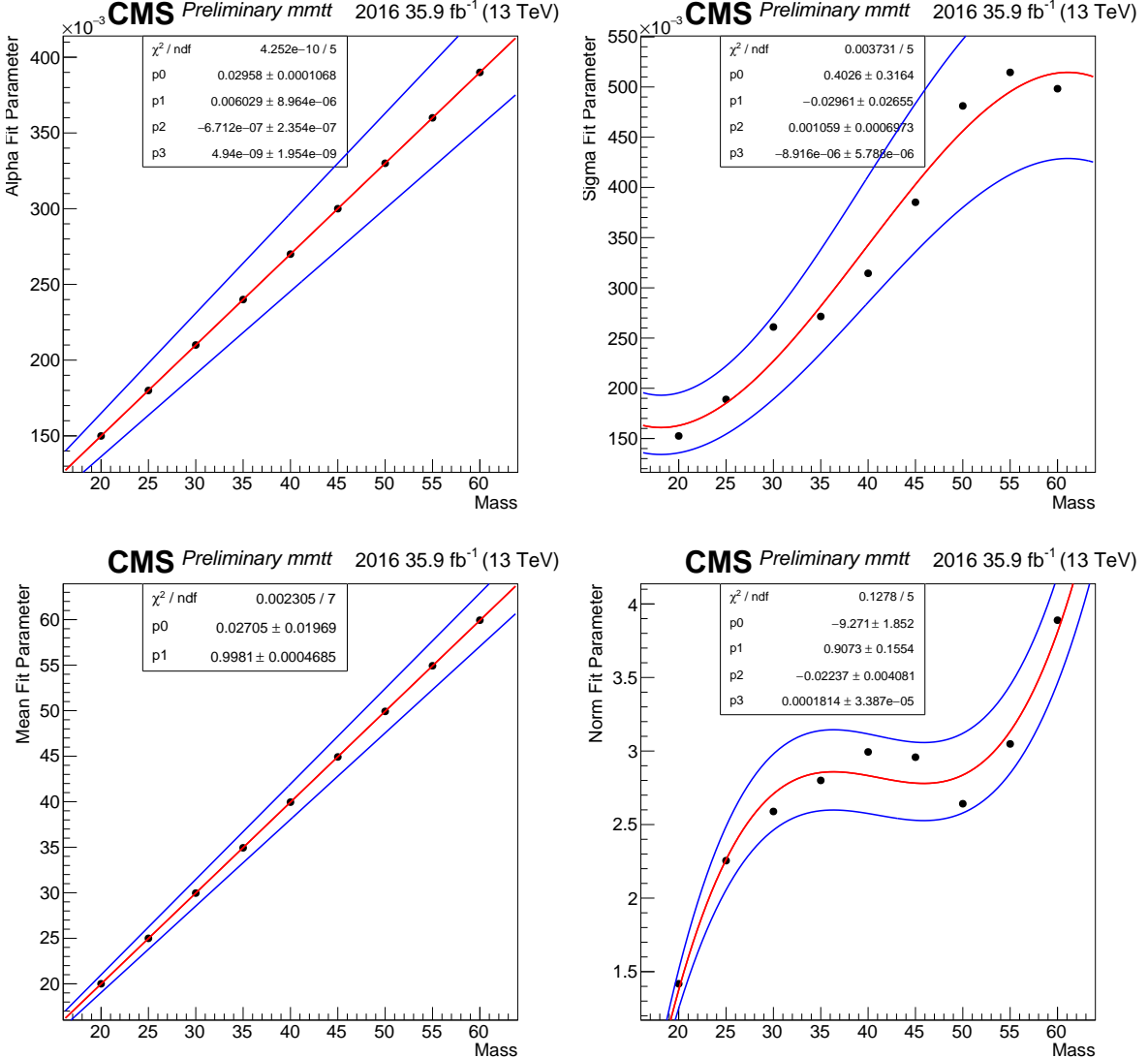


Figure 7.5: Spline functions for 2016 mm tt a 3rd order polynomial is used for for Alpha, Sigma, and Normalization, a 1st order polynomial is used for the Mean

distribution and the fits, changes in the fit templates are done and propagated to the fit model in the form of rate parameters. This is the accepted method to measure systematic impacts with a parametric fit model. These rate parameters differ slightly between the signal and background distributions. For background the error in the fit parameters are directly included in the uncertainty model.

For the signal, the uncertainty on the spline function is considered. As mentioned in the fit model section and shown in figure 7.3, the magnitude of this uncertainty is estimated from the fit of the parameters for the spline. Overall a 10% uncertainty is used for the lorentzian (alpha)

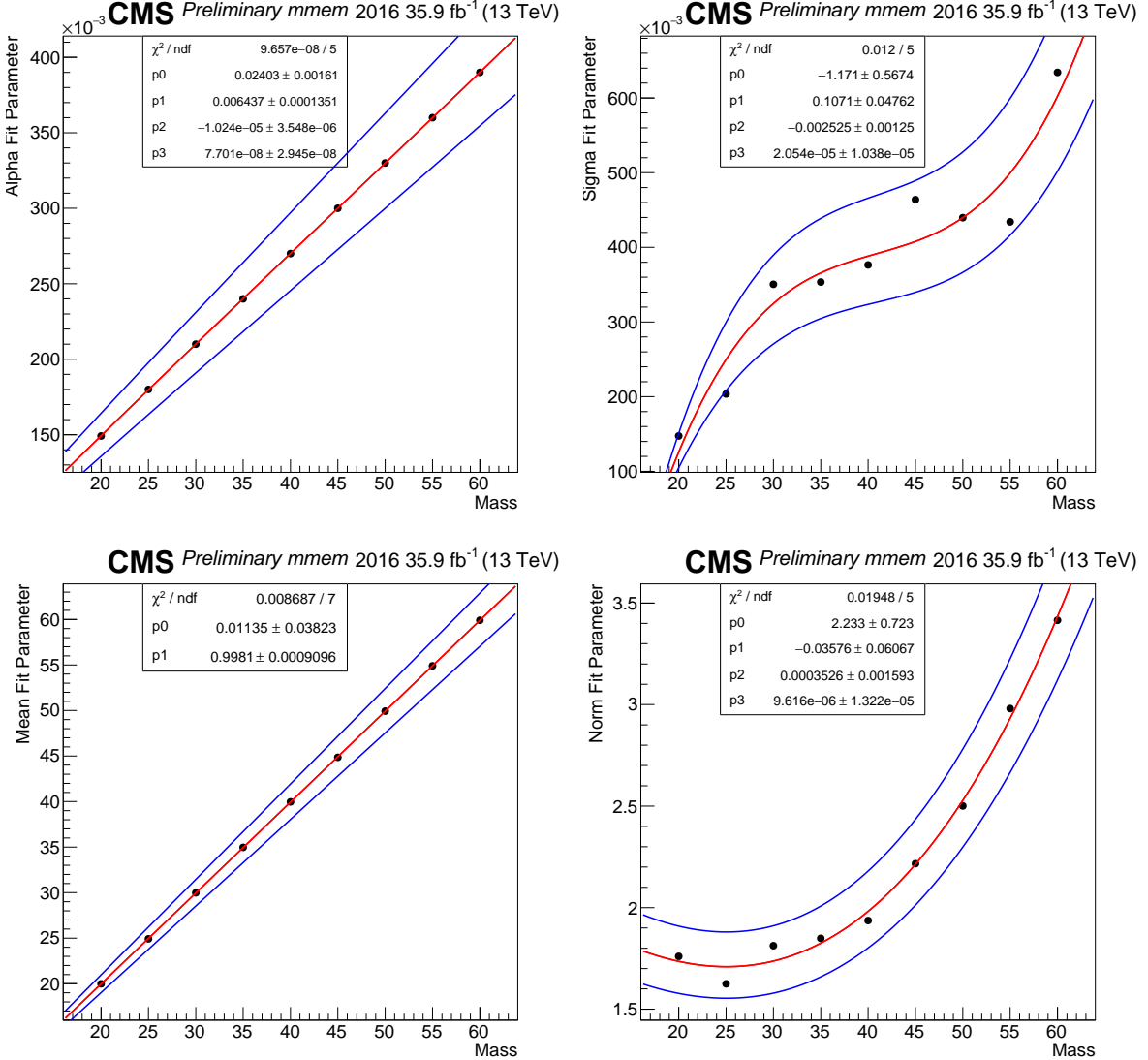


Figure 7.6: Spline functions for 2016 mmem a 3rd order polynomial is used for for Alpha, Sigma, and Normalization, a 1st order polynomial is used for the Mean

and 20% for the standard deviation (sigma) and 0.5% for the mean (mean). Although the mean is measured very precisely, the energy scale shifts from the leptons are included in this figure. Please look back at the section highlighting the uncertainties to see the bin-shift from the energy scale. The bin-shift indicates the amount the mean of the distribution is effected from the energy scale shift.

For the other systematic uncertainties that are not based on parametric shapes, like the energy scale of the leptons, a log-normal deviation to the normalization is considered. The extent to which these systematics effect the search is calculated through the concept of the “impact”. An impact

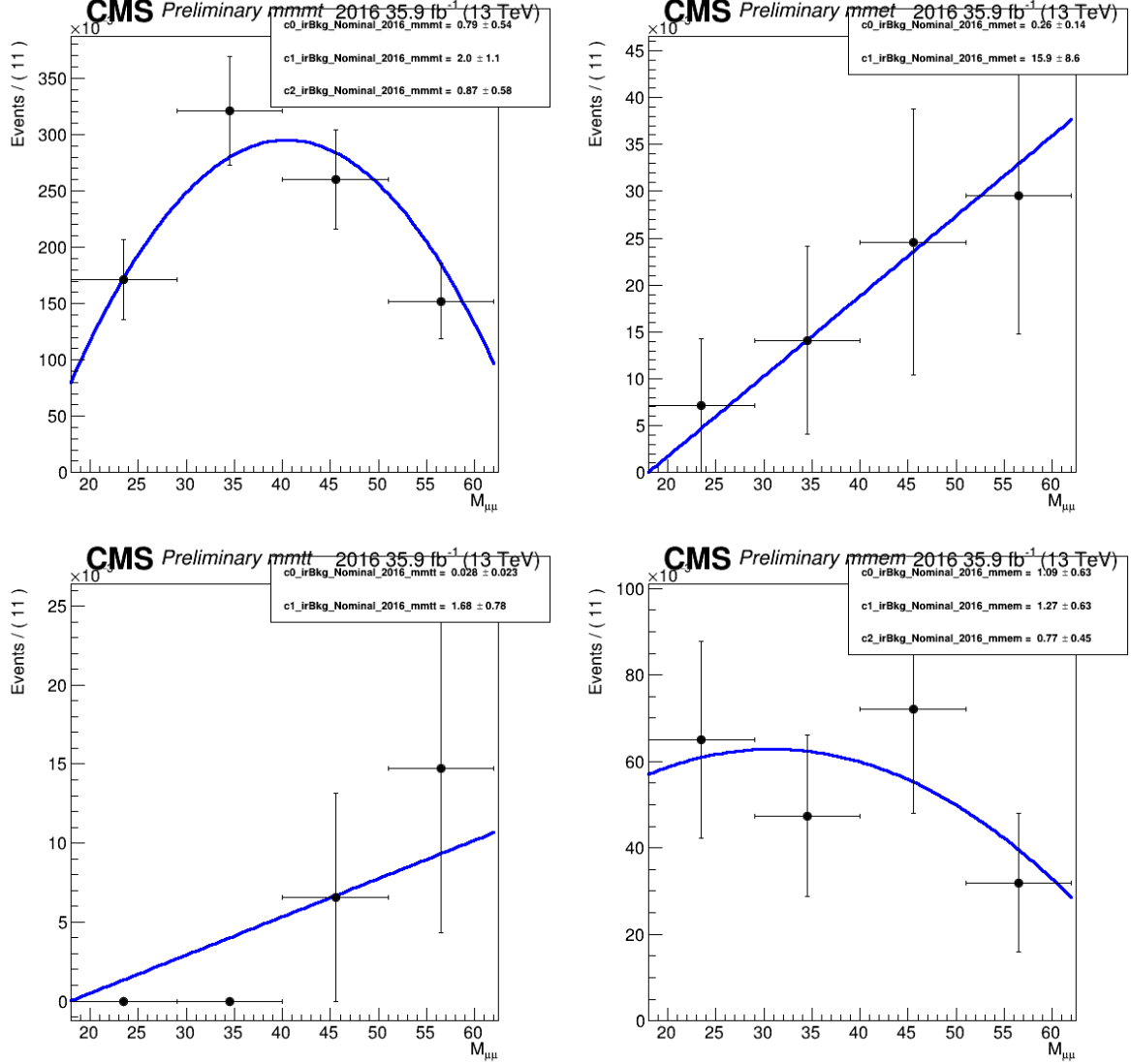


Figure 7.7: Irreducible background fit using Bernstein polynomials

is a way to see how that systematic uncertainty impacts the overall statistical model. To measure an impact for a particular systematic uncertainty, it is allowed to vary within the fit range while the rest of the parameters in the likelihood function are frozen. The corresponding difference in the signal strength is measured. In order to read the impact plots and to understand what the impacts represent in the fit model please look at table 7.1:

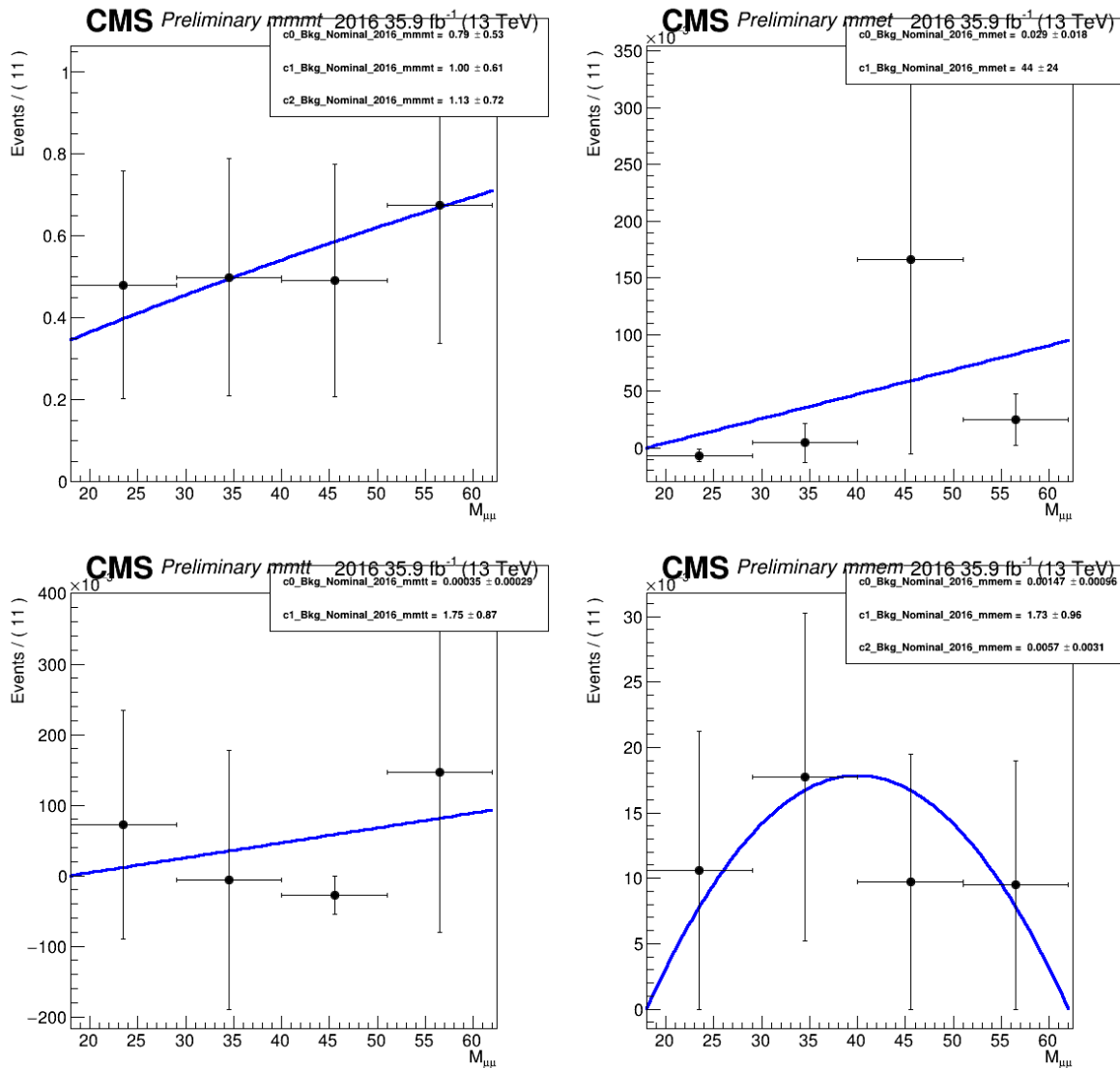


Figure 7.8: Reducible background fit using Bernstein polynomials

Table 7.1:

Type of Uncertainty	Brief Description
scale	log-normal uncertainties that effect overall scale of the distribution these include $e$ , $\mu$ , and $\tau$ (split by decay mode) energy scales
$c0_-, c1_-, \dots cN_-$	Coefficients of the Bkg (datadriven) or irBkg (ZZ) parametric shape
lumi	luminosity uncertainty (1.016 representing 1.6% uncertainty)
intAlpha	alpha interpolated spline function shape uncertainty (10%)
intSigma	sigma interpolated spline function shape uncertainty (20%)
intMean	mean interpolated spline function shape uncertainty energy scale shift uncertainties for signal included (5%)

Systematic impact distributions, sometimes referred to as pull distributions, is listed in figure 7.9. The rest of the channels and years are located in the appendix C.

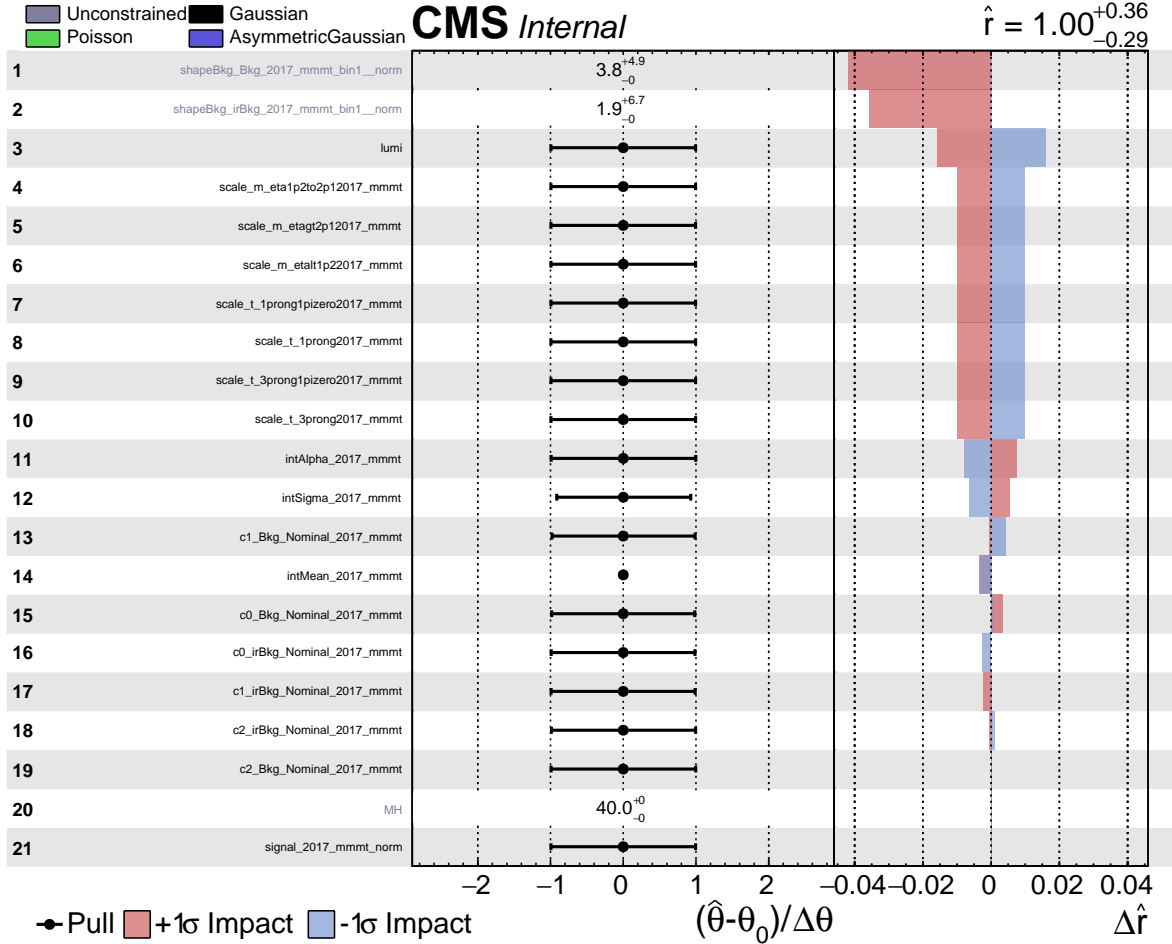


Figure 7.9: Expected systematic impacts for the fit model  $\mu\mu\tau$

# Chapter 8

## Conclusions

After the final event selection, including the signal extraction cuts listed in section 5.2.1, the statistical hypothesis test can be made. The final number of events listed in each category for the full Run II dataset is shown in the table below 8.1

Table 8.1: Expected event yields of signal and background categories across all years pertaining to  $137 \text{ fb}^{-1}$ .

Signal	Background	
$m_a = 40 \text{ GeV}$	Data Driven (FF)	Irreducible (ZZ)
6.54	23.61	6.33

Each unbinned parametric likelihood fit is included for each mass point into a confidence level scan to set an upper limit at 95% on the branching ratio. Initial values of the signal distributions are selected to make sure that the signal strength modifier in the limit is of order unity. The range of masses reflected are shown between 20 GeV and 60 GeV to ensure compatibility with Higgs combination limits for more exotic Higgs models—like those at lower  $a$  mass. In order to estimate the upper limit at 95% CL on the branching fraction a simple Poisson model can be used. For a statistically limited search we can choose to estimate the background yeild as no events. The upper limit on branching fraction calculated earlier:

$$B = \frac{N}{\sigma \cdot A \cdot \mathcal{L}} = 0.00043 \quad (8.1)$$

An upper limit of 95% is set on the branching fraction by adjusting the signal strength (event yield) until a p-value of 5% is reached on the joint likelihood function for the fit model. The event yield is normalized with a set branching fraction, which was assumed to be the Higgs  $\sigma_{SM} \times 0.01\%$ .

Multiplying the CL by 0.01% thus yields the limit on  $\frac{\sigma_h}{\sigma_{SM}} B(h \rightarrow aa \rightarrow 2\mu 2\tau)$ . Preliminary limits are set using the asymptotic limit method [30] for each mass point.

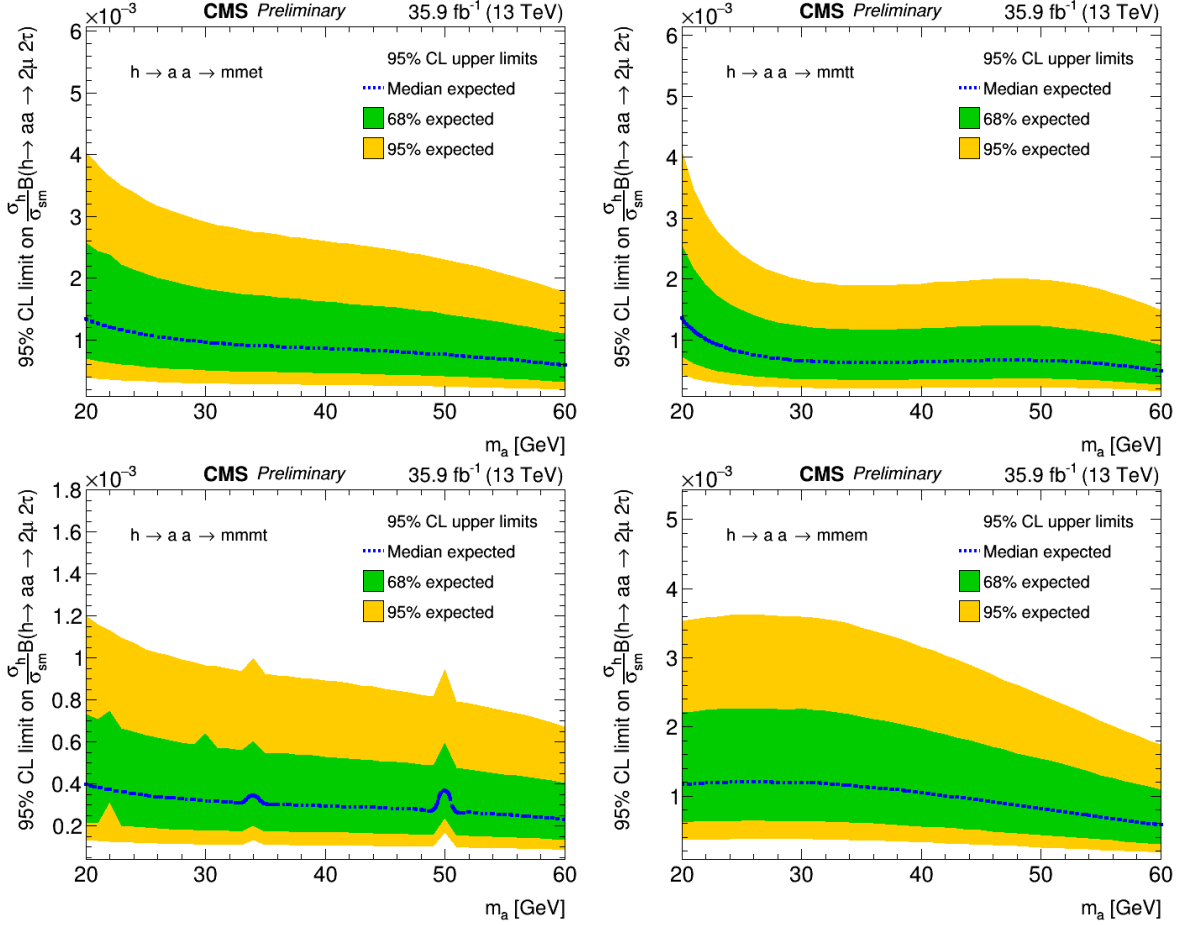


Figure 8.1: Asymptotic CL Limits on the branching fraction times ratio of the SM cross sections

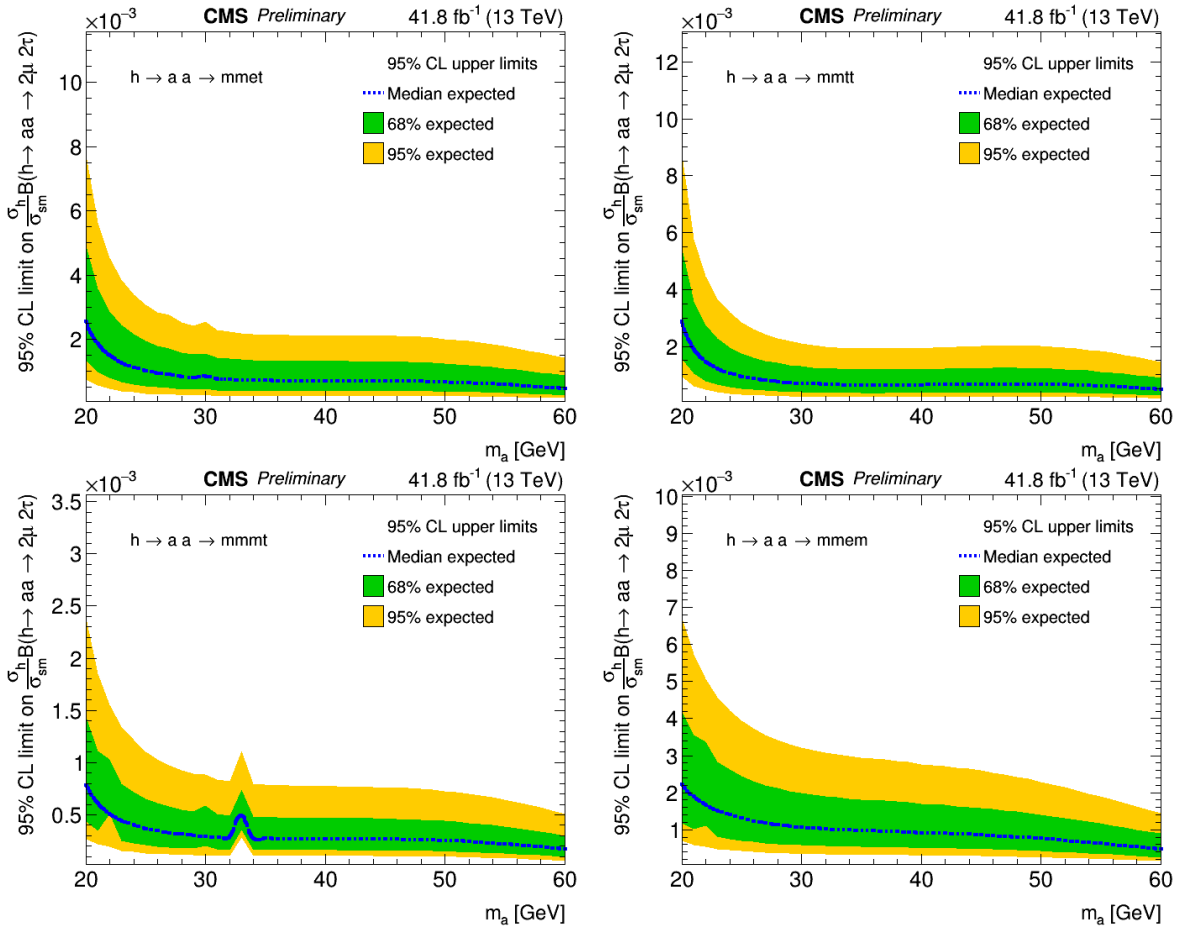


Figure 8.2: Asymptotic CL Limits on the branching fraction times ratio of the SM cross sections for 2017

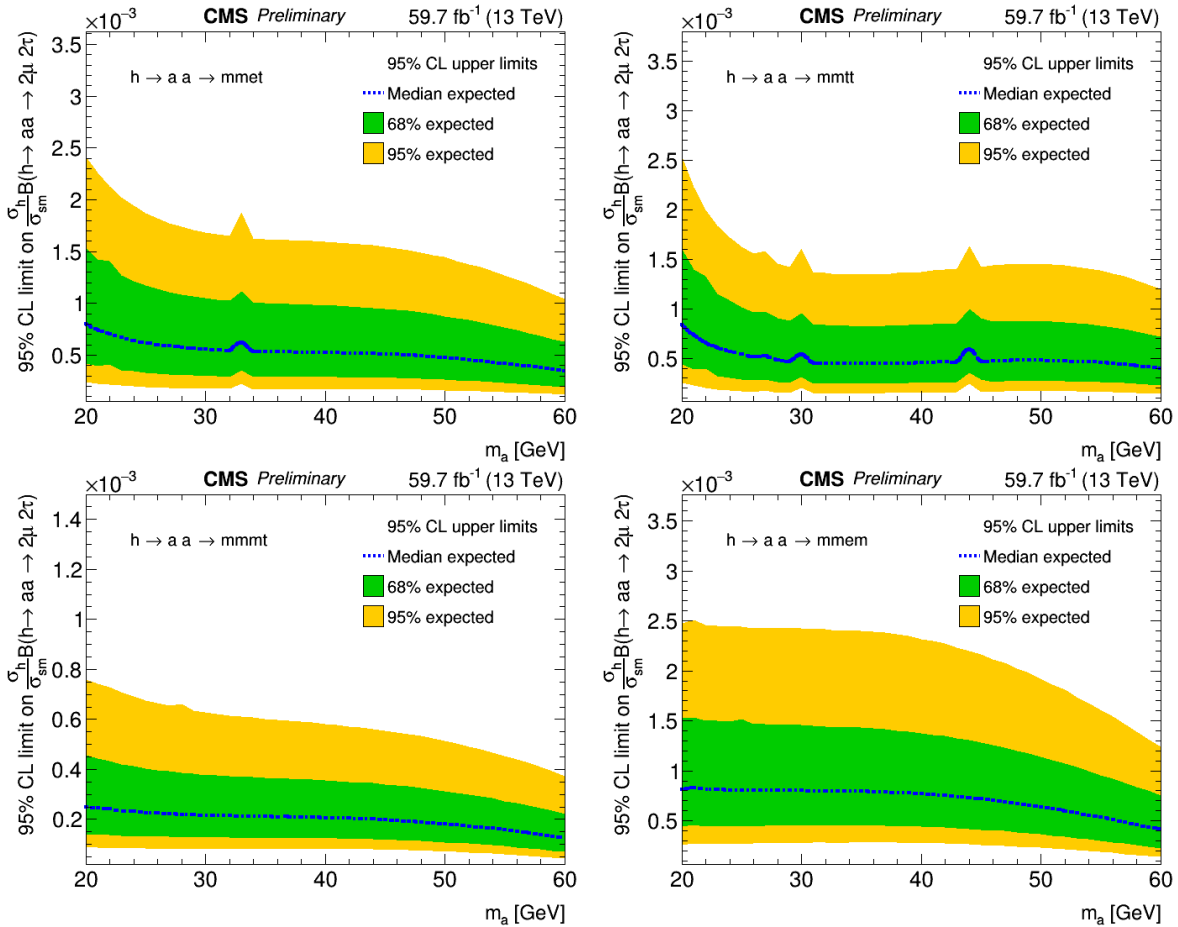


Figure 8.3: Asymptotic CL Limits on the branching fraction times ratio of the SM cross sections for 2018

All of the years and channels are then combined to form the combined result and the model 2HDM+S interpretations for different scenarios. Scenario type III where coupling to  $\tau$  leptons is favored is expected to be the most stringent scenario for this final state.

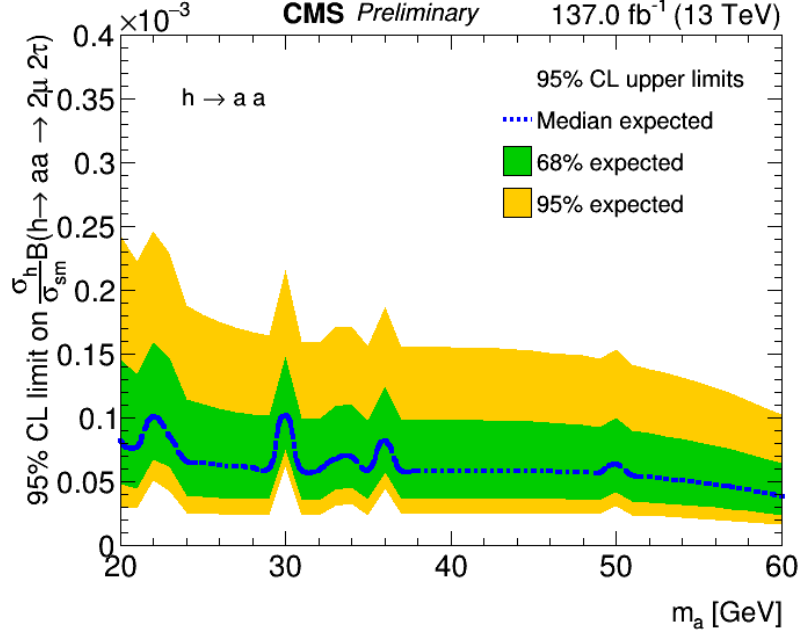


Figure 8.4: Asymptotic CL Limits on the branching fraction times ratio of the SM cross sections for the full Run II dataset  $137\text{fb}^{-1}$

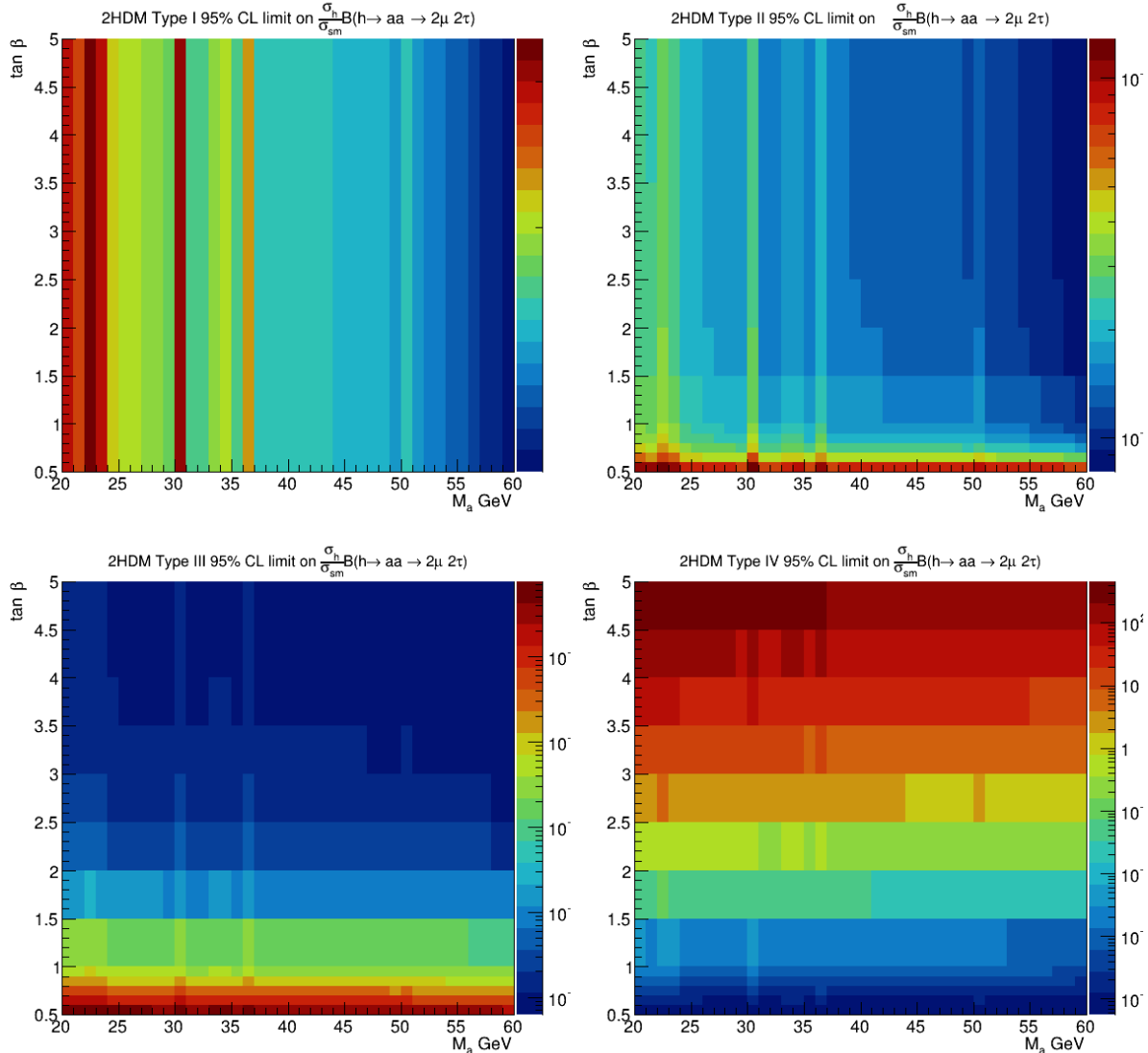


Figure 8.5: 2HDM model specific scenarios upper 95% CL limits on the branch fraction of Higgs to  $a a$  times the ratio of the SM cross sections for the full Run II dataset  $137\text{fb}^{-1}$

Pre-unblinding summary, final conclusion will be made after unblinding and observed results are obtained:

An overview of the Large Hadron Collider, CERN, CMS, luminosity operations, and an analysis focusing on the search for a BSM processes involving an exotic Higgs-like particle was presented. Using the full Run II dataset collected at CMS corresponding to an integrated luminosity of  $137\text{fb}^{-1}$ , the search for the Standard Model Higgs Boson,  $H$ , decaying to a pair of pseudoscalars,  $a$ , which then decay to pairs of muons and tau leptons was completed.

Expected upper 95% confidence level limits are about  $10^{-4}$  after addition of all final decay modes.

No excess was observed and furthermore the most stringent limits have been set for these decay modes.

These results are independent of separate 2HDMs and is considered a generic search that applies to multiple MSSM scenarios along with any BSM physics within the search window.

It has been an honor of a lifetime to work alongside CMS, Purdue, and Princeton University to deliver this analysis and years of service work!

## Appendix A

# Data and Simulation Samples

### A.1 Data and Simulation Used for Analysis

The full Run II dataset was used corresponding to  $137\text{fb}^{-1}$ .

Table A.1: List of data sets included in the analysis for the 2016 data taking period.

Data set
/SingleMuon/Run2016B_ver2-Nano250ct2019_ver2-v1/NANOAOD
/SingleMuon/Run2016B_ver1-Nano250ct2019_ver1-v1/NANOAOD
/SingleMuon/Run2016G-Nano250ct2019-v1/NANOAOD
/SingleMuon/Run2016F-Nano250ct2019-v1/NANOAOD
/SingleMuon/Run2016E-Nano250ct2019-v1/NANOAOD
/SingleMuon/Run2016D-Nano250ct2019-v1/NANOAOD
/SingleMuon/Run2016C-Nano250ct2019-v1/NANOAOD
/SingleMuon/Run2016H-Nano250ct2019-v1/NANOAOD
/DoubleMuon/Run2016H-Nano250ct2019-v1/NANOAOD
/DoubleMuon/Run2016G-Nano250ct2019-v1/NANOAOD
/DoubleMuon/Run2016F-Nano250ct2019-v1/NANOAOD
/DoubleMuon/Run2016B_ver2-Nano250ct2019_ver2-v1/NANOAOD
/DoubleMuon/Run2016B_ver1-Nano250ct2019_ver1-v1/NANOAOD
/DoubleMuon/Run2016E-Nano250ct2019-v1/NANOAOD
/DoubleMuon/Run2016D-Nano250ct2019-v1/NANOAOD
/DoubleMuon/Run2016C-Nano250ct2019-v1/NANOAOD

Table A.2: List of data sets included in the analysis for the 2017 data taking period.

Data set
/DoubleMuon/Run2017B-02Apr2020-v1/NANO AOD
/DoubleMuon/Run2017C-02Apr2020-v1/NANO AOD
/DoubleMuon/Run2017D-02Apr2020-v1/NANO AOD
/DoubleMuon/Run2017E-02Apr2020-v1/NANO AOD
/DoubleMuon/Run2017F-02Apr2020-v1/NANO AOD
/MuonEG/Run2017B-02Apr2020-v1/NANO AOD
/MuonEG/Run2017C-02Apr2020-v1/NANO AOD
/MuonEG/Run2017D-02Apr2020-v1/NANO AOD
/MuonEG/Run2017E-02Apr2020-v1/NANO AOD
/MuonEG/Run2017F-02Apr2020-v1/NANO AOD
/SingleMuon/Run2017B-02Apr2020-v1/NANO AOD
/SingleMuon/Run2017C-02Apr2020-v1/NANO AOD
/SingleMuon/Run2017D-02Apr2020-v1/NANO AOD
/SingleMuon/Run2017E-02Apr2020-v1/NANO AOD
/SingleMuon/Run2017F-02Apr2020-v1/NANO AOD
/DoubleEG/Run2017B-02Apr2020-v1/NANO AOD
/DoubleEG/Run2017C-02Apr2020-v1/NANO AOD
/DoubleEG/Run2017D-02Apr2020-v1/NANO AOD
/DoubleEG/Run2017E-02Apr2020-v1/NANO AOD
/DoubleEG/Run2017F-02Apr2020-v1/NANO AOD
/SingleElectron/Run2017B-02Apr2020-v1/NANO AOD
/SingleElectron/Run2017C-02Apr2020-v1/NANO AOD
/SingleElectron/Run2017D-02Apr2020-v1/NANO AOD
/SingleElectron/Run2017E-02Apr2020-v1/NANO AOD
/SingleElectron/Run2017F-02Apr2020-v1/NANO AOD

Table A.3: List of data sets included in the analysis for the 2018 data taking period.

Data set
/SingleMuon/Run2018A-02Apr2020-v1/NANO AOD
/SingleMuon/Run2018B-02Apr2020-v1/NANO AOD
/SingleMuon/Run2018C-02Apr2020-v1/NANO AOD
/SingleMuon/Run2018D-02Apr2020-v1/NANO AOD
/DoubleMuon/Run2018A-02Apr2020-v1/NANO AOD
/DoubleMuon/Run2018B-02Apr2020-v1/NANO AOD
/DoubleMuon/Run2018C-02Apr2020-v1/NANO AOD
/DoubleMuon/Run2018D-02Apr2020-v1/NANO AOD
/DoubleMuonLowMass/Run2018A-02Apr2020-v1/NANO AOD
/DoubleMuonLowMass/Run2018B-02Apr2020-v1/NANO AOD
/DoubleMuonLowMass/Run2018C-02Apr2020-v1/NANO AOD
/DoubleMuonLowMass/Run2018D-02Apr2020-v1/NANO AOD
/EGamma/Run2018A-02Apr2020-v1/NANO AOD
/EGamma/Run2018B-02Apr2020-v1/NANO AOD
/EGamma/Run2018C-02Apr2020-v1/NANO AOD
/EGamma/Run2018D-02Apr2020-v1/NANO AOD

Table A.4: List of data sets included in the analysis for the 2016 data taking period.

Table A.5: List of data sets included in the analysis for the 2017 data taking period.

Table A.6: List of data sets included in the analysis for the 2018 data taking period.

Monte Carlo Datasets for 2018
/DY1JetsToLL_M-50_TuneCP5_13TeV-madgraphMLM-pythia8/RunIIAutumn18NanoAODv7-Nano02Apr2020_102X_upgrade2018_realistic_v21-v1/NANOAODSIM
/DY2JetsToLL_M-50_TuneCP5_13TeV-madgraphMLM-pythia8/RunIIAutumn18NanoAODv7-Nano02Apr2020_102X_upgrade2018_realistic_v21-v1/NANOAODSIM
/DY3JetsToLL_M-50_TuneCP5_13TeV-madgraphMLM-pythia8/RunIIAutumn18NanoAODv7-Nano02Apr2020_102X_upgrade2018_realistic_v21-v1/NANOAODSIM
/DY4JetsToLL_M-50_TuneCP5_13TeV-madgraphMLM-pythia8/RunIIAutumn18NanoAODv7-Nano02Apr2020_102X_upgrade2018_realistic_v21-v1/NANOAODSIM
/DYJetsToLL_M-10to50_TuneCP5_13TeV-madgraphMLM-pythia8/RunIIAutumn18NanoAODv7-Nano02Apr2020_102X_upgrade2018_realistic_v21-v1/NANOAODSIM
/DYJetsToLL_M-10to50_TuneCP5_13TeV-madgraphMLM-pythia8/RunIIAutumn18NanoAODv7-Nano02Apr2020_102X_upgrade2018_realistic_v21-v1/NANOAODSIM
/W1jetsToLNu_TuneCP5_13TeV-madgraphMLM-pythia8/RunIIAutumn18NanoAODv7-Nano02Apr2020_102X_upgrade2018_realistic_v21-v1/NANOAODSIM
/W2jetsToLNu_TuneCP5_13TeV-madgraphMLM-pythia8/RunIIAutumn18NanoAODv7-Nano02Apr2020_102X_upgrade2018_realistic_v21-v1/NANOAODSIM
/W3jetsToLNu_TuneCP5_13TeV-madgraphMLM-pythia8/RunIIAutumn18NanoAODv7-Nano02Apr2020_102X_upgrade2018_realistic_v21-v1/NANOAODSIM
/W4jetsToLNu_TuneCP5_13TeV-madgraphMLM-pythia8/RunIIAutumn18NanoAODv7-Nano02Apr2020_102X_upgrade2018_realistic_v21-v1/NANOAODSIM
/WZTo3LNu_TuneCP5_13TeV_powheg_pythia8/RunIIAutumn18NanoAODv7-Nano02Apr2020_102X_upgrade2018_realistic_v21_ext1-v1/NANOAODSIM
/WW_4F_TuneCP5_13TeV_amcatnlo_pythia8/RunIIAutumn18NanoAODv7-Nano02Apr2020_102X_upgrade2018_realistic_v21_ext1-v1/NANOAODSIM
/WWZ_TuneCP5_13TeV_amcatnlo_pythia8/RunIIAutumn18NanoAODv7-Nano02Apr2020_102X_upgrade2018_realistic_v21_ext1-v1/NANOAODSIM
/WZZ_TuneCP5_13TeV_amcatnlo_pythia8/RunIIAutumn18NanoAODv7-Nano02Apr2020_102X_upgrade2018_realistic_v21_ext1-v1/NANOAODSIM
/ZZZ_TuneCP5_13TeV_amcatnlo_pythia8/RunIIAutumn18NanoAODv7-Nano02Apr2020_102X_upgrade2018_realistic_v21_ext1-v1/NANOAODSIM
/ttZJets_TuneCP5_13TeV_madgraphMLM_pythia8/RunIIAutumn18NanoAODv7-Nano02Apr2020_102X_upgrade2018_realistic_v21_ext1-v1/NANOAODSIM
/ttWJets_TuneCP5_13TeV_madgraphMLM_pythia8/RunIIAutumn18NanoAODv7-Nano02Apr2020_102X_upgrade2018_realistic_v21_ext1-v1/NANOAODSIM
/GluGluToContinToZTo2e2mu_13TeV_powheg_pythia8/RunIIAutumn18NanoAODv7-Nano02Apr2020_102X_upgrade2018_realistic_v21-v1/NANOAODSIM
/GluGluToContinToZTo2e2tau_13TeV_TuneCP5_MCFM701_pythia8/RunIIAutumn18NanoAODv7-Nano02Apr2020_102X_upgrade2018_realistic_v21-v1/NANOAODSIM
/GluGluToContinToZTo2mu2tau_13TeV_MCFM701_pythia8/RunIIAutumn18NanoAODv7-Nano02Apr2020_102X_upgrade2018_realistic_v21-v1/NANOAODSIM
/GluGluToContinToZTo4e_13TeV_MCFM701_pythia8/RunIIAutumn18NanoAODv7-Nano02Apr2020_102X_upgrade2018_realistic_v21_ext1-v1/NANOAODSIM
/GluGluToContinToZTo4e_13TeV_MCFM701_pythia8/RunIIAutumn18NanoAODv7-Nano02Apr2020_EXT_102X_upgrade2018_realistic_v21-v1/NANOAODSIM
/GluGluToContinToZTo4mu_13TeV_MCFM701_pythia8/RunIIAutumn18NanoAODv7-Nano02Apr2020_102X_upgrade2018_realistic_v21_ext1-v1/NANOAODSIM
/GluGluToContinToZTo4mu_13TeV_MCFM701_pythia8/RunIIAutumn18NanoAODv7-Nano02Apr2020_EXT_102X_upgrade2018_realistic_v21-v1/NANOAODSIM
/GluGluToContinToZTo4tau_13TeV_MCFM701_pythia8/RunIIAutumn18NanoAODv7-Nano02Apr2020_EXT_102X_upgrade2018_realistic_v21-v1/NANOAODSIM
/HZJ_HToWW_M125_13TeV_powheg_jhugen74_pythia8_TuneCP5/RunIIAutumn18NanoAODv7-Nano02Apr2020_102X_upgrade2018_realistic_v21-v1/NANOAODSIM
/ZZTo4L_TuneCP5_13TeV_powheg_pythia8/RunIIAutumn18NanoAODv7-Nano02Apr2020_102X_upgrade2018_realistic_v21_ext1-v1/NANOAODSIM
/ZZTo4L_TuneCP5_13TeV_powheg_pythia8/RunIIAutumn18NanoAODv7-Nano02Apr2020_102X_upgrade2018_realistic_v21_ext2-v1/NANOAODSIM
/ZZTo4L_13TeV_powheg_pythia8_TuneCP5/RunIIAutumn18NanoAODv7-Nano02Apr2020_102X_upgrade2018_realistic_v21-v1/NANOAODSIM
/ggZH_HToTauTau_ZToNuNu_M125_13TeV_powheg_pythia8/RunIIAutumn18NanoAODv7-Nano02Apr2020_102X_upgrade2018_realistic_v21-v1/NANOAODSIM
/ggZH_HToTauTau_ZToQQ_M125_13TeV_powheg_pythia8/RunIIAutumn18NanoAODv7-Nano02Apr2020_102X_upgrade2018_realistic_v21-v1/NANOAODSIM
/GluGluZH_HToWW_M125_13TeV_powheg_pythia8_TuneCP5_PSweights/RunIIAutumn18NanoAODv7-Nano02Apr2020_102X_upgrade2018_realistic_v21-v1/NANOAODSIM
/WminusToTauTau_M125_13TeV_powheg_pythia8/RunIIAutumn18NanoAODv7-Nano02Apr2020_102X_upgrade2018_realistic_v21-v1/NANOAODSIM
/WplusHToTauTau_M125_13TeV_powheg_pythia8/RunIIAutumn18NanoAODv7-Nano02Apr2020_102X_upgrade2018_realistic_v21-v1/NANOAODSIM
/ZHTauTau_M125_13TeV_powheg_pythia8/RunIIAutumn18NanoAODv7-Nano02Apr2020_102X_upgrade2018_realistic_v21-v1/NANOAODSIM
/HminusJ_HToWW_M125_13TeV_powheg_jhugen724_pythia8_TuneCP5/RunIIAutumn18NanoAODv7-Nano02Apr2020_102X_upgrade2018_realistic_v21-v1/NANOAODSIM
/HWplusJ_HToWW_M125_13TeV_powheg_jhugen724_pythia8_TuneCP5/RunIIAutumn18NanoAODv7-Nano02Apr2020_102X_upgrade2018_realistic_v21-v1/NANOAODSIM
/eos/home-s/shigginb/HAA_ntuples/ggha01a01Tomumutautau_2018_dtau_M15/
/eos/home-s/shigginb/HAA_ntuples/ggha01a01Tomumutautau_2018_dtau_M20/
/eos/home-s/shigginb/HAA_ntuples/ggha01a01Tomumutautau_2018_dtau_M25/
/eos/home-s/shigginb/HAA_ntuples/ggha01a01Tomumutautau_2018_dtau_M30/
/eos/home-s/shigginb/HAA_ntuples/ggha01a01Tomumutautau_2018_dtau_M35/
/eos/home-s/shigginb/HAA_ntuples/ggha01a01Tomumutautau_2018_dtau_M40/
/eos/home-s/shigginb/HAA_ntuples/ggha01a01Tomumutautau_2018_dtau_M45/
/eos/home-s/shigginb/HAA_ntuples/ggha01a01Tomumutautau_2018_dtau_M50/
/eos/home-s/shigginb/HAA_ntuples/ggha01a01Tomumutautau_2018_dtau_M55/
/eos/home-s/shigginb/HAA_ntuples/ggha01a01Tomumutautau_2018_dtau_M60/

## Appendix B

# Fake Rate Measurements

These figures show the rest of the datadriven background estimation on the rate at which jets fake tau leptons in QCD, ttbar, and W+jet regions. The y-axis can be interpreted as the percent fake rate.

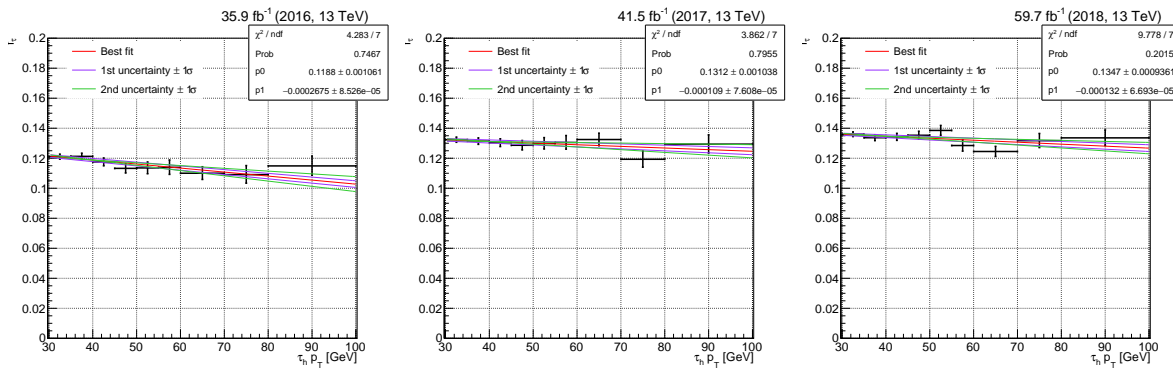


Figure B.1: Fake factors determined in the W+jets determination region with 0 jet in the  $e\tau_h$  final state in 2016 (left), 2017 (center), and 2018 (right). They are fitted with linear functions as a function of the  $\tau_h p_T$ . The green and purple lines indicate the shape systematics obtained by uncorrelating the uncertainties in the two fit parameters returned by the fit.

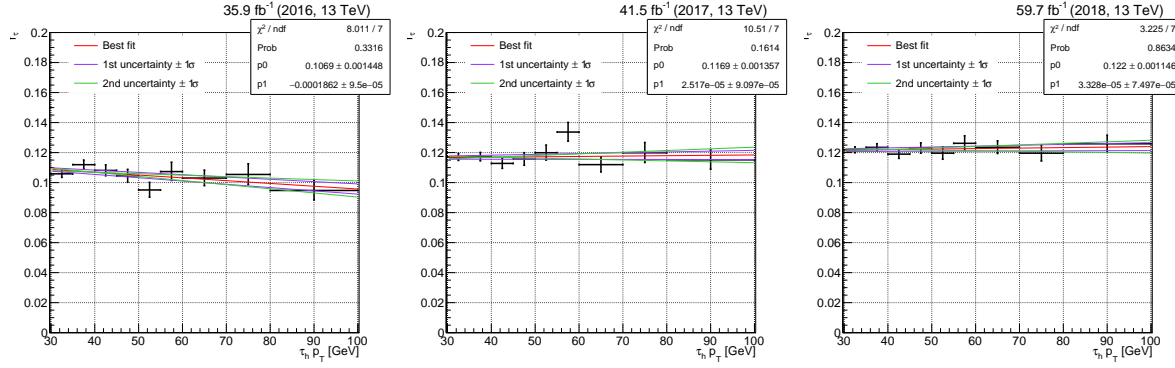


Figure B.2: Fake factors determined in the W+jets determination region with one jet in the  $e\tau_h$  final state in 2016 (left), 2017 (center), and 2018 (right). They are fitted with linear functions as a function of the  $\tau_h p_T$ . The green and purple lines indicate the shape systematics obtained by uncorrelating the uncertainties in the two fit parameters returned by the fit.

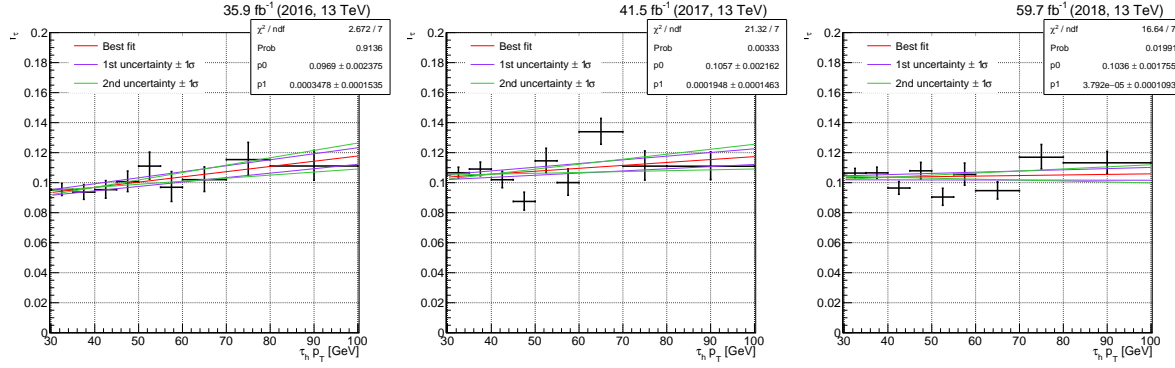


Figure B.3: Fake factors determined in the W+jets determination region with at least two jets in the  $e\tau_h$  final state in 2016 (left), 2017 (center), and 2018 (right). They are fitted with linear functions as a function of the  $\tau_h p_T$ . The green and purple lines indicate the shape systematics obtained by uncorrelating the uncertainties in the two fit parameters returned by the fit.

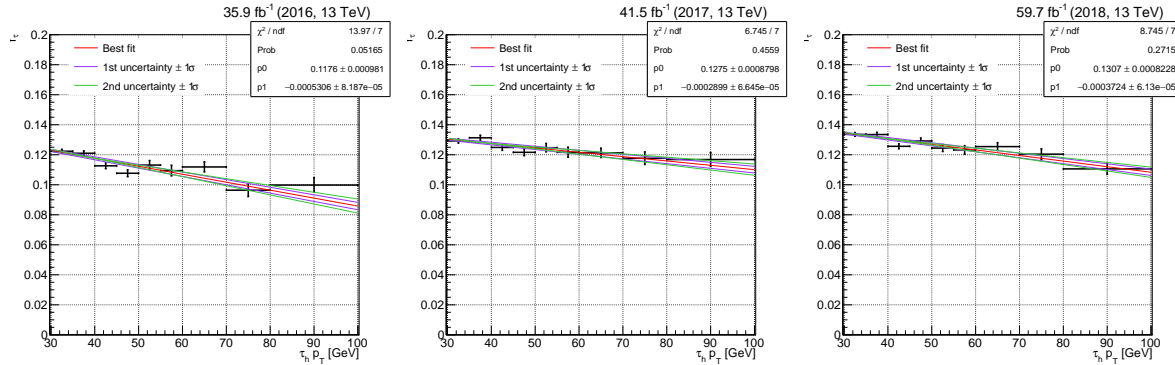


Figure B.4: Fake factors determined in the W+jets determination region with 0 jet in the  $\tau_h$  final state in 2016 (left), 2017 (center), and 2018 (right). They are fitted with linear functions as a function of the  $\tau_h p_T$ . The green and purple lines indicate the shape systematics obtained by uncorrelating the uncertainties in the two fit parameters returned by the fit.

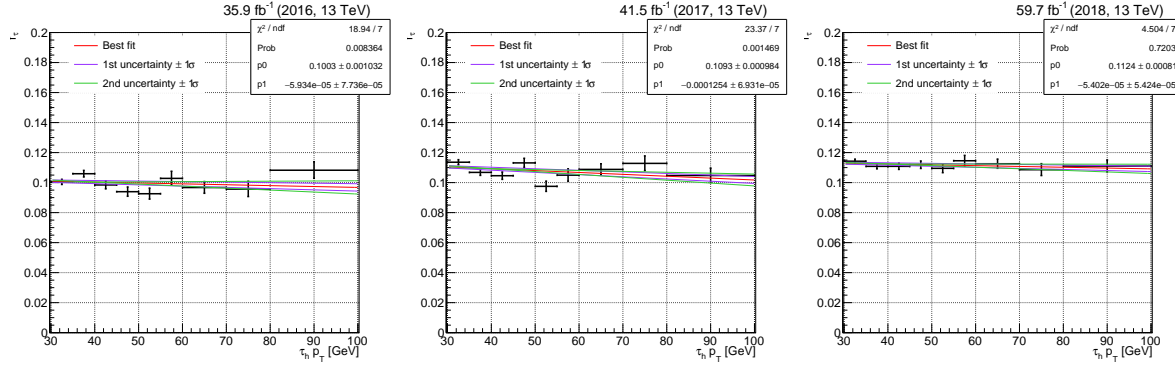


Figure B.5: Fake factors determined in the W+jets determination region with one jet in the  $\tau_h$  final state in 2016 (left), 2017 (center), and 2018 (right). They are fitted with linear functions as a function of the  $\tau_h p_T$ . The green and purple lines indicate the shape systematics obtained by uncorrelating the uncertainties in the two fit parameters returned by the fit.

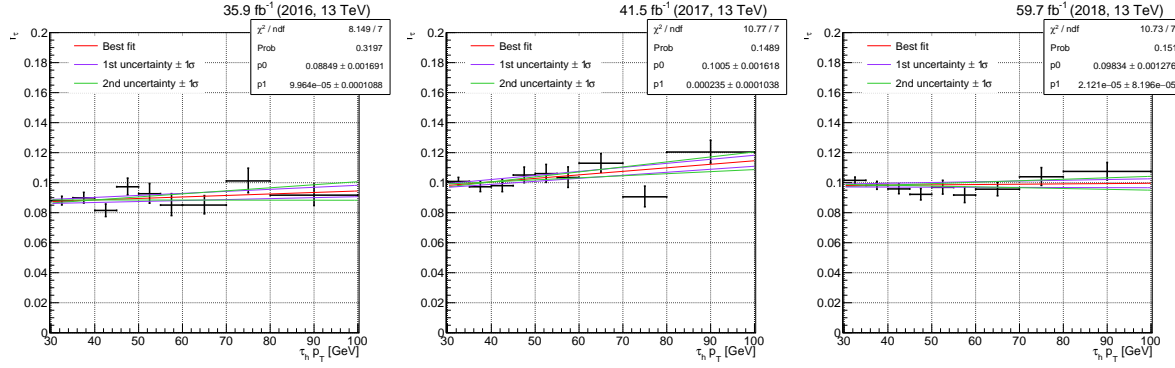


Figure B.6: Fake factors determined in the W+jets determination region with at least two jets in the  $\tau_h$  final state in 2016 (left), 2017 (center), and 2018 (right). They are fitted with linear functions as a function of the  $\tau_h p_T$ . The green and purple lines indicate the shape systematics obtained by uncorrelating the uncertainties in the two fit parameters returned by the fit.

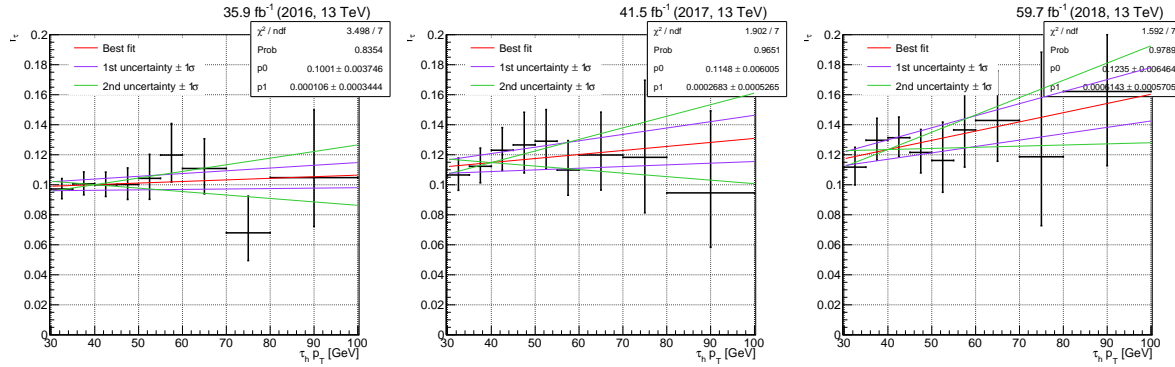


Figure B.7: Fake factors determined in the QCD multijet determination region with 0 jet in the  $\tau_h$  final state in 2016 (left), 2017 (center), and 2018 (right). They are fitted with linear functions as a function of the  $\tau_h p_T$ . The green and purple lines indicate the shape systematics obtained by uncorrelating the uncertainties in the two fit parameters returned by the fit.

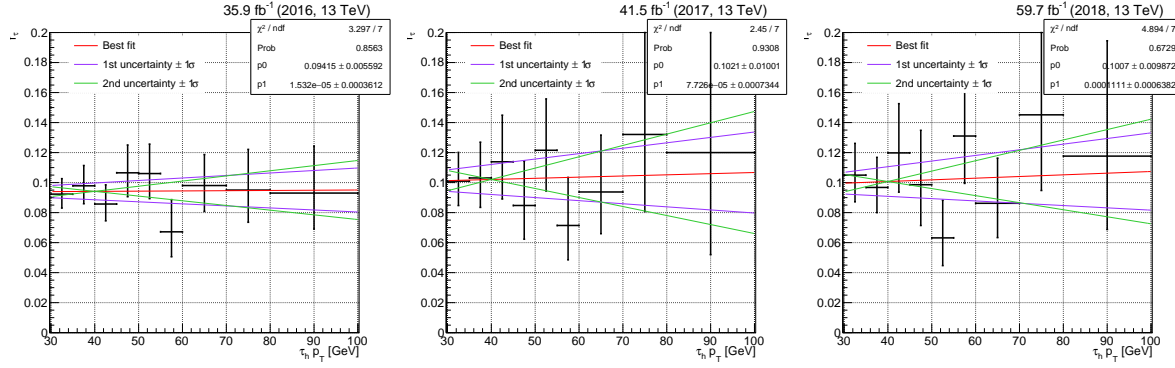


Figure B.8: Fake factors determined in the QCD multijet determination region with one jet in the  $e\tau_h$  final state in 2016 (left), 2017 (center), and 2018 (right). They are fitted with linear functions as a function of the  $\tau_h p_T$ . The green and purple lines indicate the shape systematics obtained by uncorrelating the uncertainties in the two fit parameters returned by the fit.

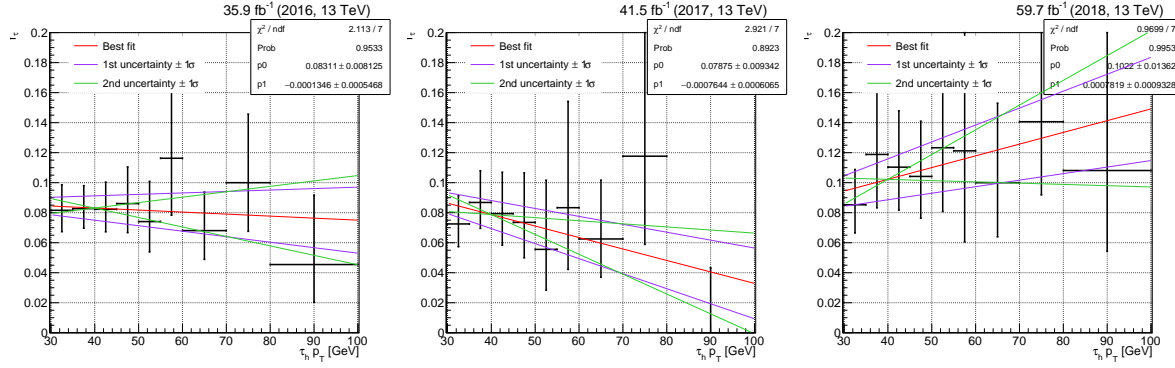


Figure B.9: Fake factors determined in the QCD multijet determination region with at least two jets in the  $e\tau_h$  final state in 2016 (left), 2017 (center), and 2018 (right). They are fitted with linear functions as a function of the  $\tau_h p_T$ . The green and purple lines indicate the shape systematics obtained by uncorrelating the uncertainties in the two fit parameters returned by the fit.

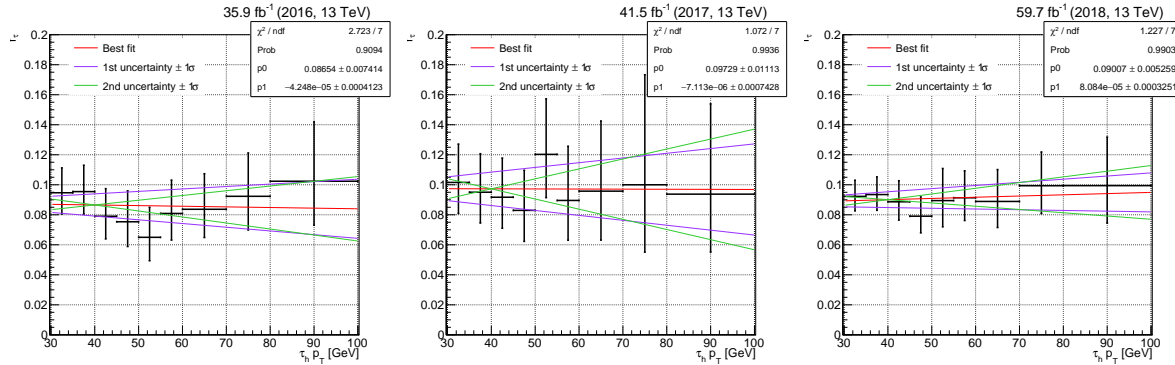


Figure B.10: Fake factors determined in the QCD multijet determination region with one jet in the  $\tau_h$  final state in 2016 (left), 2017 (center), and 2018 (right). They are fitted with linear functions as a function of the  $\tau_h p_T$ . The green and purple lines indicate the shape systematics obtained by uncorrelating the uncertainties in the two fit parameters returned by the fit.

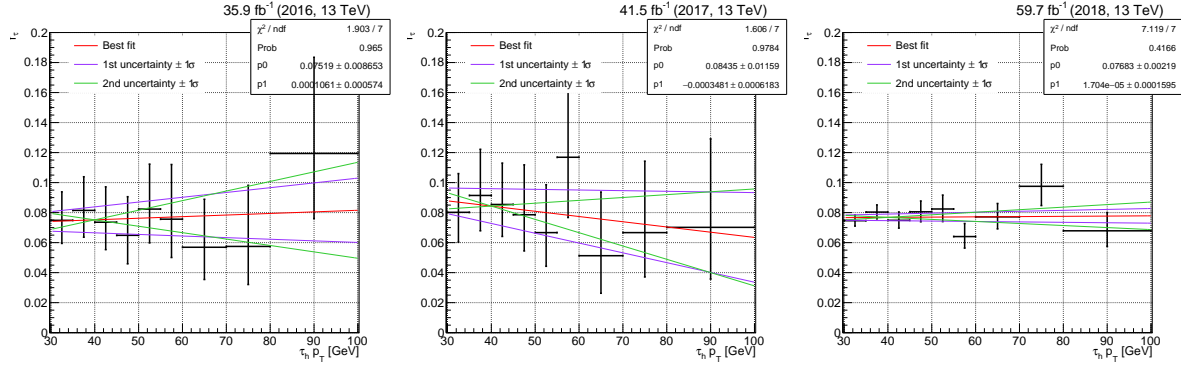


Figure B.11: Fake factors determined in the QCD multijet determination region with at least two jets in the  $\tau_h$  final state in 2016 (left), 2017 (center), and 2018 (right). They are fitted with linear functions as a function of the  $\tau_h$   $p_T$ . The green and purple lines indicate the shape systematics obtained by uncorrelating the uncertainties in the two fit parameters returned by the fit.

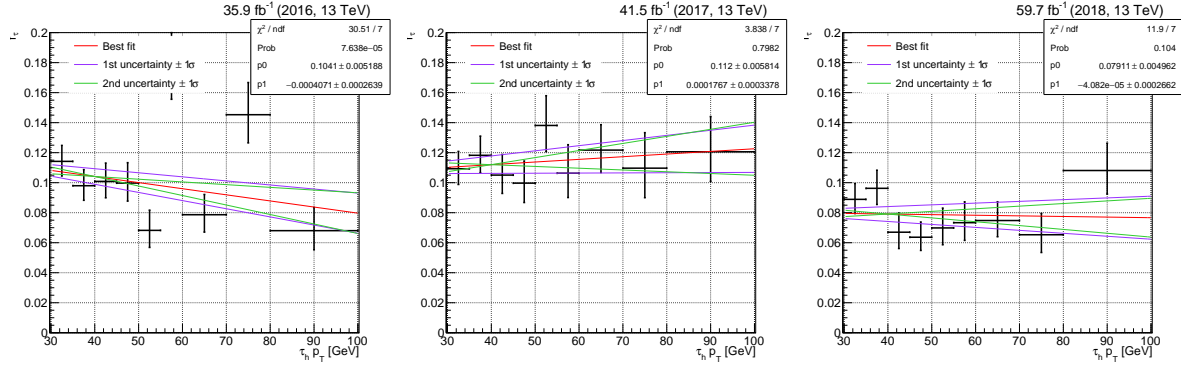


Figure B.12: Fake factors determined in the  $t\bar{t}$  determination region in data in the  $e\tau_h$  final state in 2016 (left), 2017 (center), and 2018 (right). They are fitted with linear functions as a function of the  $\tau_h$   $p_T$ . The green and purple lines indicate the shape systematics obtained by uncorrelating the uncertainties in the two fit parameters returned by the fit.

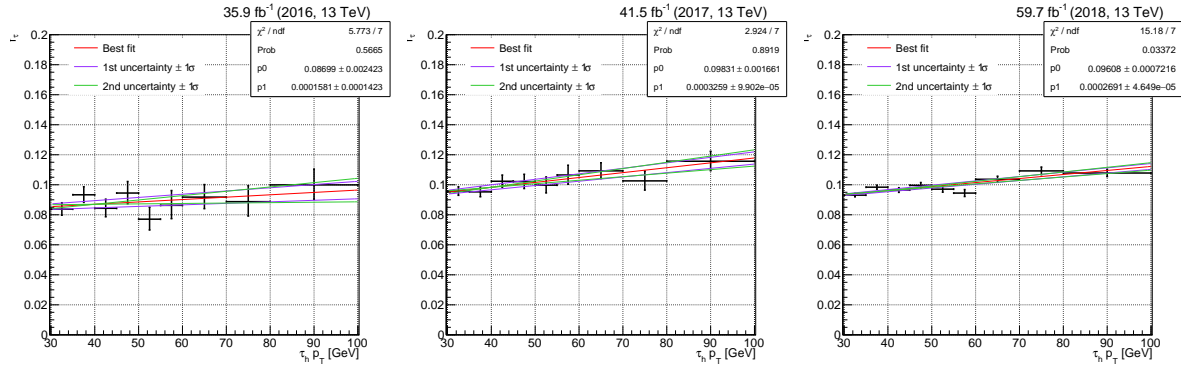


Figure B.13: Fake factors determined in the  $t\bar{t}$  simulation in the  $e\tau_h$  final state in 2016 (left), 2017 (center), and 2018 (right). They are fitted with linear functions as a function of the  $\tau_h$   $p_T$ . The green and purple lines indicate the shape systematics obtained by uncorrelating the uncertainties in the two fit parameters returned by the fit.

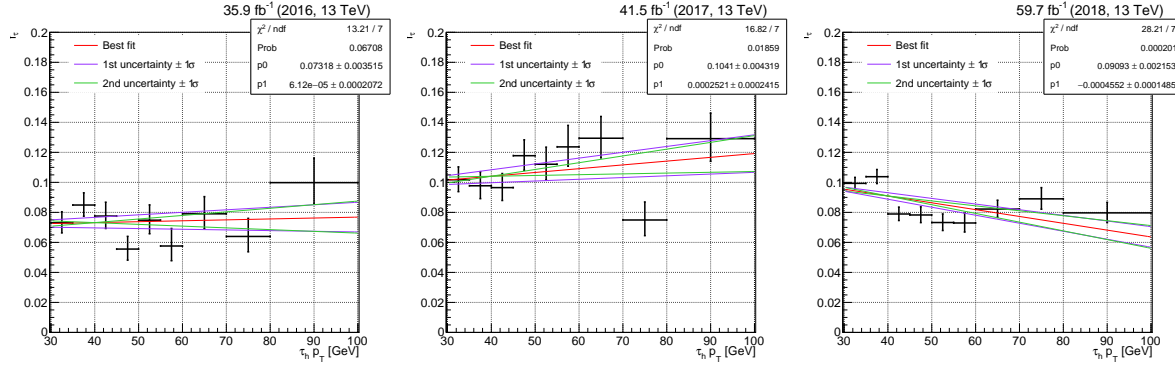


Figure B.14: Fake factors determined in the  $t\bar{t}$  determination region in data in the  $\tau_h$  final state in 2016 (left), 2017 (center), and 2018 (right). They are fitted with linear functions as a function of the  $\tau_h p_T$ . The green and purple lines indicate the shape systematics obtained by uncorrelating the uncertainties in the two fit parameters returned by the fit.

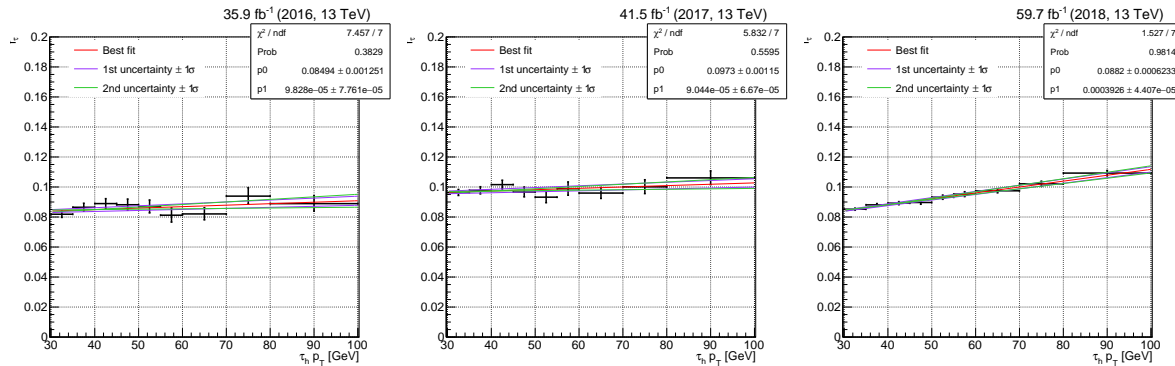


Figure B.15: Fake factors determined in the  $t\bar{t}$  simulation in the  $\tau_h$  final state in 2016 (left), 2017 (center), and 2018 (right). They are fitted with linear functions as a function of the  $\tau_h p_T$ . The green and purple lines indicate the shape systematics obtained by uncorrelating the uncertainties in the two fit parameters returned by the fit.

## Appendix C

# Systematic Uncertainties

Below are the rest of the channels and years from the systematic uncertainty discussion similar to mmmmt 2017 result shown in the main part of the paper 7.9.

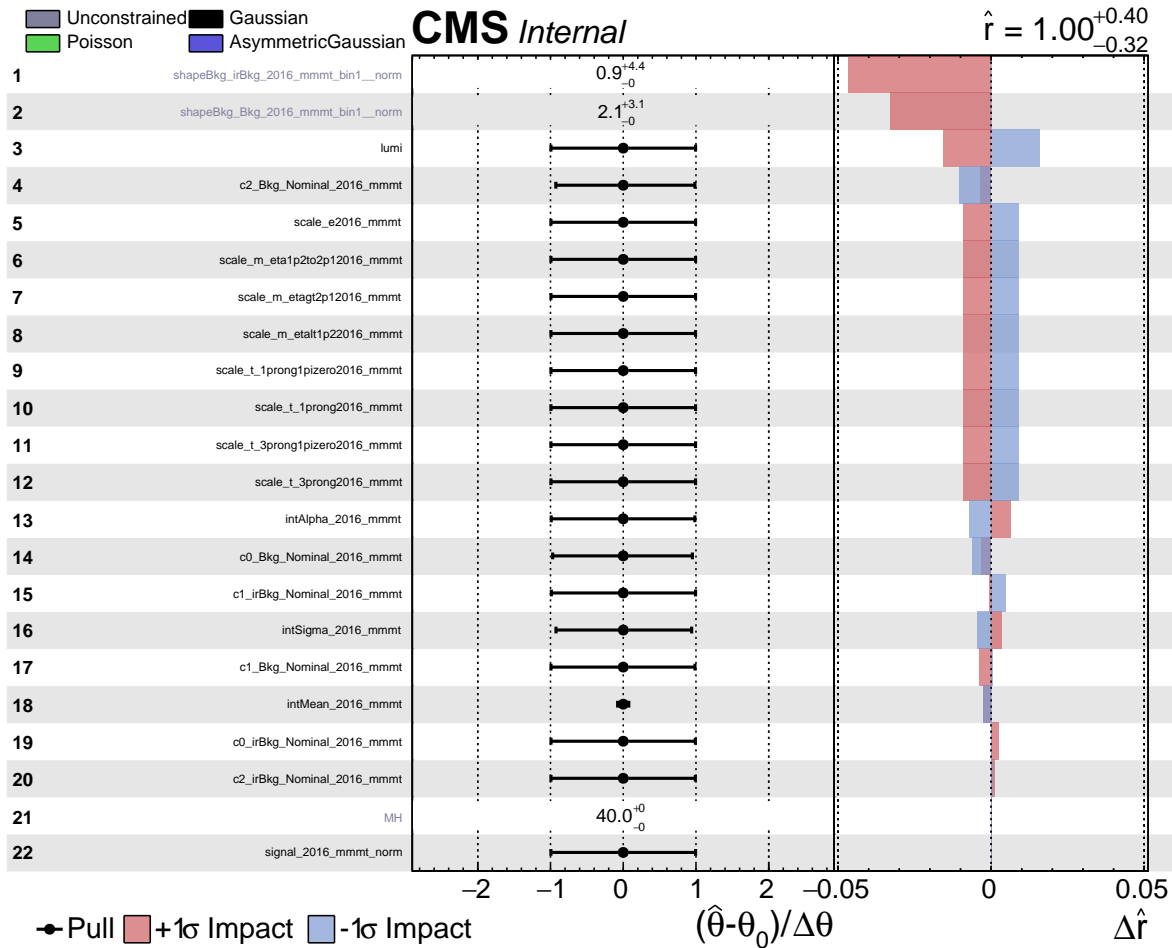


Figure C.1: Expected systematic impacts for the fit model  $\mu\mu\mu\tau$

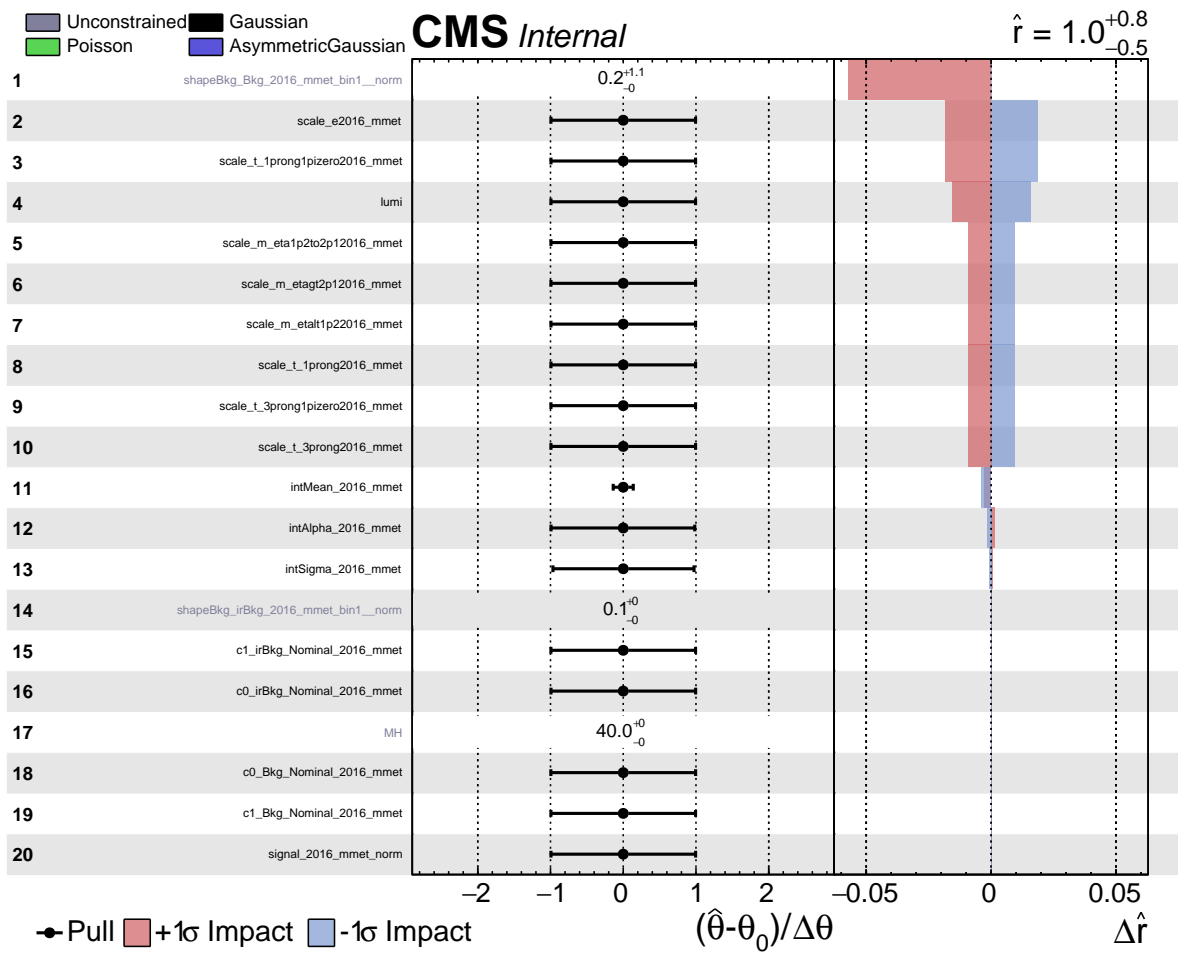


Figure C.2: Expected systematic impacts for the fit model  $\mu\mu e\tau$

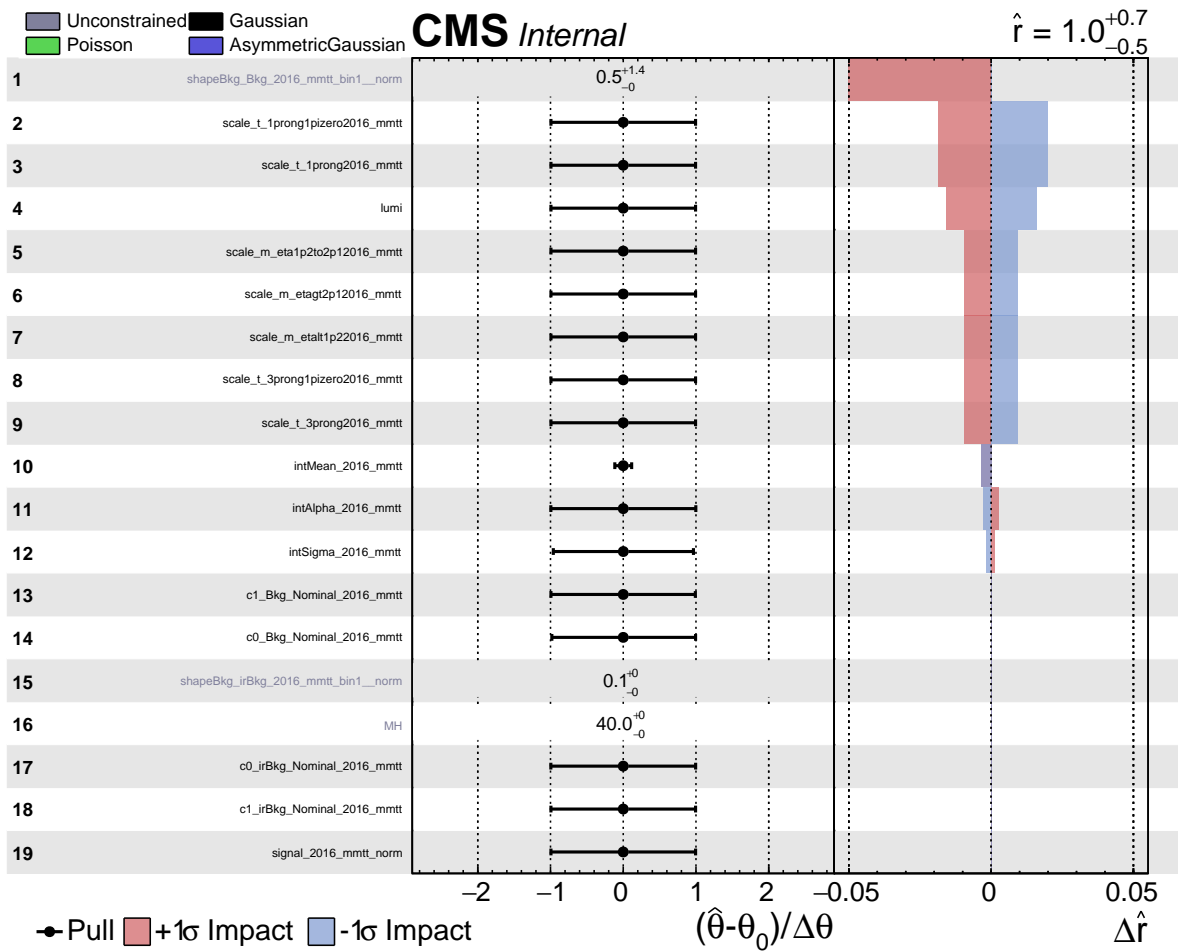


Figure C.3: Expected systematic impacts for the fit model for 2016  $\mu\mu\tau\tau$

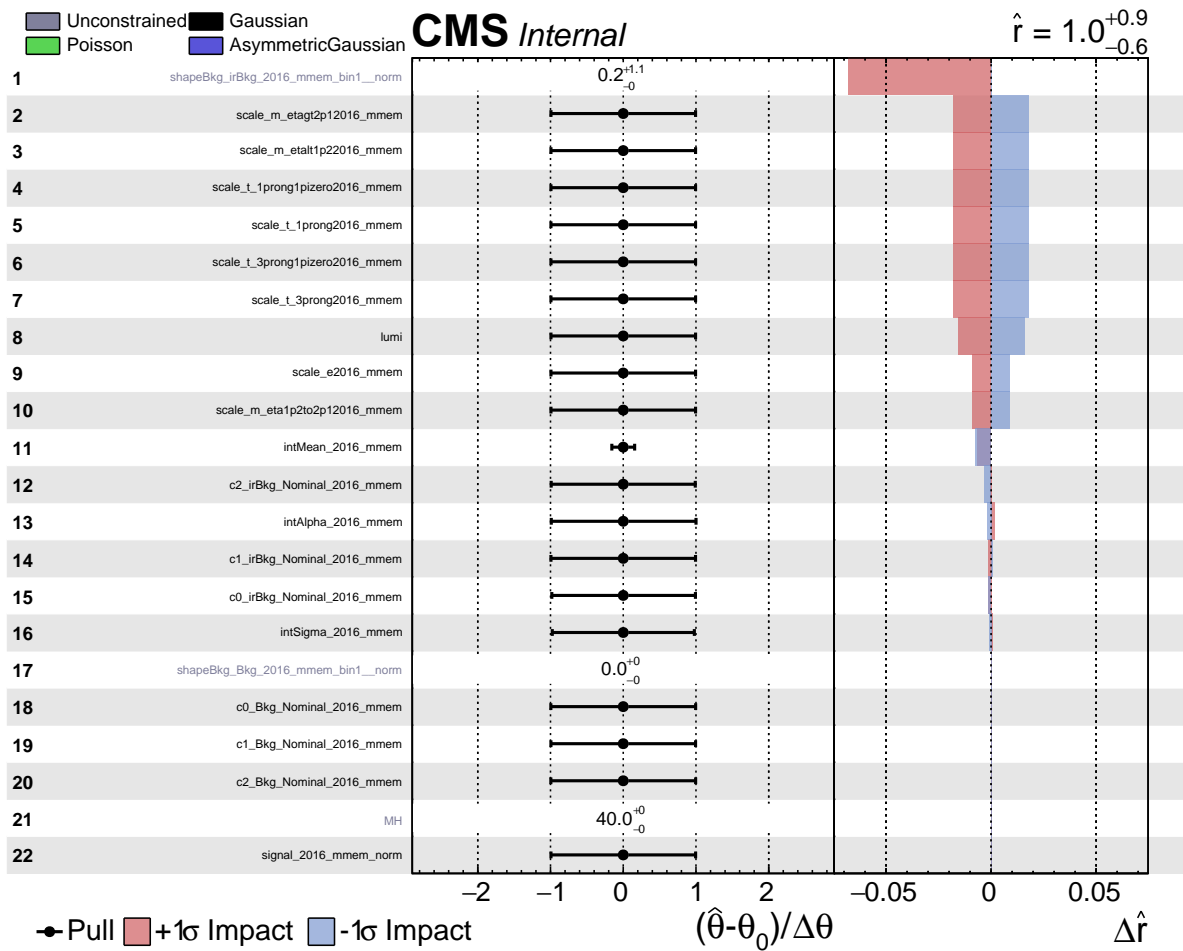
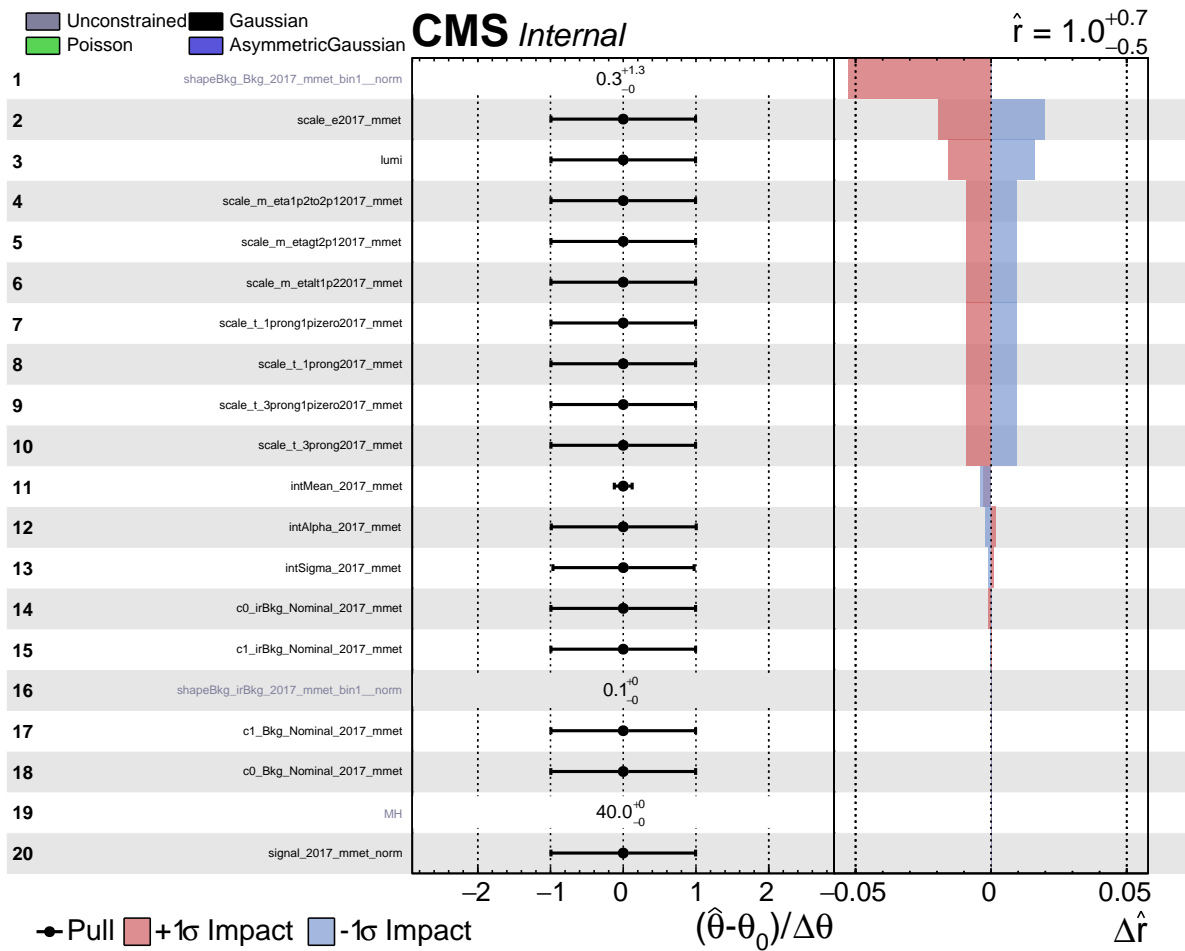


Figure C.4: Expected systematic impacts for the fit model for 2016  $\mu\mu e\mu$

Figure C.5: Expected systematic impacts for the fit model  $\mu\mu e\tau$

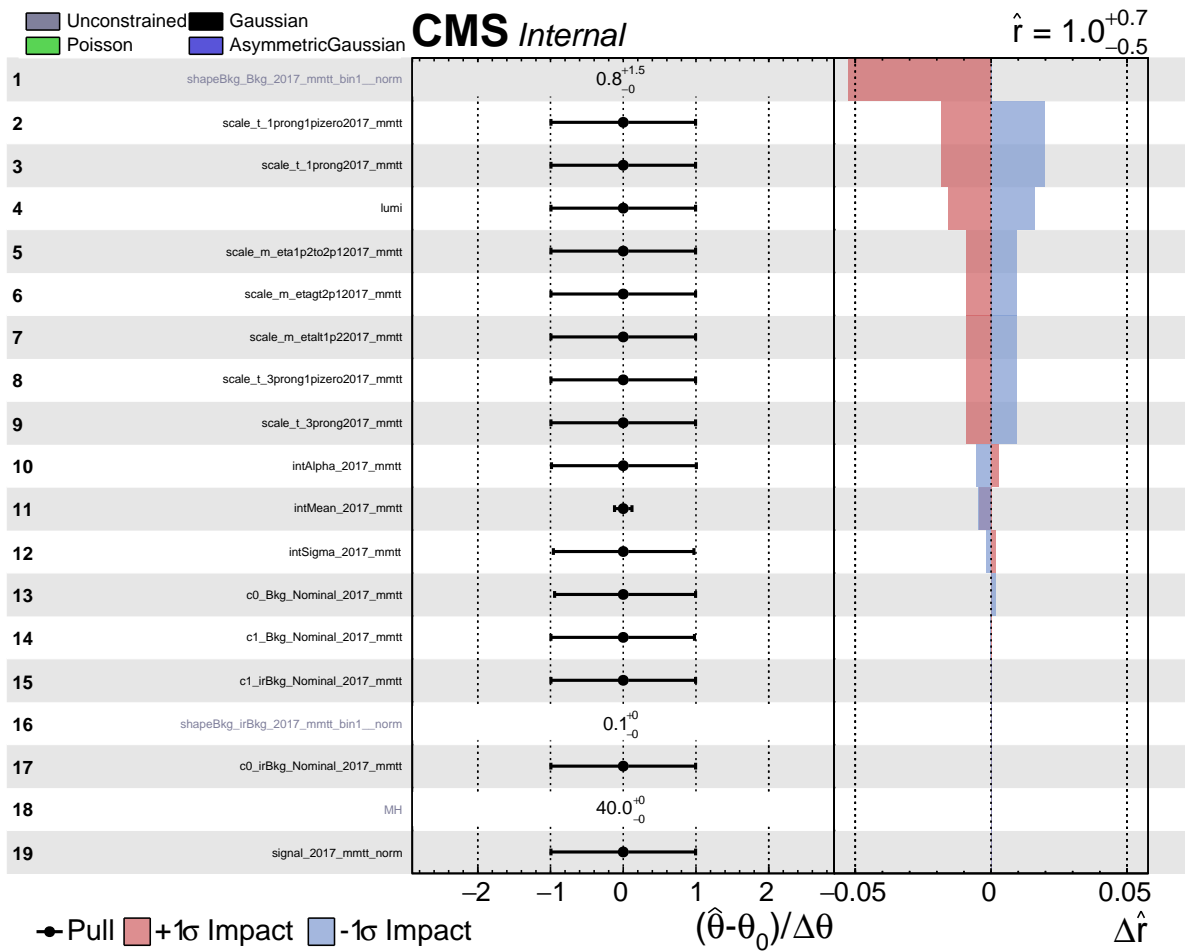


Figure C.6: Expected systematic impacts for the fit model for 2017  $\mu\mu\tau\tau$

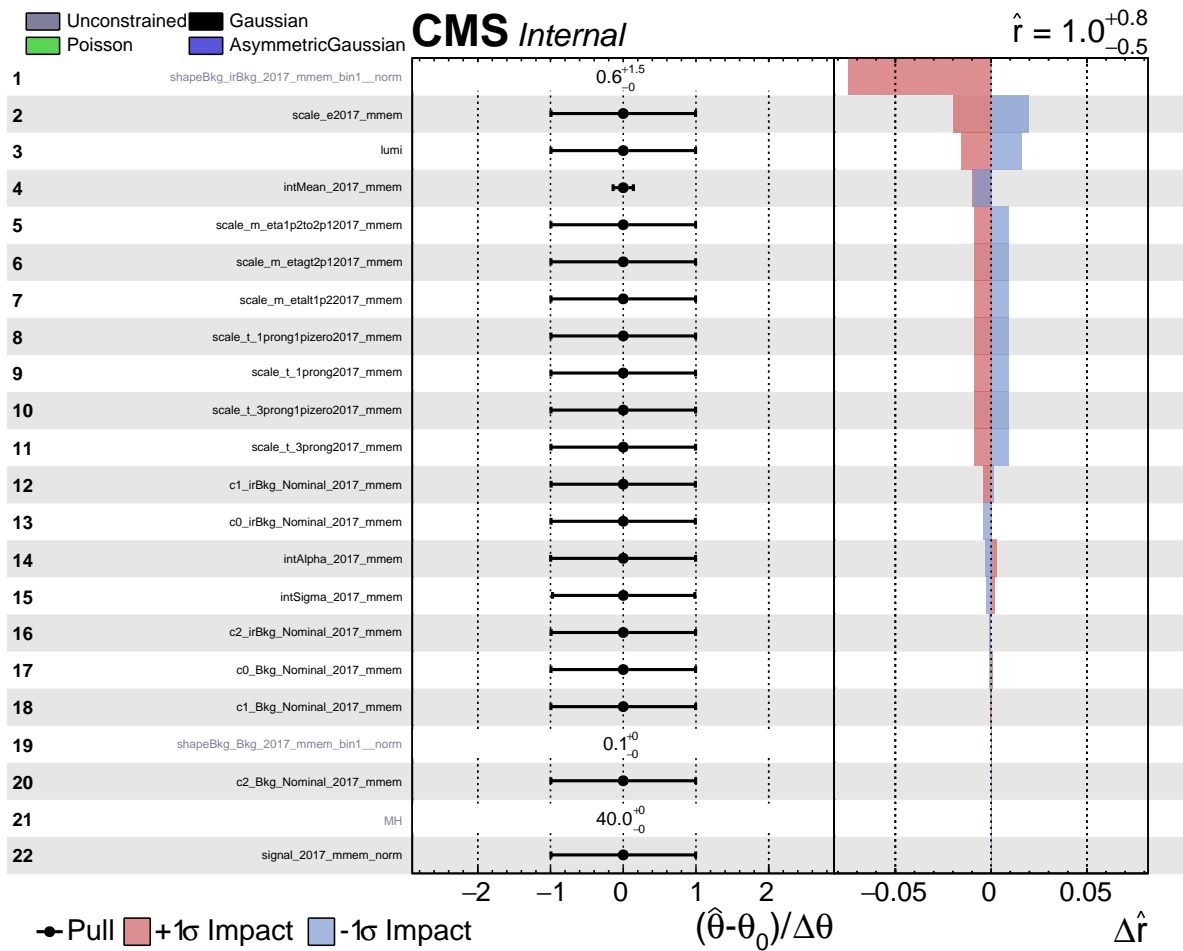


Figure C.7: Expected systematic impacts for the fit model for 2017  $\mu\mu e\mu$

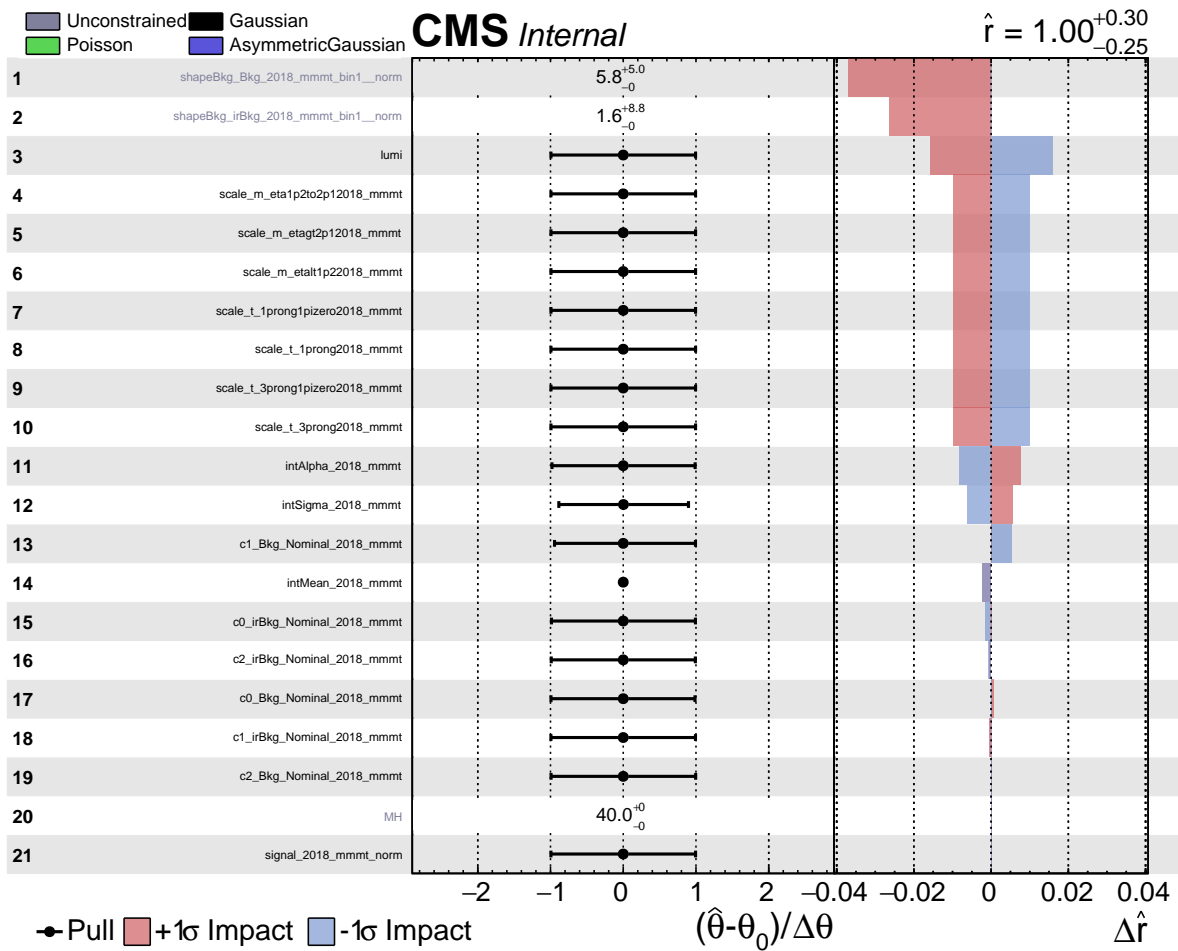
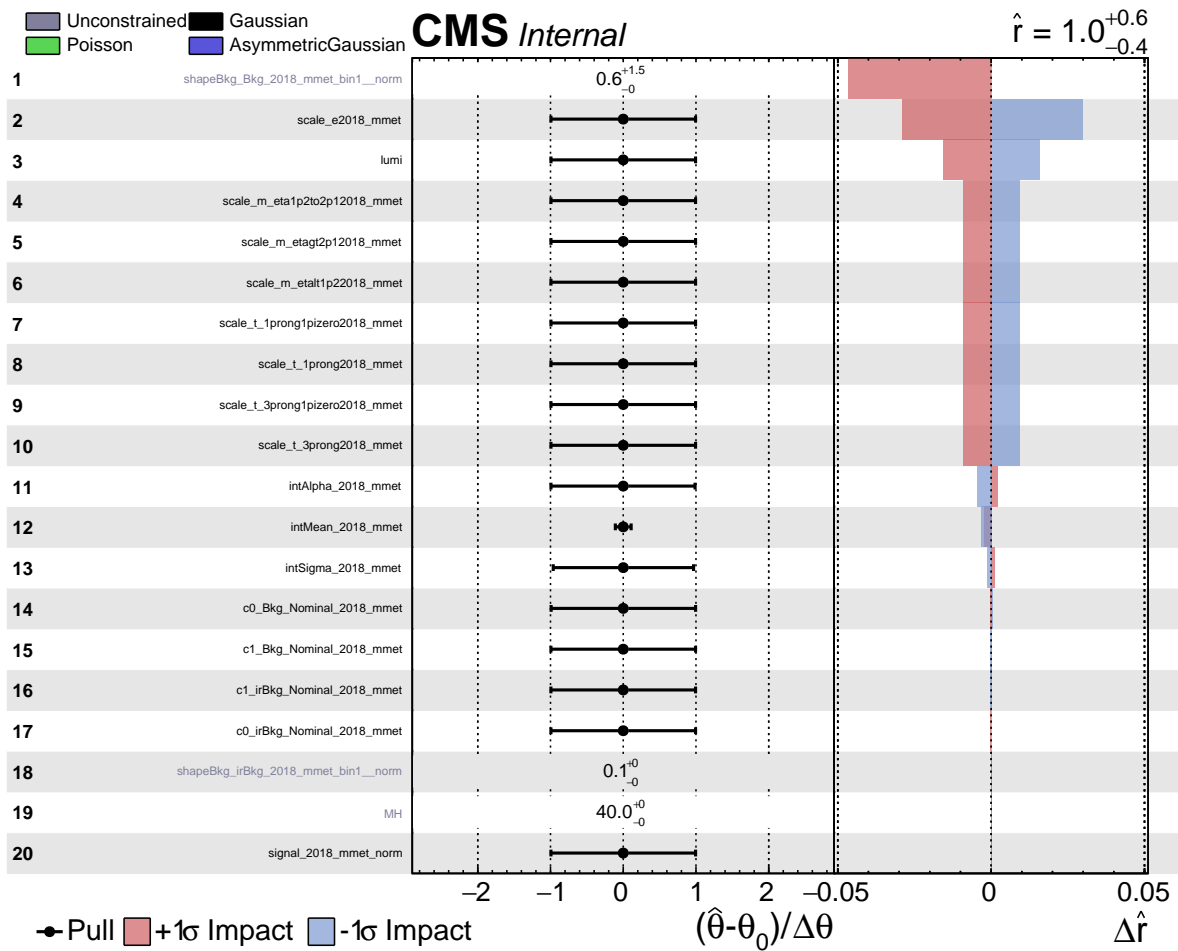


Figure C.8: Expected systematic impacts for the fit model  $\mu\mu\mu\tau$

Figure C.9: Expected systematic impacts for the fit model  $\mu\mu e\tau$

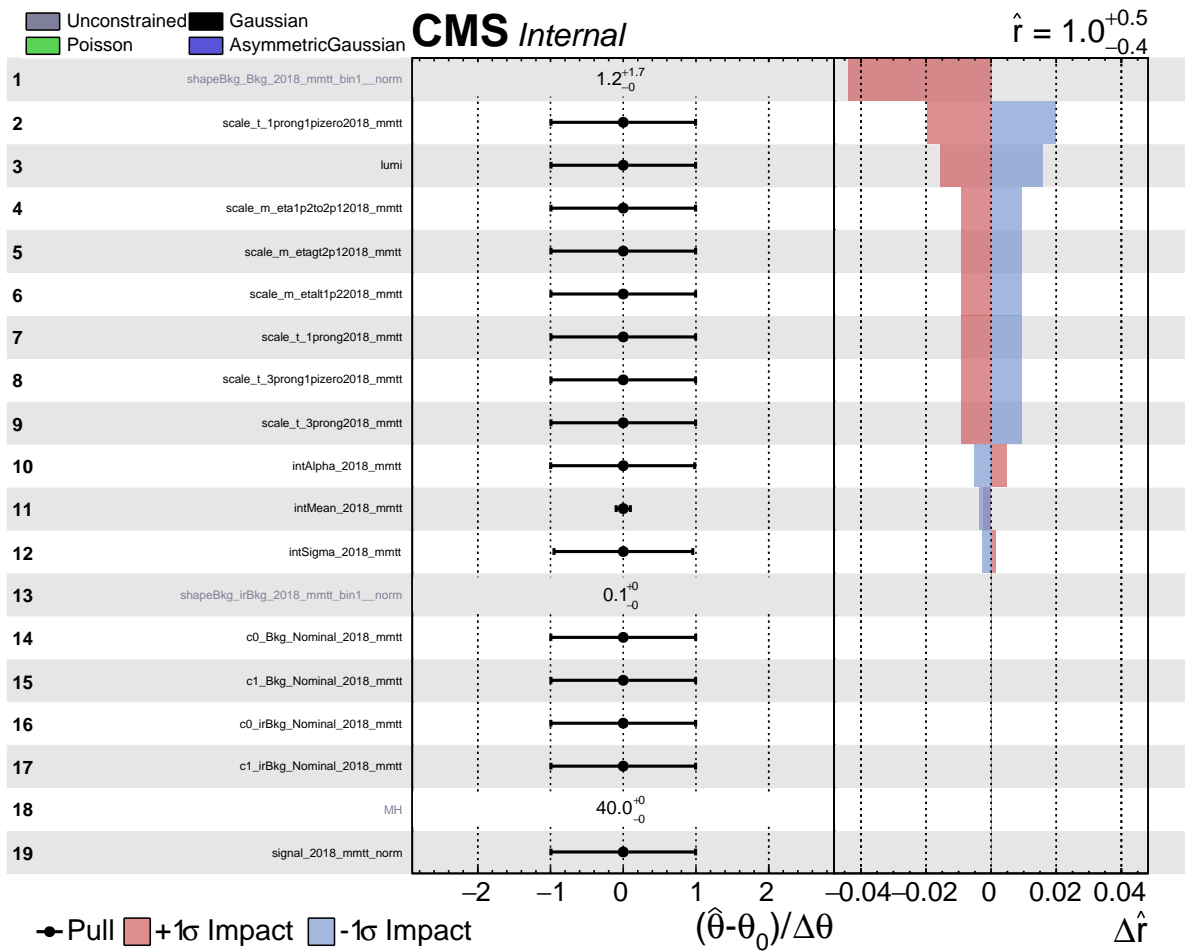


Figure C.10: Expected systematic impacts for the fit model for 2018  $\mu\mu\tau\tau$

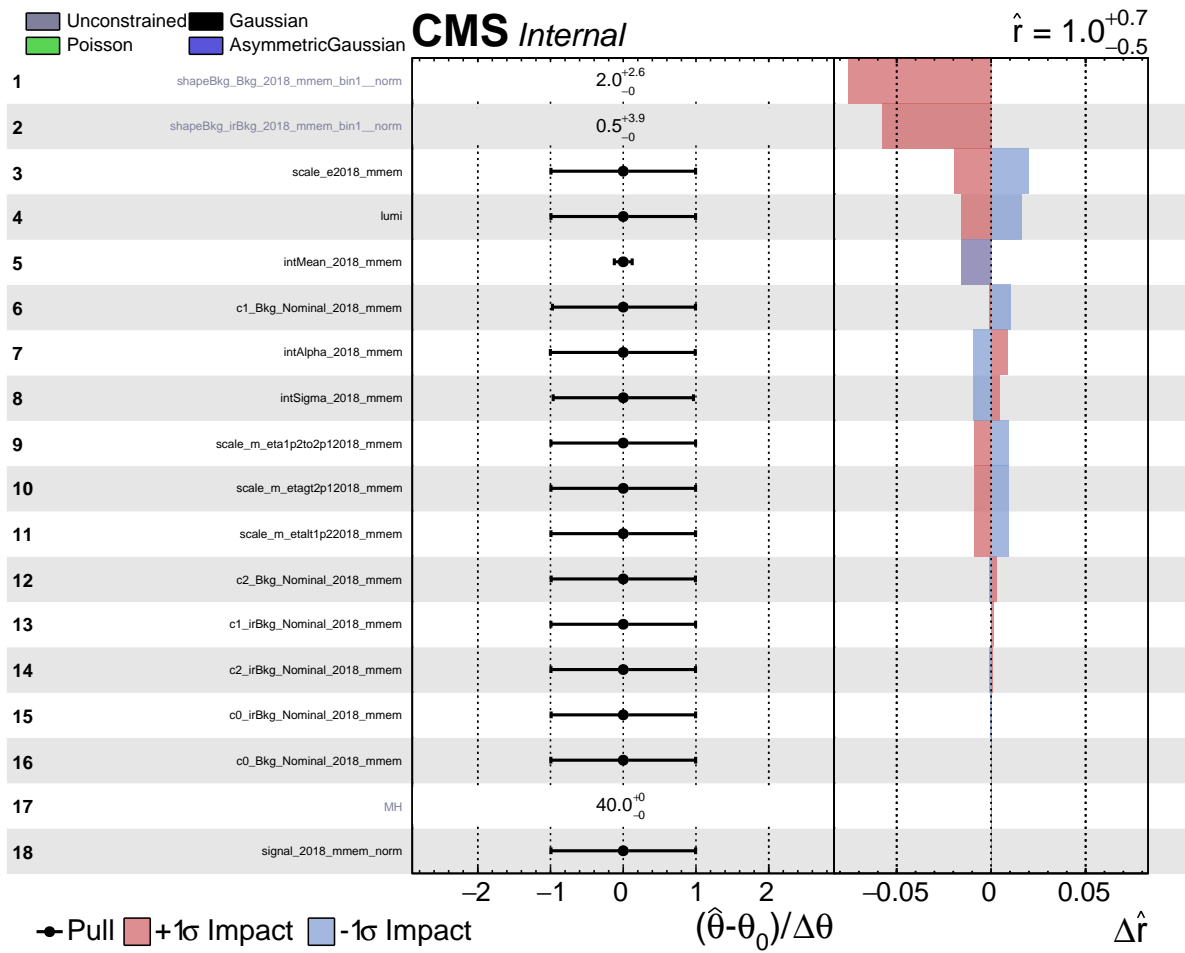


Figure C.11: Expected systematic impacts for the fit model for 2018  $\mu\mu e\mu$

## **Appendix D**

## **Fit Models**

This section contains the remaining parametric fit models for the rest of the years 2017, 2018 and the channels referenced originally in chapter 7.

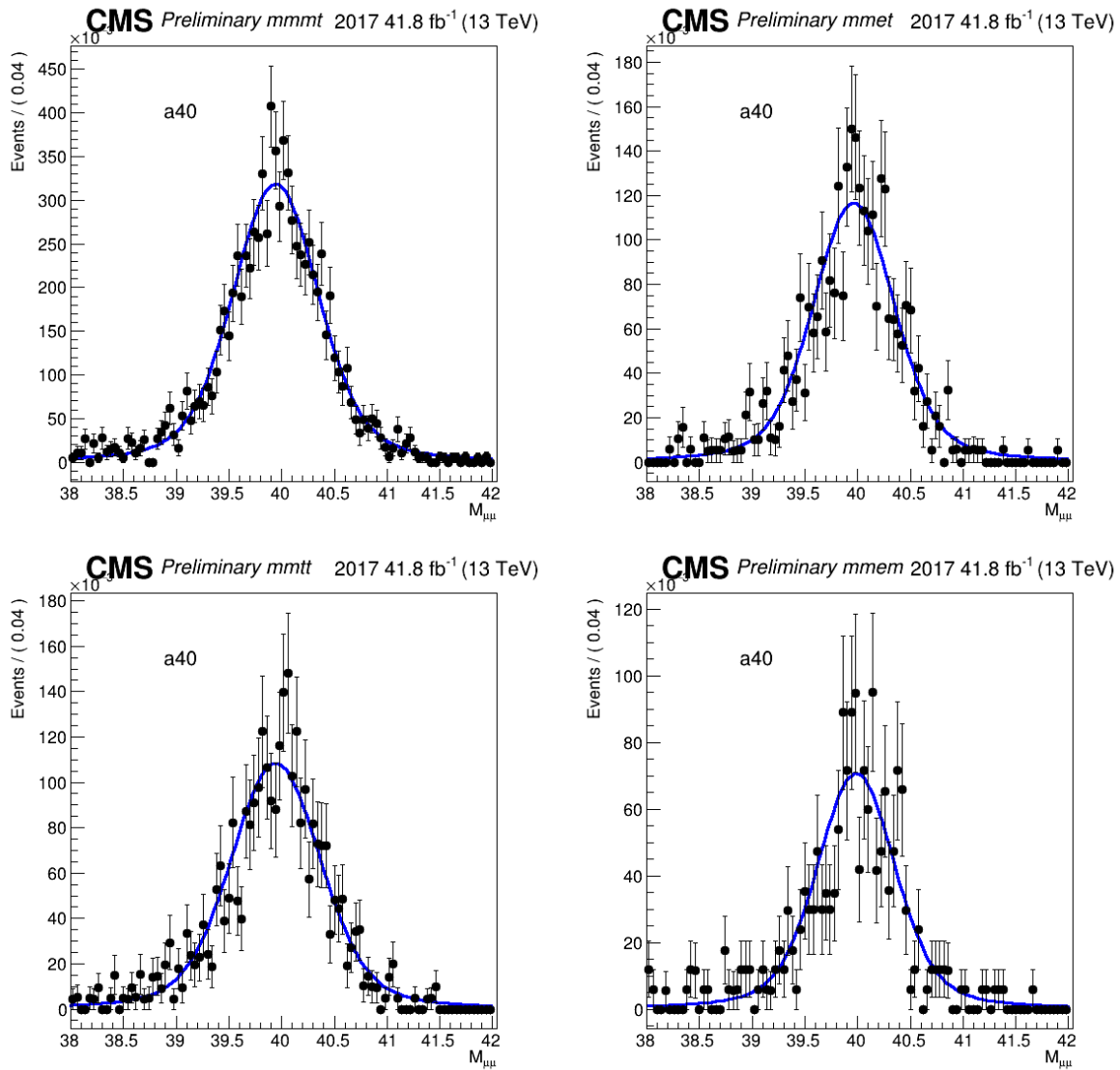


Figure D.1: 2017 Signal fit using a Voigtian function

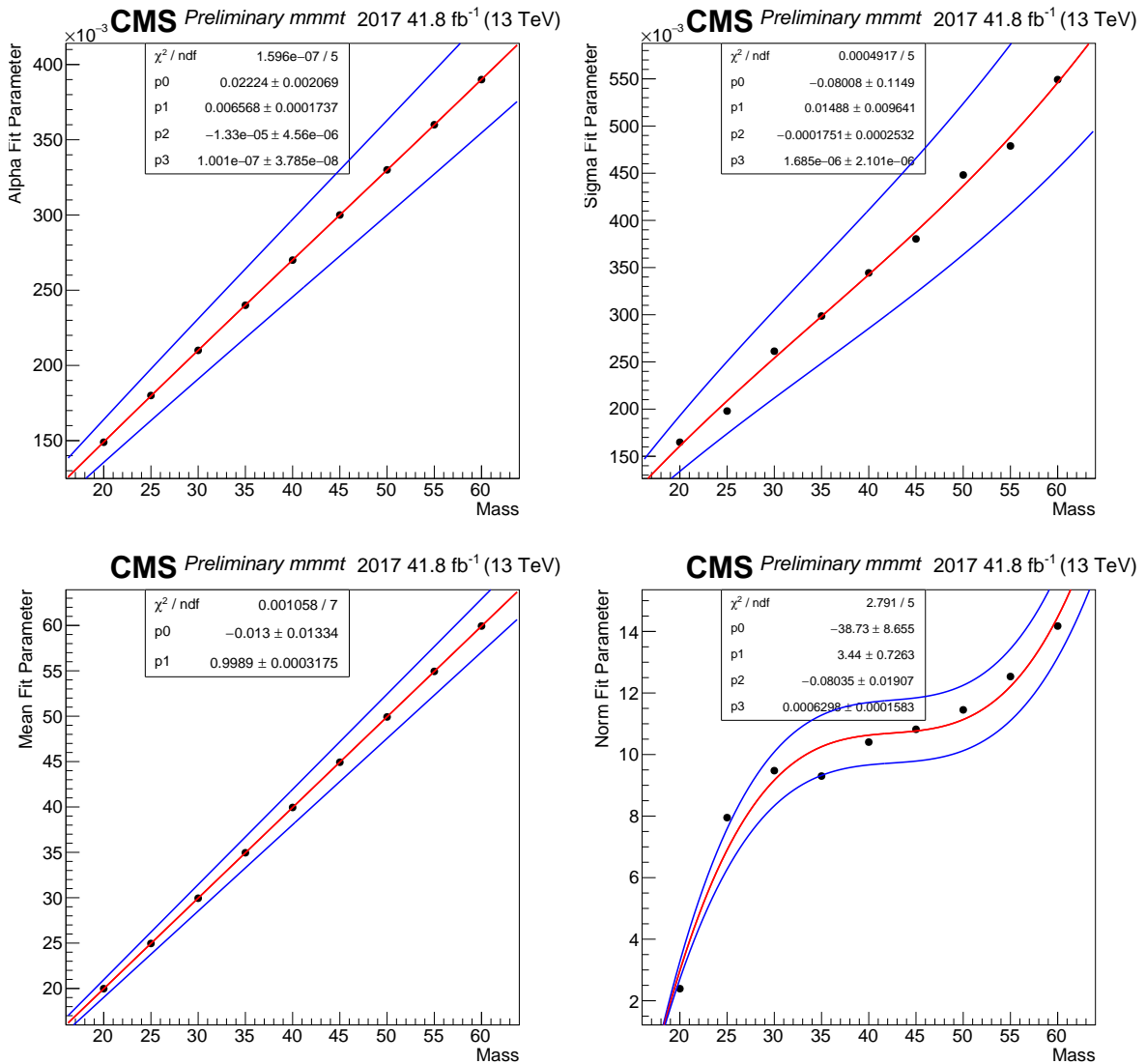


Figure D.2: Spline functions for 2017 mmmt a 3rd order polynomial is used for for Alpha, Sigma, and Normalization, a 1st order polynomial is used for the Mean

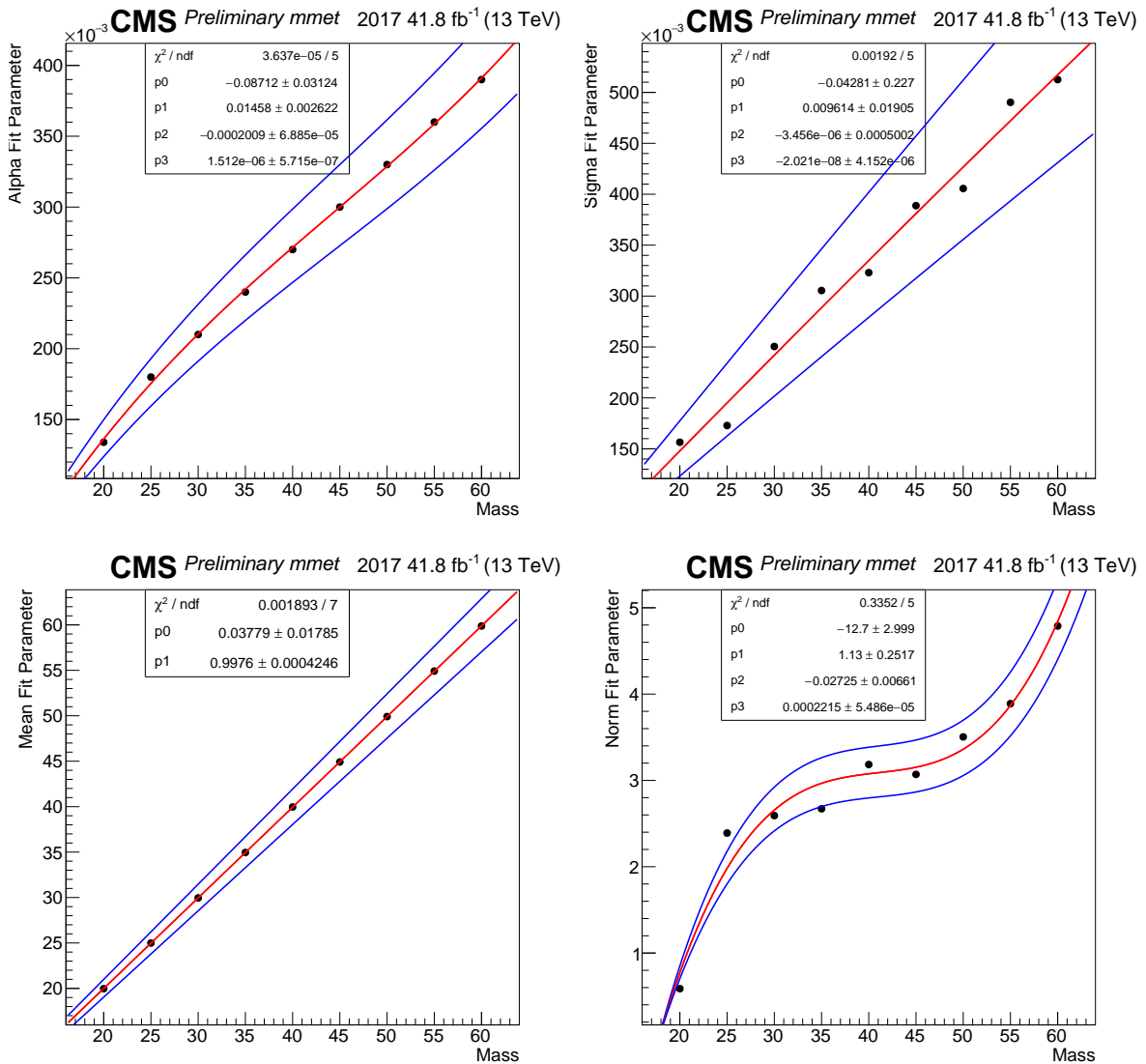


Figure D.3: Spline functions for 2017 mmet a 3rd order polynomial is used for for Alpha, Sigma, and Normalization, a 1st order polynomial is used for the Mean

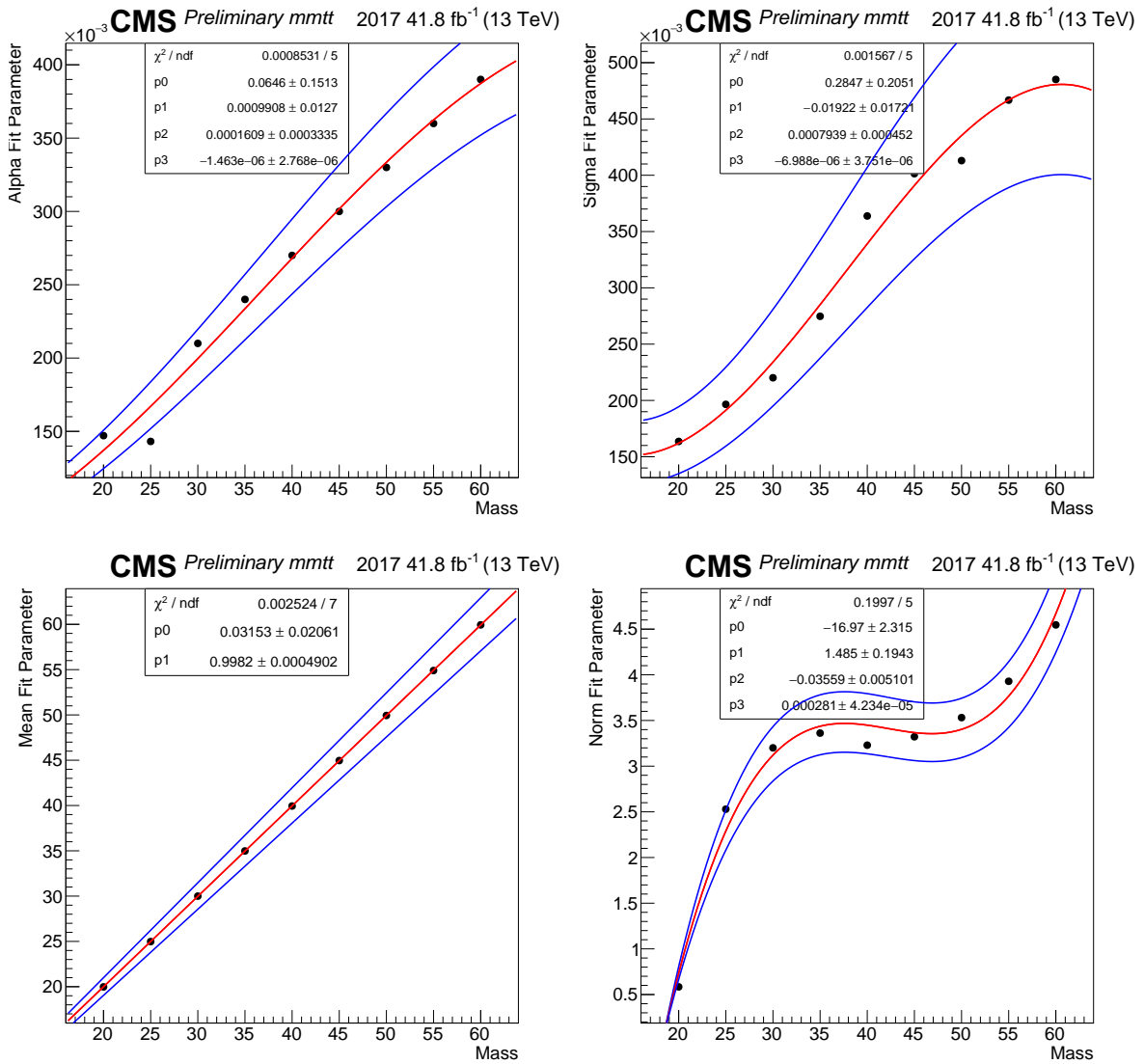


Figure D.4: Spline functions for 2017 mm $t\bar{t}$  a 3rd order polynomial is used for for Alpha, Sigma, and Normalization, a 1st order polynomial is used for the Mean

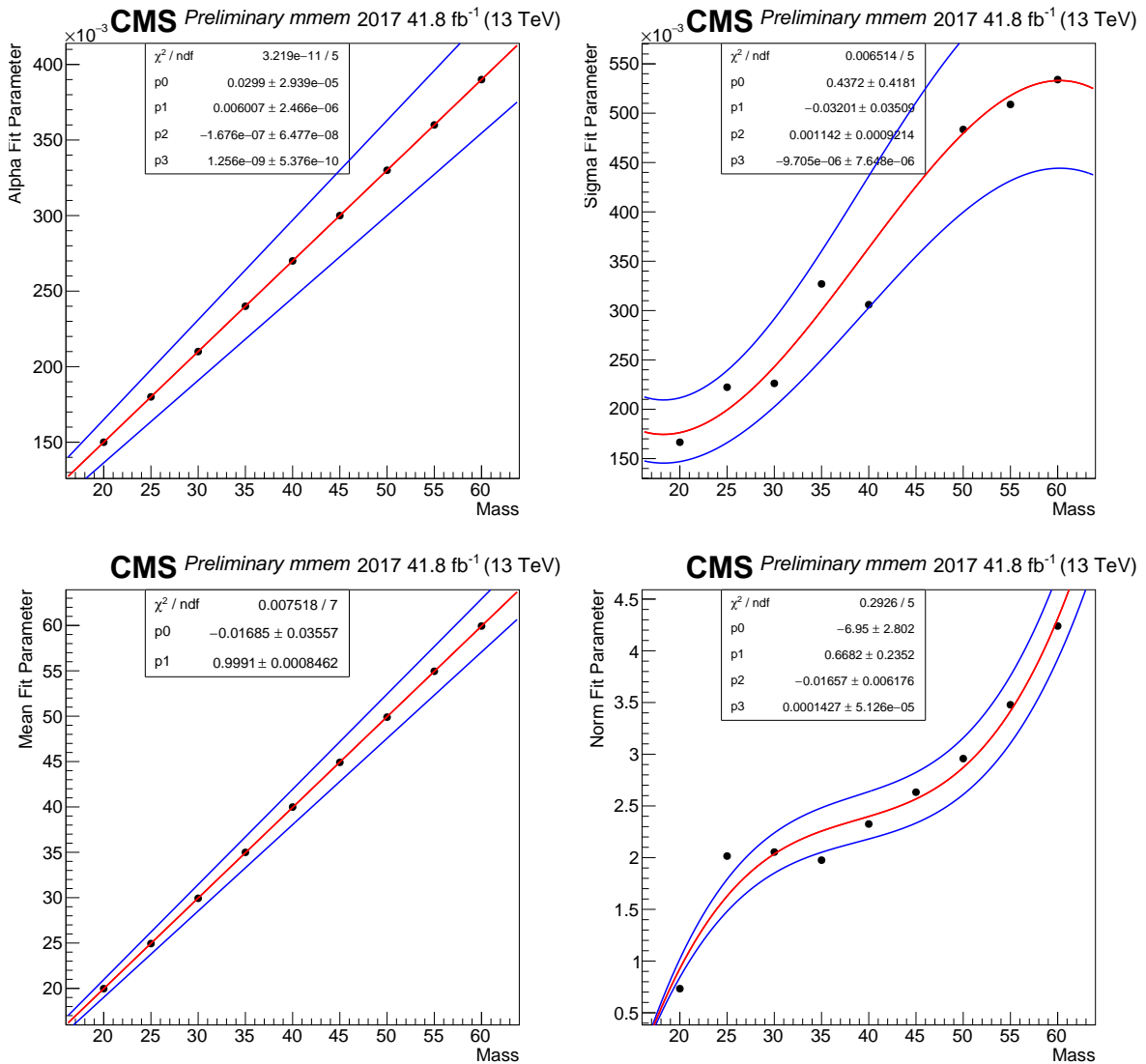


Figure D.5: Spline functions for 2017 mmem a 3rd order polynomial is used for for Alpha, Sigma, and Normalization, a 1st order polynomial is used for the Mean

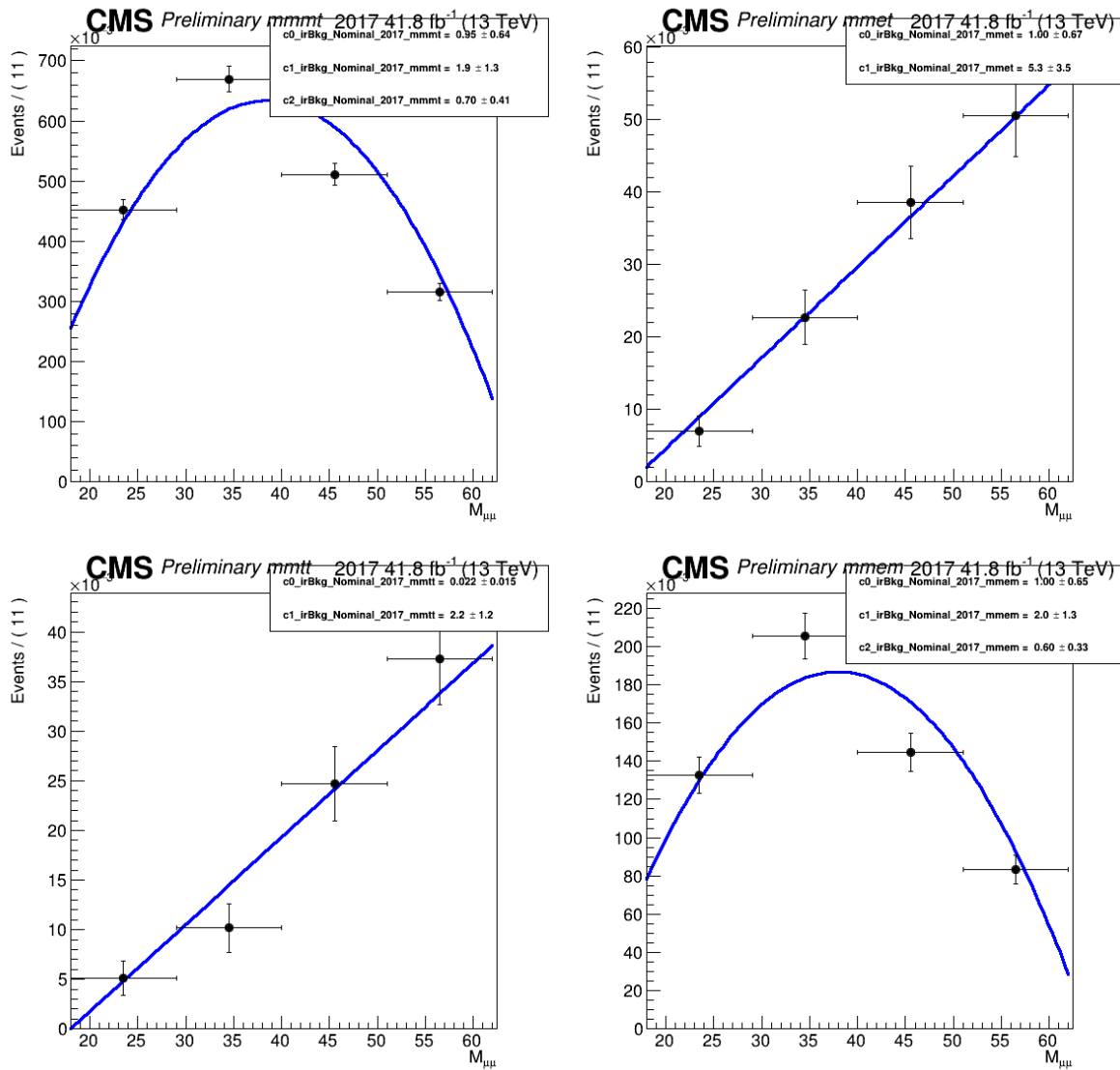


Figure D.6: 2017 irreducible background fit using Bernstein polynomials

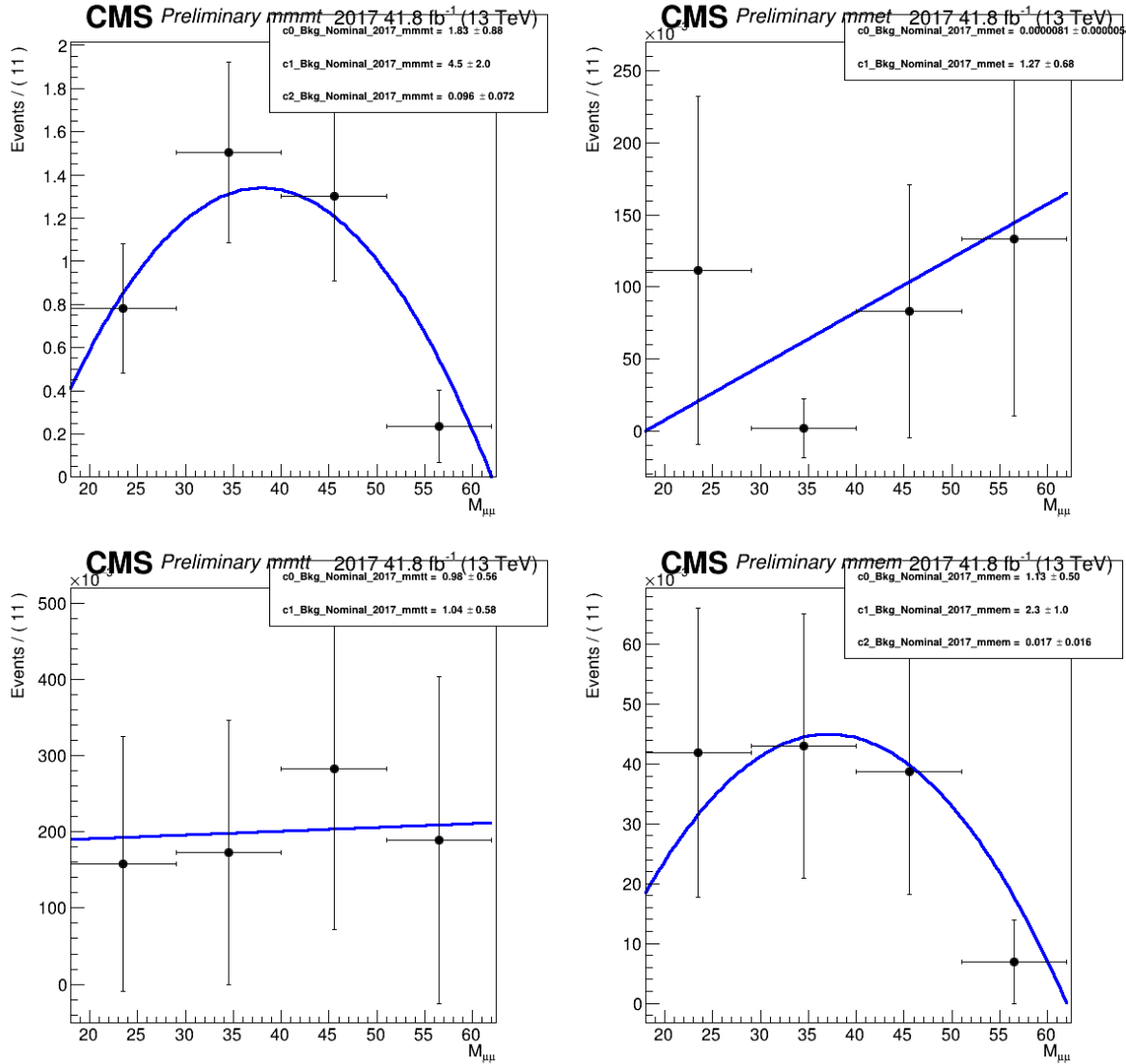


Figure D.7: 2017 reducible background fit using Bernstein polynomials

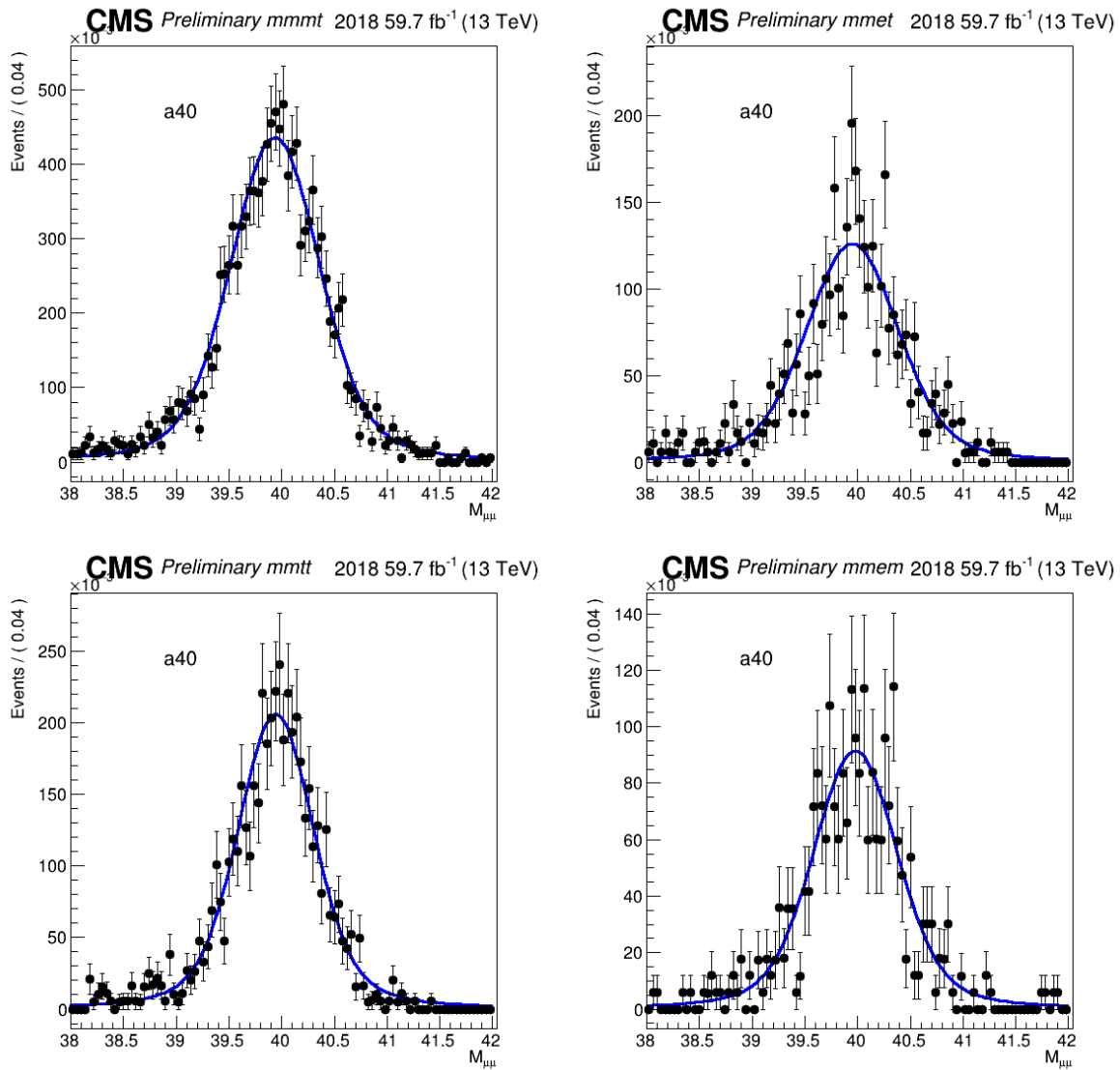


Figure D.8: 2018 Signal fit using a Voigtian function

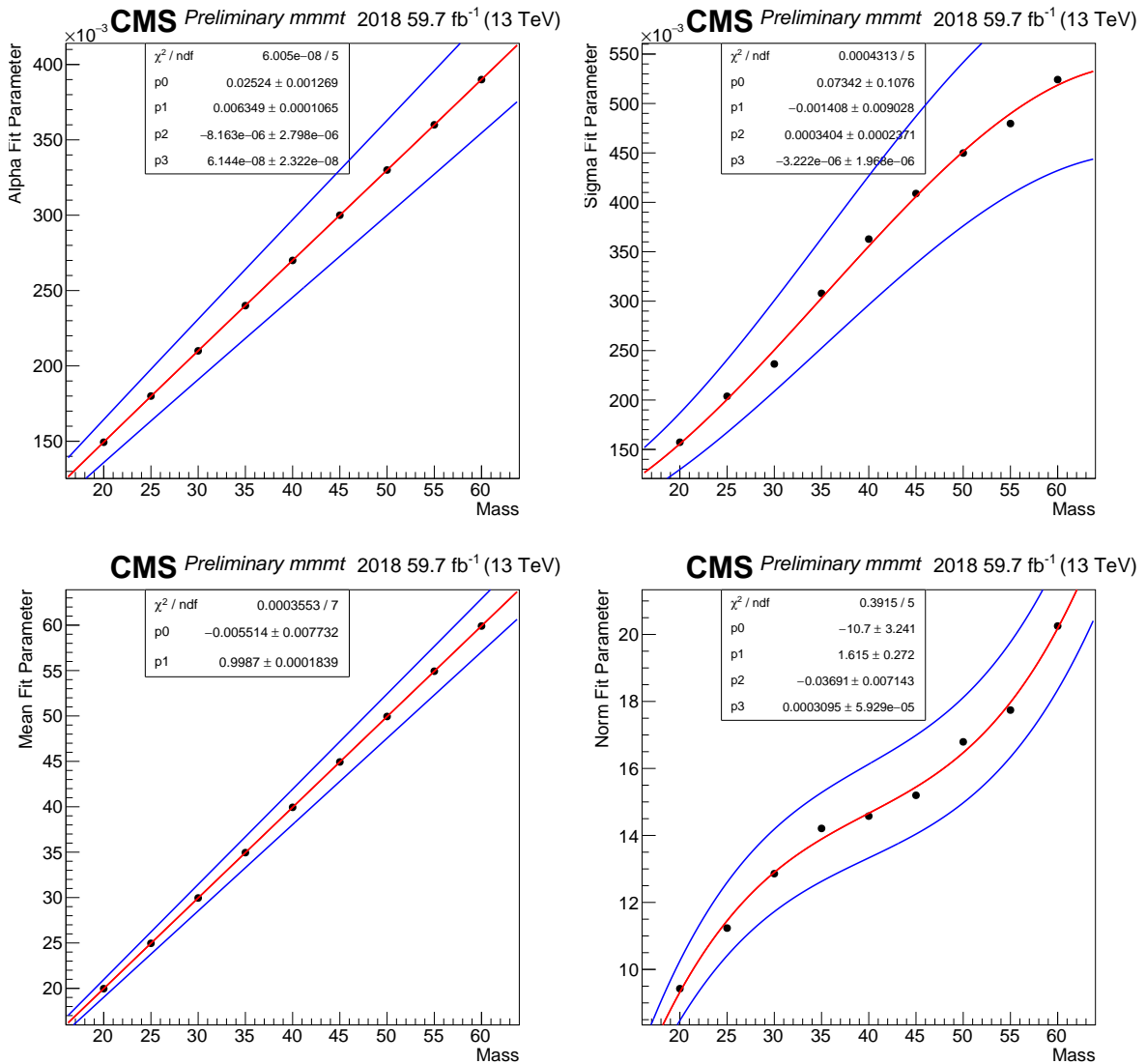


Figure D.9: Spline functions for 2018 mmmt a 3rd order polynomial is used for for Alpha, Sigma, and Normalization, a 1st order polynomial is used for the Mean

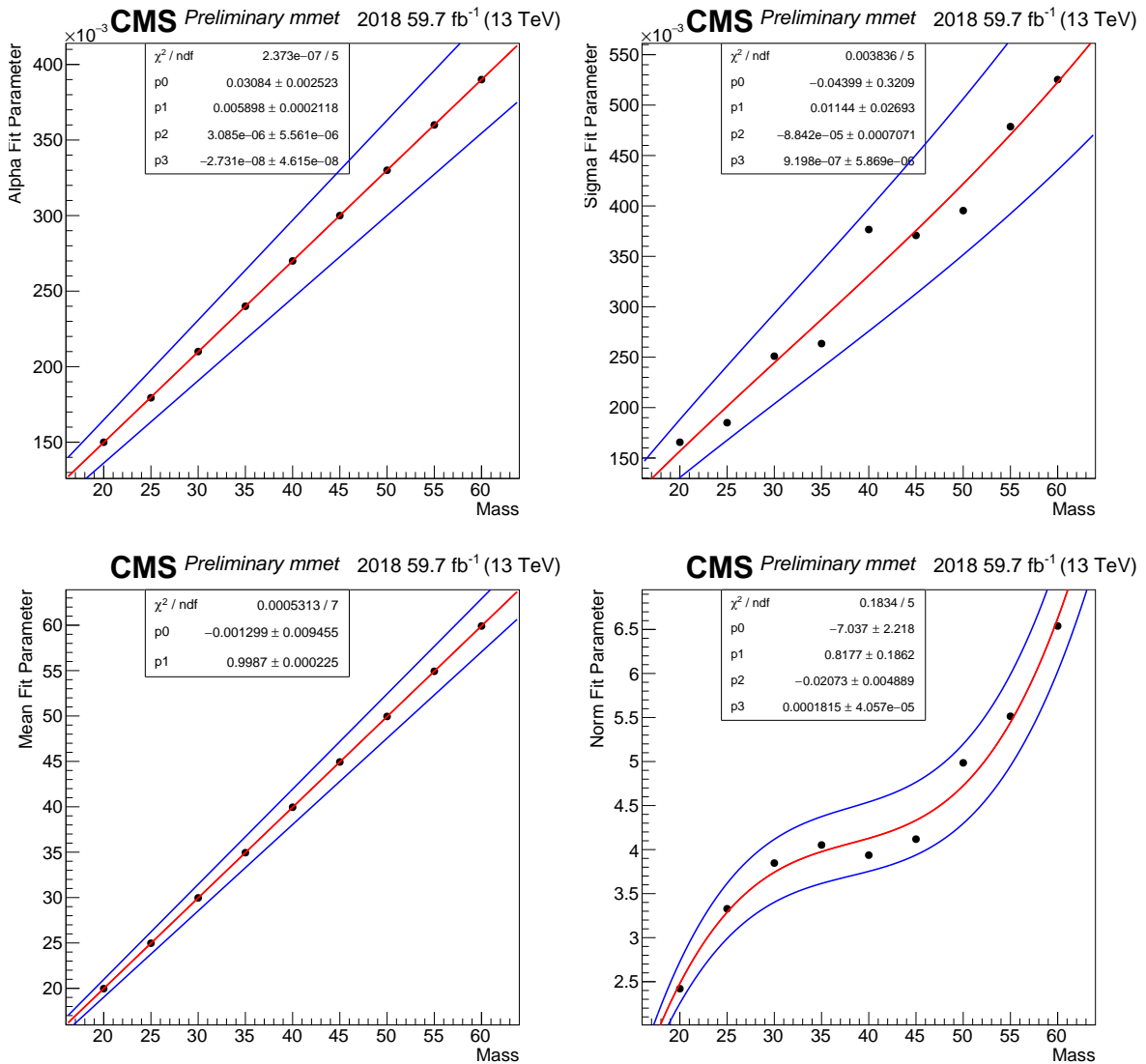


Figure D.10: Spline functions for 2018 mmet a 3rd order polynomial is used for for Alpha, Sigma, and Normalization, a 1st order polynomial is used for the Mean

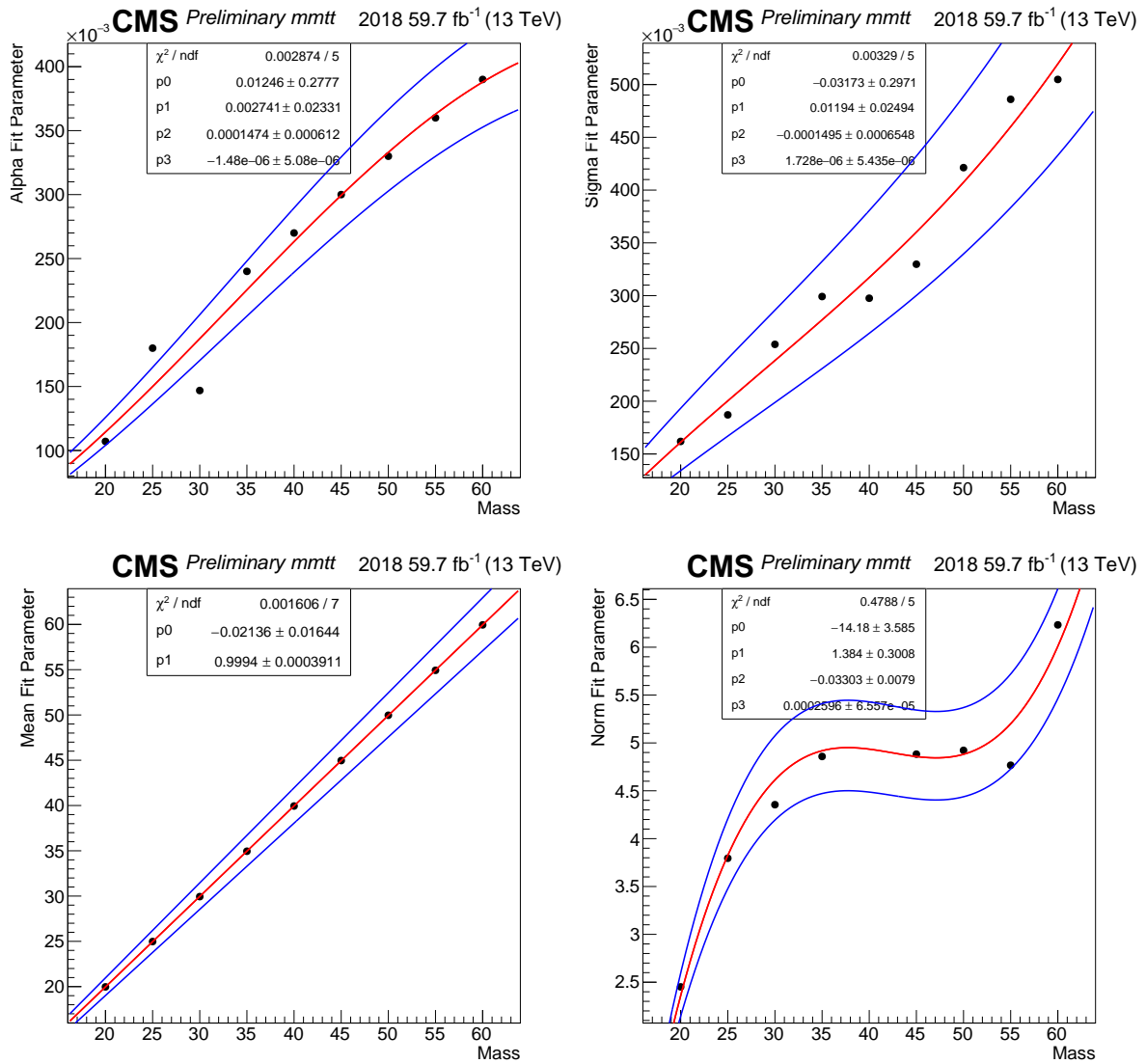


Figure D.11: Spline functions for 2018 mmtt a 3rd order polynomial is used for for Alpha, Sigma, and Normalization, a 1st order polynomial is used for the Mean

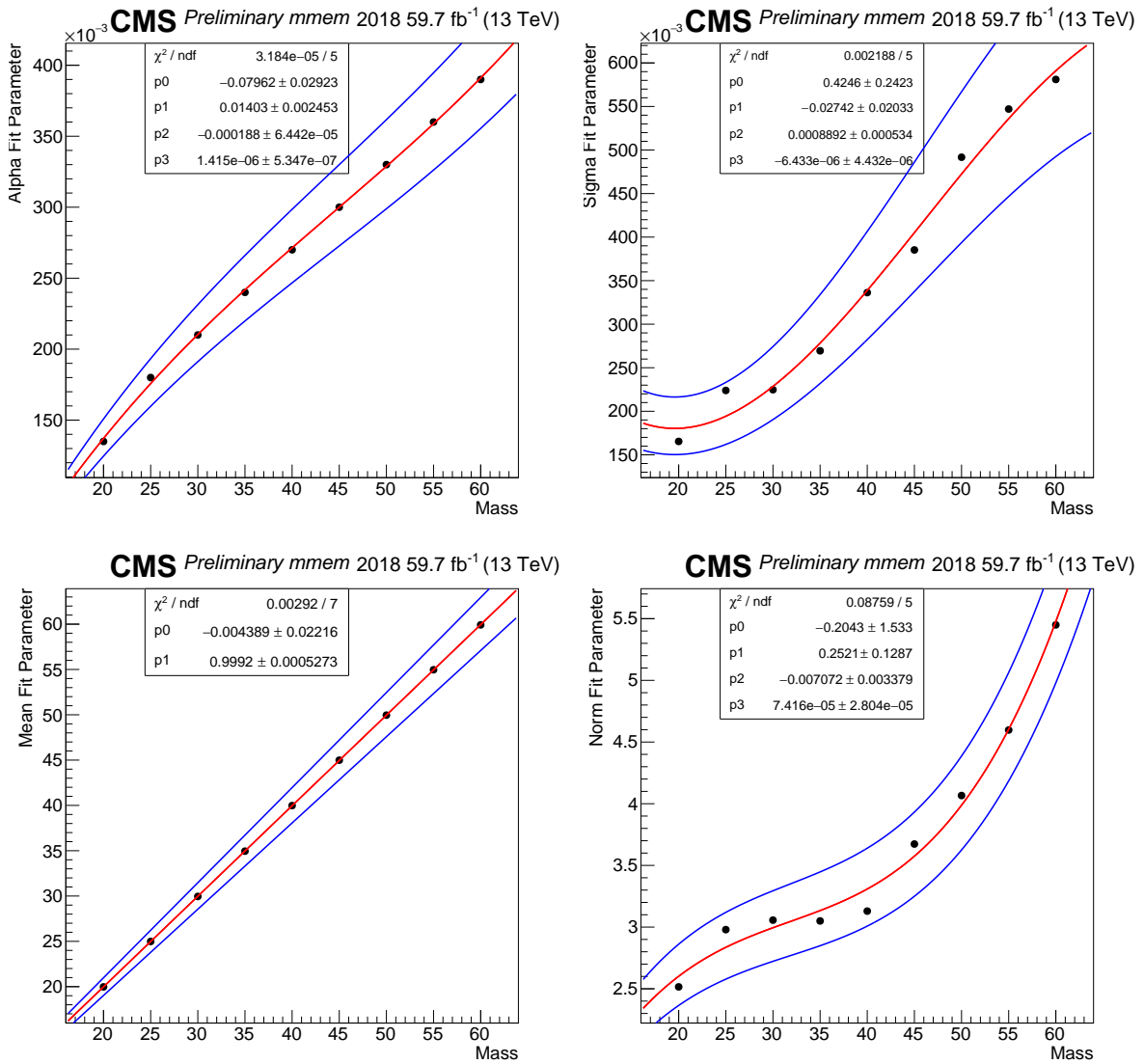


Figure D.12: Spline functions for 2018 mmem a 3rd order polynomial is used for for Alpha, Sigma, and Normalization, a 1st order polynomial is used for the Mean

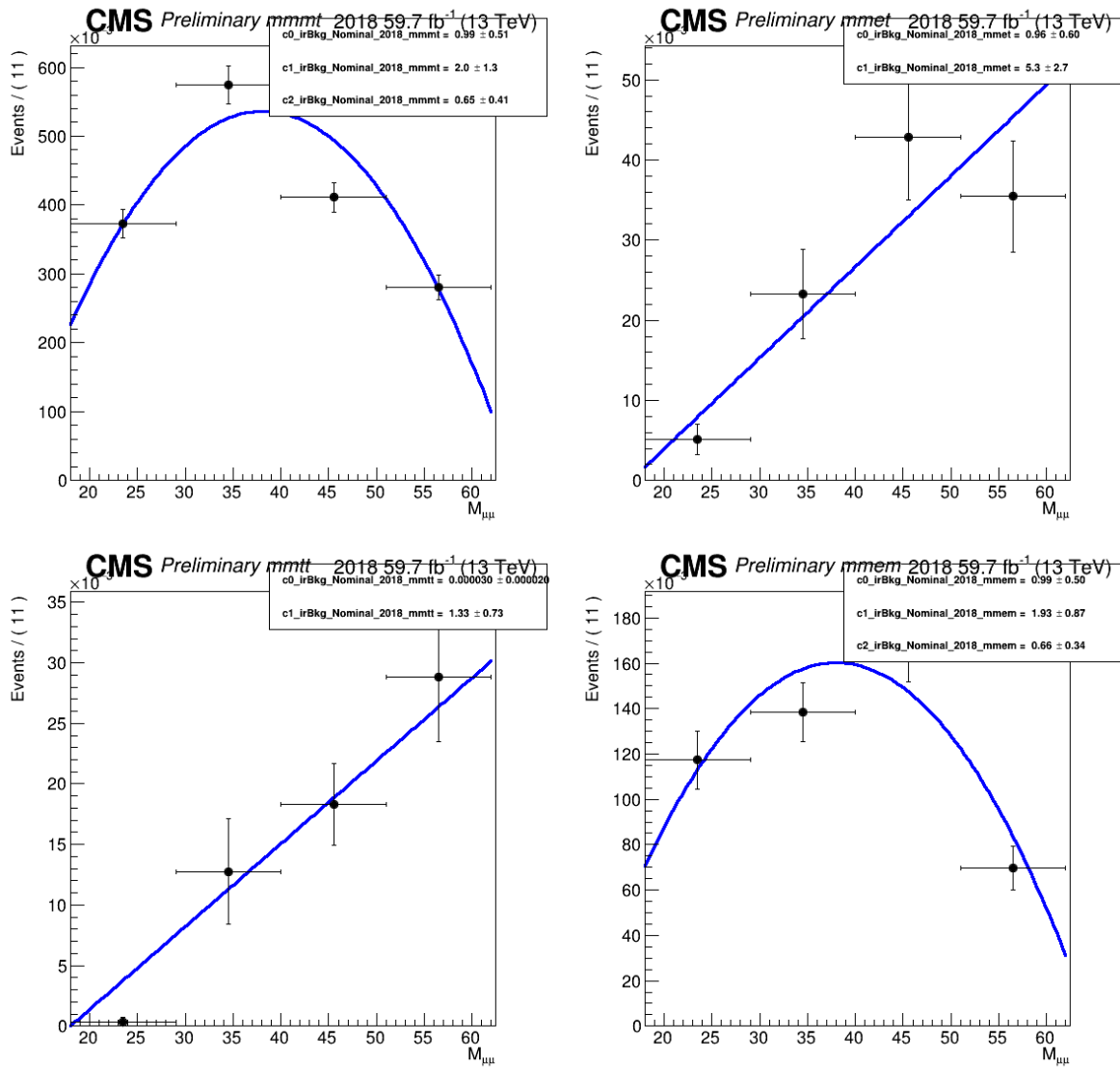


Figure D.13: 2018 irreducible background fit using Bernstein polynomials

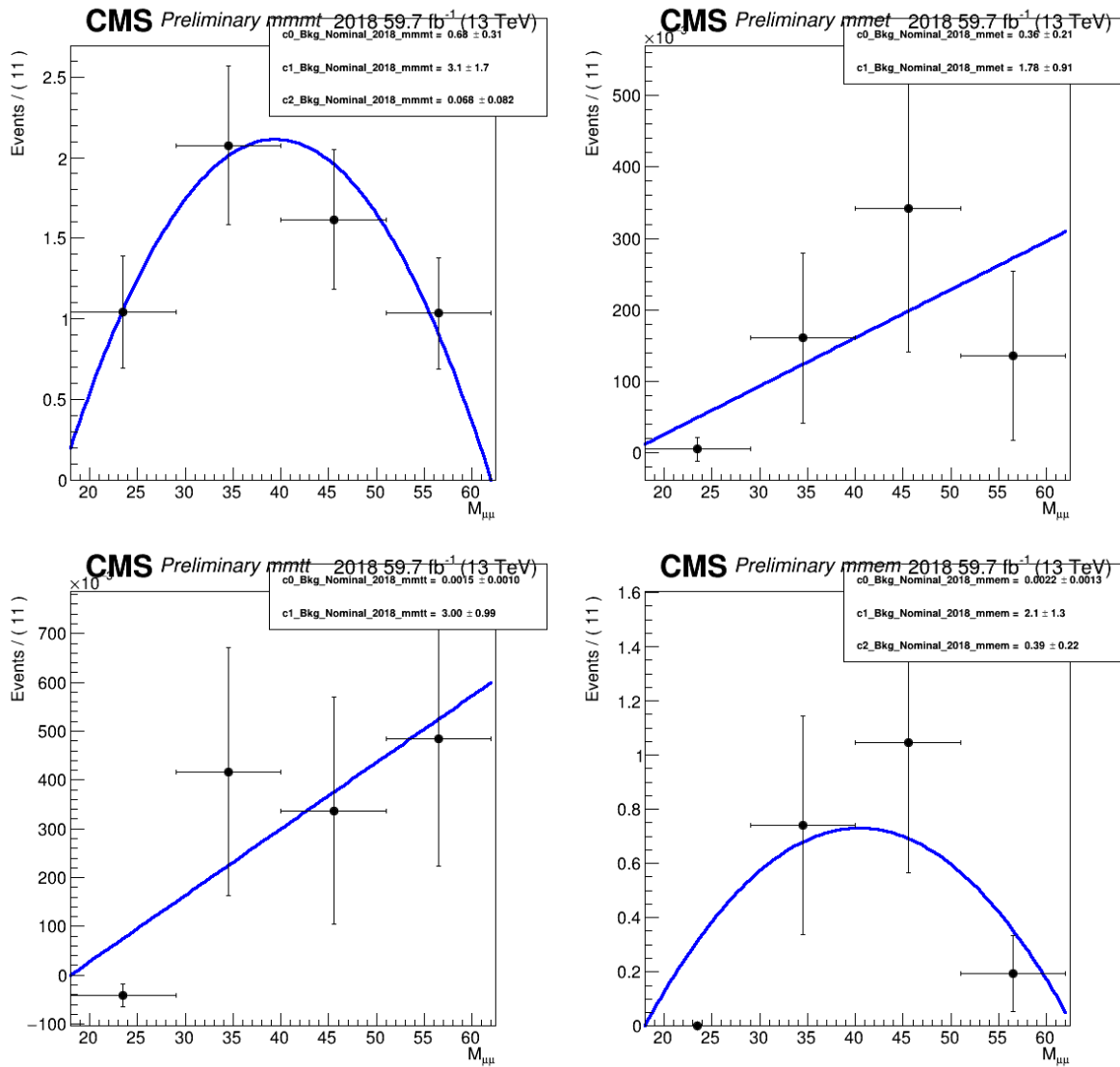


Figure D.14: 2018 reducible background fit using Bernstein polynomials

# References

- [1] E. Noether, “Invariant variation problems,” *Transport Theory and Statistical Physics*, vol. 1, pp. 186–207, jan 1971.
- [2] C. G. Tully, *Elementary particle physics in a nutshell*. Princeton, NJ: Princeton Univ. Press, 2011.
- [3] T. Lancaster and S. J. Blundell, *Quantum field theory for the gifted amateur*. Oxford: Oxford University Press, Apr 2014.
- [4] G. Branco, P. Ferreira, L. Lavoura, M. Rebelo, M. Sher, and J. P. Silva, “Theory and phenomenology of two-higgs-doublet models,” *Physics Reports*, vol. 516, pp. 1–102, jul 2012.
- [5] D. Curtin, R. Essig, S. Gori, P. Jaiswal, A. Katz, T. Liu, Z. Liu, D. McKeen, J. Shelton, M. Strassler, Z. Surujon, B. Tweedie, and Y.-M. Zhong, “Exotic decays of the 125 GeV higgs boson,” *Physical Review D*, vol. 90, oct 2014.
- [6] A. M. Sirunyan *et al.*, “Search for an exotic decay of the higgs boson to a pair of light pseudoscalars in the final state of two muons and two  $\tau$  leptons in proton-proton collisions at  $s=13$  tev leptons with the CMS detector,” *Journal of High Energy Physics*, p. 283, 2017.  
$$\sqrt{s} = 13$$
- [7] O. S. Brüning, P. Collier, P. Lebrun, S. Myers, R. Ostojic, J. Poole, and P. Proudlock, *LHC Design Report*. CERN Yellow Reports: Monographs, Geneva: CERN, 2004.
- [8] S. Chatrchyan *et al.*, “The CMS experiment at the CERN LHC,” *JINST*, vol. 03, p. S08004, 2008.

- [9] T. Eichhorn, “Development of Silicon Detectors for the High Luminosity LHC,” 2015. presented 8 Jul 2015.
- [10] S. Chatrchyan, G. Hmayakyan, V. Khachatryan, A. M. Sirunyan, R. Adolphi, G. Anagnostou, S. Brauer, ... Hansel, T. Nobauer, M. Droege, U. Roser, A. Schonning, F. Stockli, and P. Trub, “The CMS experiment at the CERN LHC. The Compact Muon Solenoid experiment,” *JINST*, vol. 3, p. S08004. 361 p, 2008. Also published by CERN Geneva in 2010.
- [11] C. Foudas, “The CMS Level-1 Trigger at LHC and Super-LHC. The CMS Level-1 Trigger at LHC and Super-LHC,” tech. rep., 2008.
- [12] L. Thomas, “CMS High Level Trigger performance at 13 TeV,” *PoS*, vol. ICHEP2018, p. 226. 4 p, 2019.
- [13] CMS Collaboration, “Commissioning of the particle-flow event reconstruction with the first LHC collisions recorded in the CMS detector,” CMS Physics Analysis Summary CMS-PAS-PFT-10-001, CERN, 2010.
- [14] D. Hufnagel, “The architecture and operation of the CMS Tier-0,” tech. rep., CERN, Geneva, Nov 2010.
- [15] J. Knolle, “Precision luminosity measurement with proton-proton collisions at the CMS experiment in Run 2,” tech. rep., CERN, Geneva, Oct 2020.
- [16] CMS Collaboration, “Particle-flow event reconstruction in CMS and performance for jets, taus, and  $E_T^{\text{miss}}$ ,” CMS Physics Analysis Summary CMS-PAS-PFT-09-001, CERN, 2009.
- [17] I. Kratschmer, “Muon reconstruction and identification in CMS Run I and towards Run II,” tech. rep., CERN, Geneva, Oct 2014.
- [18] V. Khachatryan *et al.*, “Performance of electron reconstruction and selection with the CMS detector in proton-proton collisions at  $\sqrt{s} = 8$  TeV,” *JINST*, vol. 10, p. P06005, 2015.
- [19] R. Workman *et al.*, “Review of Particle Physics,” to be published (2022).

- [20] A. Sirunyan, A. Tumasyan, *et al.*, “Performance of reconstruction and identification of  $\tau$  leptons decaying to hadrons and  $\nu_\tau$  in pp collisions at  $\sqrt{s} = 13$  TeV,” *Journal of Instrumentation*, vol. 13, pp. P10005–P10005, oct 2018.
- [21] E. P. O. Group, “Egamma miniaod v2 apply energy scale 13 tev,” August 2022.  
<https://twiki.cern.ch/twiki/bin/view/CMS/EgammaMiniAODV2>.
- [22] T. P. O. Group, “Tauid recommendations 13 tev,” August 2022.  
<https://twiki.cern.ch/twiki/bin/viewauth/CMS/TauIDRecommendation13TeV>.
- [23] CMS, “Search for the standard model higgs boson decaying to a pair of tau leptons in 2016 data,” CMS Note 2016/355, 2016.
- [24] E. P. O. Group, “Electron mva recommendations 13 tev,” August 2022.  
<https://twiki.cern.ch/twiki/bin/view/CMS/MultivariateElectronIdentificationRun2>.
- [25] M. H. Hassanshahi, “Tau identification in CMS during LHC Run 2,” tech. rep., CERN, Geneva, Nov 2021.
- [26] A. Sirunyan, A. Tumasyan, *et al.*, “Particle-flow reconstruction and global event description with the CMS detector,” *Journal of Instrumentation*, vol. 12, pp. P10003–P10003, oct 2017.
- [27] A. M. Sirunyan *et al.*, “Performance of reconstruction and identification of  $\tau$  leptons decaying to hadrons and  $\nu_\tau$  in pp collisions at  $\sqrt{s} = 13$  TeV,” *JINST*, vol. 13, p. P10005, 2018.
- [28] CMS Collaboration, “Identification of hadronic tau lepton decays using a deep neural network,” 2022.
- [29] “Measurement of Higgs boson production in the decay channel with a pair of  $\tau$  leptons,” tech. rep., CERN, Geneva, 2020.
- [30] G. Cowan, K. Cranmer, E. Gross, and O. Vitells, “Asymptotic formulae for likelihood-based tests of new physics,” *The European Physical Journal C*, vol. 71, feb 2011.